

2

DNA-TR-85-352-V

AD-A209 184

**LABORATORY-SCALE AIRBLAST
PRECURSOR EXPERIMENTS**
Volume III—HOB Studies Micro-Mach Experiments

H. Reichenbach
Fraunhofer Institut fur Kurzzeitdynamik
Ernst-Mach-Institut
Eckerstr. 4
D-7800 Freiburg, West Germany

31 March 1989

Technical Report

DTIC
ELECTE
JUN 15 1989
S D D

CONTRACT No. DNA 001-86-C-0075

Approved for public release;
distribution is unlimited.

THIS WORK WAS SPONSORED BY THE DEFENSE NUCLEAR AGENCY
UNDER RDT&E RMC CODE B4693C RA RY 00003 25904D.

Prepared for
Director
Defense Nuclear Agency
Washington, DC 20305-1000

89 6 15 011

Destroy this report when it is no longer needed. Do not return to sender.

PLEASE NOTIFY THE DEFENSE NUCLEAR AGENCY, ATTN: CSTI, WASHINGTON, DC 20305-1000, IF YOUR ADDRESS IS INCORRECT, IF YOU WISH IT DELETED FROM THE DISTRIBUTION LIST, OR IF THE ADDRESSEE IS NO LONGER EMPLOYED BY YOUR ORGANIZATION.



DISTRIBUTION LIST UPDATE

This mailer is provided to enable DNA to maintain current distribution lists for reports. We would appreciate your providing the requested information.

- Add the individual listed to your distribution list.
- Delete the cited organization/individual.
- Change of address.

NAME: _____

ORGANIZATION: _____

OLD ADDRESS

CURRENT ADDRESS

TELEPHONE NUMBER: (____) _____

SUBJECT AREA(S) OF INTEREST:

DNA OR OTHER GOVERNMENT CONTRACT NUMBER: _____

CERTIFICATION OF NEED-TO-KNOW BY GOVERNMENT SPONSOR (if other than DNA):

SPONSORING ORGANIZATION: _____

CONTRACTING OFFICER OR REPRESENTATIVE: _____

SIGNATURE: _____

CUT HERE AND RETURN



Director
Defense Nuclear Agency
ATTN: TITL
Washington, DC 20305-1000

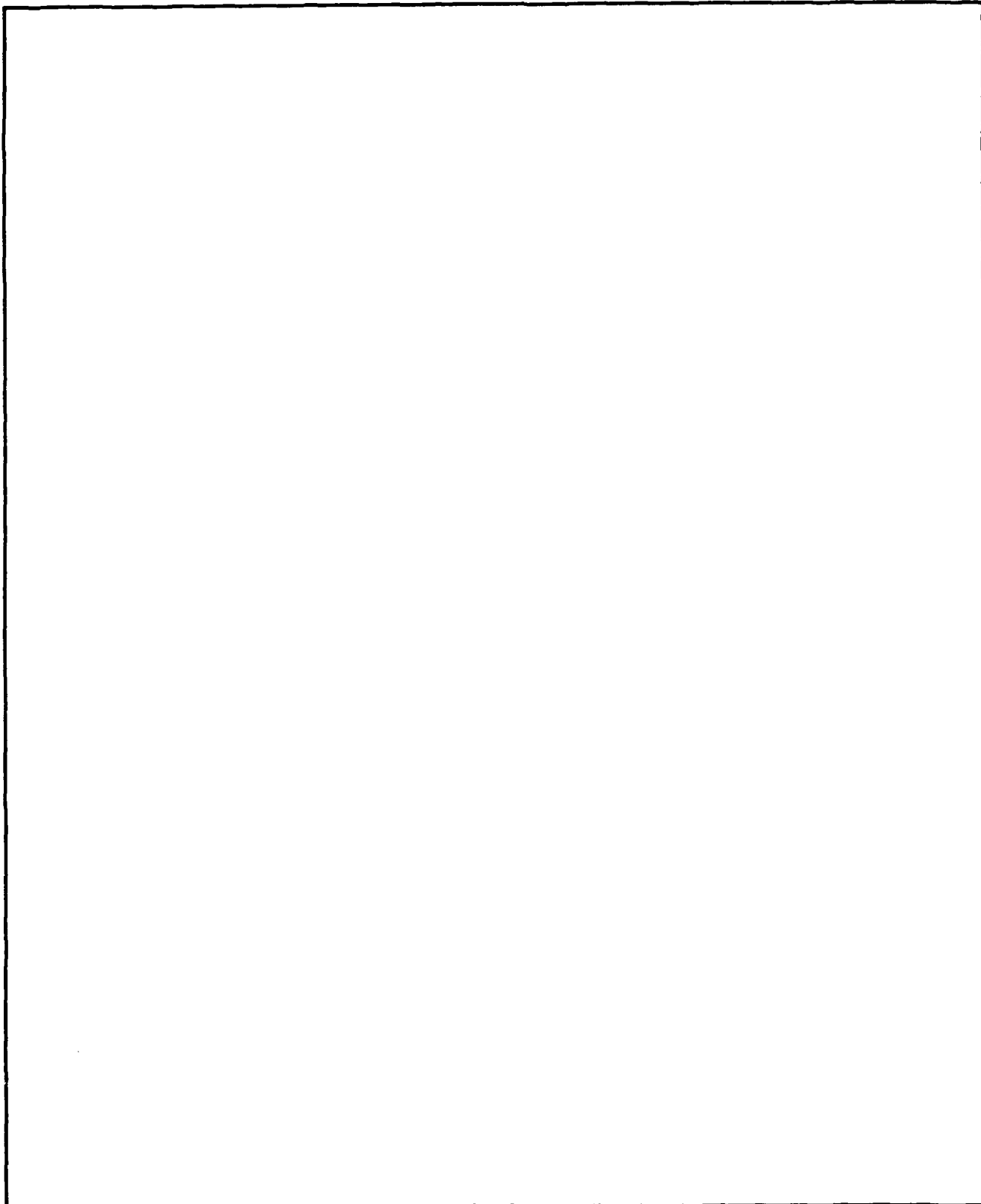
Director
Defense Nuclear Agency
ATTN: TITL
Washington, DC 20305-1000

UNCLASSIFIED

SECURITY CLASSIFICATION OF THIS PAGE

REPORT DOCUMENTATION PAGE				
1a REPORT SECURITY CLASSIFICATION UNCLASSIFIED		1d RESTRICTIVE MARKINGS		
2a SECURITY CLASSIFICATION AUTHORITY N/A since Unclassified		3 DISTRIBUTION AVAILABILITY OF REPORT Approved for public release; distribution is unlimited.		
2b DECLASSIFICATION/DOWNGRADING SCHEDULE N/A since Unclassified		5 MONITORING ORGANIZATION REPORT NUMBER(S) DNA-TR-85-352-V3		
4 PERFORMING ORGANIZATION REPORT NUMBER(S)		7a NAME OF MONITORING ORGANIZATION Director Defense Nuclear Agency		
6a NAME OF PERFORMING ORGANIZATION Fraunhofer Institut fur Kurzzeit- dynamik, Ernst-Mach-Institut		6b OFFICE SYMBOL (if applicable)	7b ADDRESS (City, State, and ZIP Code) Washington, DC 20305-1000	
6c ADDRESS (City, State, and ZIP Code) Eckerstr. 4 D-7800 Freiburg, West Germany		9 PROCUREMENT INSTRUMENT IDENTIFICATION NUMBER DNA 001-86-C-0075		
8a NAME OF FUNDING SPONSORING ORGANIZATION		8b OFFICE SYMBOL SPSP/ Castleberry	10 SOURCE OF FUNDING NUMBERS	
8c ADDRESS (City, State and ZIP Code)		PROGRAM ELEMENT NO 62715H	PROJECT NO RA	TASK NO RY
				WORK UNIT ACCESSION NO DH013330
11 TITLE (Include Security Classification) LABORATORY-SCALE AIRBLAST PRECURSOR EXPERIMENTS Volume III—HOB Studies Micro-Mach Experiments				
12 PERSONAL AUTHOR(S) Reichenbach, H.				
13a TYPE OF REPORT Technical	13b TIME COVERED FROM 880115 TO 881231	14 DATE OF REPORT (Year, Month, Day) 890331	15 PAGE COUNT 82	
16 SUPPLEMENTARY NOTES This work was sponsored by the Defense Nuclear Agency under RDT&E RMC Code B4693C RA RY 00003 25904D.				
17 COSAS CODES		18 SUBJECT TERMS (Continue on reverse if necessary and identify by block number)		
FIELD	GROUP	SUB-GROUP		
19	09		Precursor	
14	02		Air Blast	
		Height of Burst; Shock Tube Experiments. West Germany		
19 ABSTRACT (Continue on reverse if necessary and identify by block number) This work was undertaken to increase the understanding of the fluid dynamics of airblast precursors. A series of shock tube experiments were conducted using a helium layer from a porous plate and a heated plate to create a surficial high-sound-speed layer. A series of small charge tests were conducted in an enclosed environment using a helium-induced high sound speed layer introduced from a circularly symmetrical ceramic porous plate.				
20 DISTRIBUTION AVAILABILITY OF ABSTRACT <input type="checkbox"/> UNCLASSIFIED UNLIMITED <input checked="" type="checkbox"/> SAME AS RPT <input type="checkbox"/> DTIC USERS		21 ABSTRACT SECURITY CLASSIFICATION UNCLASSIFIED		
22a NAME OF RESPONSIBLE INDIVIDUAL Bennie F. Maddox		22b TELEPHONE (Include Area Code) (202) 325-7042	22c OFFICE SYMBOL DNA/CSTI	

UNCLASSIFIED
SECURITY CLASSIFICATION OF THIS PAGE



PREFACE

We would like to thank Dr. George Ullrich, from the Shock Physics Directorate of Defense Nuclear Agency (DNA) for his encouragement and support in the execution of this task. Dr. Allen Kuhl, R & D Associates, is thanked for all his advice, his encouraging discussions, his help with the interpretation of the results, and his continual interest during his visits to EMI.

Without the careful conducting of the experiments by Dipl.-Ing. (FH) W. Schätzle and Mr. W. Gehri, the results could not have been achieved. For help with data handling and drawing diagrams, we have to thank Dr. Scheklinski-Glück, Mr. E. Bühler and Mrs. E. Götzmann. The cooperation of the EMI mechanical workshop, under the direction of Mr. M. Scharbach, and of the photographic laboratory, under the direction of Mr. B. Grünewald, and the preparation of the report by Mrs. S. Deschoux are gratefully acknowledged.

The financial support received from the U.S. Defense Nuclear Agency under contract no. DNA 001-86-C-0075 is greatly appreciated.



Accession For	
NTIS CRA&I	<input checked="" type="checkbox"/>
DTIC TAB	<input type="checkbox"/>
Unannounced	<input type="checkbox"/>
Justification	
By	
Distribution /	
Availability Codes	
Dist	Avail and/or Special
A1	

TABLE OF CONTENTS

Section	Page
PREFACE	iii
LIST OF ILLUSTRATIONS	v
1 INTRODUCTION	1
2 EXPERIMENTAL APPARATUS	3
2.1 TEST CHAMBER	3
2.2 OPTICAL EQUIPMENT	4
2.3 ELECTRONIC EQUIPMENT	5
2.3.1 Electronic Control System	5
2.3.2 Pressure Recording System and Display	6
2.4 HE-FILLING SYSTEM	6
2.5 HE-CONCENTRATION MEASUREMENTS	8
2.5.1 Measurement Principle and Probe Construction	8
2.5.2 Calibration of the Probes	9
3 HIGH EXPLOSIVE CHARGE	10
3.1 MANUFACTURING OF THE CHARGE	10
3.2 DETERMINATION OF THE CHARGE EQUIVALENT	11
3.2.1 Charge Equivalent Related to the Peak Overpressure	11
3.2.2 Charge Equivalent Related to the Overpressure Impulse	12
4 RESULTS	13
4.1 HOB EXPERIMENTS WITHOUT HE LAYER	13
4.1.1 Smooth Surface	13
4.1.1.1 Optical Measurements	13
4.1.1.2 Pressure Measurements	14
4.1.2 Rough Surface	14
4.1.2.1 Optical Measurements	15
4.1.2.2 Pressure Measurements	15
4.1.3 Comparison between Smooth and Rough Surface Data	15
4.1.4 Determination of the Charge Scale Factor	15
4.1.4.1 Comparison with TNT Free Field Data	15
4.1.4.2 Comparison with RDX-HOB Curves	17
4.2 HOB EXPERIMENTS WITH HELIUM LAYER	17
4.2.1 Helium Concentration Distribution in the Layer	17
4.2.2 HOB Experiments	18
4.2.2.1 Optical Measurements	18
4.2.2.2 Pressure Measurements	19
5 SUMMARY AND CONCLUSIONS	21
5.1 SMALL-CHARGE DEVELOPMENT	21
5.2 BLAST WAVE DRIVEN BY NP CHARGE	21
5.3 BLAST WAVE SCALE	21
5.4 INSTRUMENTATION FOR THE HEIGHT OF BURST TESTS	22
5.5 IDEAL HEIGHT OF BURST RESULTS	23
5.6 HEIGHT OF BURST TESTS OVER ROUGH SURFACES	23
5.7 HELIUM LAYER PRECURSOR TESTS	24
6 RECOMMENDATIONS	26

LIST OF ILLUSTRATIONS

Figure	Page
1 Test chamber for Micro-Mach experiments.	27
2 Overview picture of the test chamber.	28
3 New design of the roof plate.	28
4 Optical setup for high speed camera pictures.	29
5 Optical setup for single frame pictures.	30
6 Cordin camera with rotator and control unit.	31
7 Light source with light output between 40 μ s and 700 μ s in the form of a square wave pulse. Energy source, pulse former, trigger, and delay circuits are installed in their own cabinet.	31
8 EMI single spark point light source. Power supply and trigger are integrated in a single box. Exposure time: 0.3 μ s.	32
9 7-channel timing unit.	32
10 Charge ignition unit with trigger and delay device.	33
11 Circuit diagram of the electronic equipment.	34
12 Timing diagram for single spark photography. The given helium pressures are measured in the helium lines (Fig. 23). The diagram portrays test M 0228.	35
13 Timing diagram for Cordin camera records. The given helium pressures are measured in the helium lines (Fig. 23). The diagram portrays tests M 0246 - M 0249 (overlapping records).	36
14 Pressure recording system. On the left: 12-channel Le Croy transient recorder with calibration device and computer. On the right: printer and plotter. The recording system is installed in a Faraday cage.	37
15 Example of a pressure record. Charge ignition signal and light source trigger signal are visible. The second curve gives the overpressure impulse, $I = \int \Delta p dt$. The data for peak overpressure, maximum impulse, time of arrival, and positive duration are printed automatically in the diagram.	38
16 Example of a data summary sheet. After each test the sheet is printed with the calibration data of the 12 measuring channels.	39
17 Transducer mounting for vibration damping.	40
18 Location of the transducers. Top view of the test chamber G ₁ . . . G ₁₂ = gauge location. Distance between two gauges 5.7 cm (11.4 cm between G ₁₁ and G ₁₂). See also Figure 20.	40

LIST OF ILLUSTRATIONS (Continued)

Figure	Page	
19	The lid of the test chamber (upside down). The different grooves are visible, as are the bolts which serve to fix the Filtrokelit plate.	41
20	Tubing of the helium filling system. Some tubes are removed for a better overview. The position of the pressure transducers can be seen along a diagonal.	41
21	Side and top view of the bore holes in the lid of the test chamber.	42
22	Pumping system (see also Fig. 11, Fig. 12 Fig. 13, Fig. 21).	43
23	Helium rinsing and filling system (see also Fig. 11, Fig. 12 Fig. 13, Fig. 21).	44
24	Construction of the helium probe.	45
25	Circuit diagram of the electronic bridge of the helium probe.	46
26	8-channel helium-concentration measuring arrangement.	47
27	Calibration curve for helium-concentration measurements.	48
28	Intermediate stages of the manufacturing process of the HE charge.	49
29	Some frames of a Cordin-camera film. Test No. M 027; HOB = 12.5 cm, smooth surface (aluminum). Charge weight = 0.6 g. Exposure time of a frame 3 μ s.	50
30	Single frame photographs. Tests No. M 44, M 46, M 42, M 43. HOB = 12.5 cm; smooth surface (aluminum). Charge weight = 0.6 g. Exposure time = 0.3 μ s. First frame shows charge before detonation.	51
31	Explanation of the wave system in the case of non-precursed blast propagation.	52
32	Single frame photographs. Tests No. M 51; M 50; M 49; M 48; HOB = 12.5 cm; rough surface; charge weight = 0.6 g; exposure time = 0.3 μ s. First frame shows charge before detonation.	53
33	Peak overpressure P_{50} at smooth and rough surfaces. HOB = 6.7 cm, charge weight = 0.6 g. The error bars are marked left and right of the data points for a clearer representation.	54
34	Overpressure impulse I_+ at smooth and rough surfaces. HOB = 6.7 cm, charge weight = 0.6 g. The error bars are marked left and right of the data points for a clearer representation.	55

LIST OF ILLUSTRATIONS (Continued)

Figure	Page	
35	Comparison between measured radius-time values of the shock front from Cordin camera pictures with time-of-arrival TNT free field data. Upper diagram is before matching, lower diagram is after matching. TNT equivalent factor: $f_0 = 1.4$.	56
36	Comparison between evaluated peak overpressure-distance value from Cordin camera pictures with peak overpressure free field data for TNT. TNT equivalent factor $f_0 = 1.4$.	57
37	Comparison with RDX-HOB curves. In this case, the best fit is achieved with an RDX equivalent factor of $f_0 = 0.7$.	58
38	Measured helium concentration as function of radius and height. High helium concentrations of more than 90% were achieved.	59
39	Two frames of a Cordin cinematographic picture series. Test No. M 228. Frame 59 and 84. HOB = 6.7 cm.	60
40	Precursed and ideal HOB-shock structure. HOB = 6.7 cm. a) 180 μ s after charge ignition (tests M 263 and M 198) b) 220 μ s after charge ignition (tests M 264 and M 190) c) 250 μ s after charge ignition (tests M 260 and M 183) d) 350 μ s after charge ignition (tests M 262 and M 201)	61 62
41	Deformation of the edges of a cube by light deflection in an inhomogenous density field (Tests M 240, M 236, M 237).	63
42	Pressure records at different ground range positions for nonprecursed (black) and precursed (grey) blast (for positions see Fig. 18; tests M 245 and M 248, resp.).	64
43	Impulse curves at different ground range positions for nonprecursed (black) and precursed (grey) blast (tests M 245 and M 248, resp.).	68
44	Peak overpressure versus ground range for nonprecursed blast at smooth and rough surfaces, respectively, and for precursed blast. HOB = 12.5 cm ($375 \text{ ft/kt}^{1/3}$).	70

SECTION 1 INTRODUCTION

If a blast wave propagates in a medium where a thin layer of high-temperature gas is located near the ground, a precursor develops. In an earlier report sponsored by the Defense Nuclear Agency (Contract No. DNA-001-84-C-0342), the fundamental features of the interaction processes were described and illustrated.* Different techniques were successfully developed to

- create and control high-sound-speed layers in the laboratory.
- demonstrate which physical questions may be asked.
- determine which questions can be answered by such tests.

Two experimental methods proved to be especially successful in reproducibly simulating relatively thin high-sound-speed layers in a small shock tube:

- 1) Hot air layers formed by electrically heated metallic strips
- 2) Free helium layers on the surface of porous ceramic plates (Filtrokelt plates)

To increase the understanding of the fluid dynamics of airblast precursors, DNA awarded another contract (DNA-001-86-C-0075) to EMI to undertake the following tasks:

Task 1: Conduct a series of shock tube experiments using a helium layer from a porous plate and a heated plate to create a surficial high-sound-speed layer.

Task 2: Conduct a series of small charge tests in an enclosed environment using a helium-induced high sound speed layer introduced from a circularly symmetrical ceramic porous plate.

* H. Reichenbach, Laboratory-Scale Airblast Precursor Experiments, Vol. 1: Exploratory Shock Tube Tests; DNA-TR-85-352, Defense Nuclear Agency, Washington, D.C. 1985.

The results of Task 1 have been reported earlier.* The shock tube tests were able to answer such questions as:

- Why does the precursor wall jet become turbulent?
- What is the effect of the thermal layer vertical gradient on:
shock structure? (negligible)
wall jet shape? (important)
wall jet turbulence? (important)
- Why does the wall jet show fine-scale turbulence?
- What is the influence of the wall boundary layer and wall roughness?

The present report describes small (laboratory) scale height-of-burst experiments. Because such small charges were used (0.6 g spheres of hexogen), we called the tests of Task 2 "Micro-Mach Experiments."

The objectives of the tests were as follows:

- (1) To utilize the EMI optical capabilities to give a high-fidelity flow visualization of the evolution of an HOB airblast precursor without the influence of a membrane (i.e., similar to physical problems).
- (2) To measure pressure histories on the surface without influence of terrain and weather effects.
- (3) To compare ideal and non-ideal blast wave environments under well-controlled conditions.

* H. Reichenbach, Laboratory-Scale Airblast Precursor Experiments. Vol.2: Parametric Studies, EMI Rep. E 6/87.

SECTION 2 EXPERIMENTAL APPARATUS

2.1 TEST CHAMBER.

The Micro-Mach experiments were conducted in a cubical test chamber (120 cm by 120 cm by 60 cm) shown in Figure 1. This approach gave well-controlled ambient conditions, and protected personnel and sensitive laboratory equipment from the effects of the explosion. The chamber was shock-isolated from the floor to minimize any blast-induced vibrations of the sensitive optical equipment. The chamber was equipped with optical quality windows (69 cm by 20 cm by 2 cm) for high-speed photography (see Fig. 2).

The aluminum walls of the chamber were bolted together and easily replaceable. A removable circular roof plate provided easy access to the chamber for charge emplacement and instrumentation adjustments. A small crane facilitated the handling of this heavy plate. This roof plate formed the reflecting surface for the height-of-burst tests. For ideal-surface experiments, a polished aluminum surface was used. For the precursor test, a helium distribution system was incorporated into the plate. In the original design, this consisted of a 66 cm-diameter by 2-cm thick porous ceramic plate (Filtrokelit) mounted flush with the roof of the test chamber. The high sound speed layer was created by forcing helium through the porous plate by means of a pressurized chamber mounted behind the plate. In the final design, the porous plate area was increased, as shown in Figure 3. We have now a good tool at our disposal for future experiments.

In previous shock tube tests it was found advantageous to have the He layer at the roof and not at the bottom to control for the buoyancy of helium. Therefore for the Micro-Mach experiments the He layer was produced at the ceiling. However, when describing the tests, we speak as if the helium layer were on the bottom or ground. So we speak of ground zero and height of burst.

2.2 OPTICAL EQUIPMENT.

A Cordin high-speed camera (type 330) or a single frame system were used to photograph the explosion. The optical setup differs slightly, as shown in Figures 4 and 5. Two spherical mirrors with a diameter of 640 mm each and a focal length of about 4 m are arranged so as to produce parallel light at the location of the test chamber. If a knife blade is installed at the second focus of the light path, schlieren photographs can be taken. This method was also used to visualize the helium layer.

The continuous writing Cordin camera (Fig. 6) needs a light source with an adjustable light output in the form of a square wave pulse. If the light duration is too long, the first frames will be double-exposed. We therefore developed our own special light source for the Cordin camera with an output diameter of 1 mm. The light source is shown in Figure 7 together with the energy source, the pulse former, the trigger, and the delay circuits respectively. The light output can be adjusted between 40 μs and 700 μs depending on the framing frequency of the camera.

The exposure time of a frame in a rotating prism camera depends on the frame period. In the version we used, the exposure time equals about half of the frame period.

A photo of the EMI single-spark point light source for shadow and schlieren pictures is shown in Fig. 8. Power supply and trigger circuit are combined with the point source. Due to the coaxial construction, an exposure time of 300 ns (= 0.3 μs) is achieved. The pinhole in the electrode corresponding to the light output area has a diameter of 0.5 mm.

The alignment of the optical light path was facilitated by using a He-Ne-laser system. Due to the long light paths, the optical system is very sensitive to vibrations and small twisting of the components. Therefore great care must be taken to get reproducible picture quality.

2.3 ELECTRONIC EQUIPMENT.

2.3.1 Electronic Control System.

In addition to high speed photography of the explosion, pressure measurements were made. Thus the ignition of the charge, the triggering of the light source, and the initiation of the 12-channel transient recorder (Le Croy type TR 8837) had to be synchronized. As will be described later, accurate timing of the He filling process was also needed to obtain reasonably reproducible helium layers. Therefore, we had to develop a new timing control system to meet the numerous filling and triggering requirements. Some new devices were produced, as shown in Figures 9 and 10. The principle of our electronic arrangement is sketched in Figure 11.

For tests without a helium layer the pulse generator (HP 8010 A) is started manually. The sharp rising pulse triggers three delay generators. The first delayed pulse starts the 12-channel computer-operated Le Croy transient recorder to store the pressure-time signals of the pressure transducers (Kistler type 603 B). The sampling rate of the 8-bit recorder is 32 MHz. The time window can be chosen between 32 μ s and 16 ms. The second delayed pulse starts the ignition circuit of the charge. A capacity of 2 μ F loaded to 5 - 12 kV is discharged into a thin wire. This wire explodes and ignites the charge. A third delayed pulse starts the light source, either the single spark (Fig. 8) or the special light source of the Cordin camera (Fig. 7).

For tests with a helium layer, a timing unit with seven independent channels steers the pump and valves of the gas filling system (see Section 2.4). One of the channels triggers the pulse generator. When the timing unit is started manually, all the other functions needed for a test are triggered automatically. Only the Cordin camera is operated by hand controls because pretriggering by the camera pulse is not possible. The gas filling system requires 20 seconds for purging and creation of the helium layer before ignition of the charge.

Figures 12 and 13 depict examples of two timing diagrams for single spark photography and cinematography with the Cordin camera, respectively. Note that the time scale for the gas filling procedure is given in seconds whereas the scale for triggering the ignition and the measuring system is given in microseconds.

2.3.2 Pressure Recording and Display.

Experiments with such small HE charges require a pressure recording system with a high time resolution and also a large gain range. It must be able to record peak pressures between 0.1 bar and 300 bar with a high signal-to-noise ratio. We therefore installed a computer-operated transient recorder system with 12 channels (Le Croy type T.R. 8837 F). Kistler gages (type 603 R) with charge amplifiers (type 5001) served as pressure transducers. The signals of the 12 channels are stored in digital form and can be plotted one after the other on a plotter (Epson type 800). Our own computer program was developed to calibrate each individual channel with respect to the expected signal level. The plot program allows a choice of formats. Not only the pressure time curves are plotted but also the overpressure impulse, the positive duration, and the time of arrival. All the data needed for test evaluation are printed as a data summary sheet. The recording system is shown in Figure 14. Figures 15 and 16 are examples of the quality of the plotted curves and the data summary sheet, respectively.

Great care was needed to install the pressure gages. At first, the blast-induced vibrations of the walls greatly influenced the transducer signals. We tried different shock-absorbing mountings. Good results were achieved with the system sketched in Figure 17.

The locations of the transducers are specified in Figure 18. Gage 1 is placed at ground zero. The others are arranged along a diagonal at a distance of 57 mm in each case, except gage 12 with an interval of 11.4 mm to gage 11 (see also Fig. 20).

2.4 HE FILLING SYSTEM.

In previous shock tube tests, it was relatively easy to produce a thin, uniform helium layer by diffusion through a porous ceramic plate. We therefore expected little difficulty in applying this technique to the height-of-burst tests. We found, however, that it was very difficult to create a stable, laminar, uniform helium layer in this circular layer geometry. After much experimentation, we arrived at the following design.

The plenum chamber contained several broad circular grooves to circulate the helium. Along one radius, the grooves are interrupted by a barrier. The helium flow was introduced on one side of the barrier and forced to propagate along the channel to reach the outlet on the other side of the barrier where the gas is pumped out. A nearly uniform helium distribution is achieved behind the Filtrokelit plate because the flow velocity in the grooves is much higher than the diffusion rate through the 2-cm-thick ceramic plate. In Figure 19, the lid with the different grooves can be seen (upside down) before the Filtrokelit plate was inserted and tightly bolted. In the middle and in an outer ring, porous bronze pieces are inserted to allow blowing or suction of helium or air. This permits some variations in the filling process to influence the helium layer above the ceramic plate.

Figure 20 shows the plastic filling tubes and the small inlet and outlet pipes. To have a better overview, some of the filling tubes are removed. The positions of the pressure transducers are clearly visible along a diagonal.

The bore hole locations in the lid are sketched in Figure 21. The holes $P_1 - P_9$ are connected with the vacuum pump, see Figure 22. The inlet holes for helium are marked $H_1 - H_{13}$. The function is explained in Figure 23.

As mentioned earlier, some difficulties were encountered in producing a relatively thin uniform helium layer with a concentration high enough for precursor investigations. It was impossible to obtain reproducible layers by hand-operating the filling system. As we learned in the course of numerous experiments, the operating time of the different valves (see Figs. 22 and 23) must be controlled with an accuracy better than a tenth of a second. Therefore a special timing device was developed (see Section 2.3.1 and Fig. 9).

The filling procedure starts with rinsing the vessel. Valve 1 is in the open position. Air is sucked through the vessel where, near the bottom, a valve-controlled opening exists which remains open during the whole test. Thus the helium-air mixture of a previous test may be removed. When the timing device is triggered, valve 2 opens and the gas in the grooves behind the Filtrokelit plate is sucked out (see Fig. 22). One second after triggering, valve 1 is closed and the rinsing process of the vessel is finished. Five seconds later, valve 3 is opened (see Fig. 23) and the rinsing process of the helium tubing starts. This procedure lasts about 20 seconds and is sufficient to fill the pipes and the pores of the ceramic plate with nearly pure helium. About 2 seconds earlier, valve 2 is closed and pumping is stopped. Valves 4

and 5 are operated for about 1 and 1.5 seconds, respectively. They close simultaneously with valve 3. Because the pressure in the helium lines 1 and 2 is higher than in the rinsing line, helium is pressed through the Filtrokelit plate just before the charge is fired. The ignition is triggered about 0.5 seconds (typically) before the closure time of valves 3, 4, and 5.

The timing of the different valves is specified in Figures 12 and 13, which indicate also the typical pressures in the different lines.

2.5 HE-CONCENTRATION MEASUREMENTS.

As discussed, the procedure to create a helium layer must be controlled very carefully. Shadow and schlieren pictures alone cannot give enough information. First, we used 3 helium concentration probes (provided by Dynamics Technology, Inc.)* to measure the helium concentration in the layer versus time. With the help of the probes, it was possible to check the concentration inside the helium layer and also to control the efficiency of the helium filling system. But more than 3 probes were needed to measure the spatial distribution of helium concentration. We therefore developed our own automated system that provides measurements at 8 different positions simultaneously.

2.5.1 Measurement Principle and Probe Construction.

The probe acts as a hot-wire anemometer. A constant gas flow through the probe was created by a sonically choked nozzle. This flow cools the hot wire by convective heat transfer, and this changes the electrical resistance of the wire. If the parameters are kept constant, the cooling effect depends on the helium concentration in the gas flow. (Helium is more efficient than air.)

The hot wire forms one arm of an electronic bridge. A compensating circuit balances the bridge so that the wire resistance (or in other words, the temperature) remains constant. The compensating current is then a measure of the concentration.

* We are very grateful to Dr. Allen Kuhl, RDA, for the idea and for his assistance in arranging the loan of the measuring device and its transfer from the USA to EMI.

The probe construction is shown in Figure 24. By means of a vacuum pump, gas is sucked through a nozzle of a diameter of 0.08 mm. The nozzle used is commercially available. The ratio of the pressures on both sides of the nozzle is high enough to guarantee a supersonic flow behind the nozzle. In this case, the mass flow through the nozzle is constant and independent of the pressure ratio. The wire is located between the gas inlet tube and the supersonic nozzle.

The circuit diagram of the electronic bridge is given in Figure 25. The output signal is registered on an 8-channel plotter. An overview is presented in Figure 26.

2.5.2 Calibration of the Probes.

A priori, there is no reason to expect a linear relationship between the helium concentration and the output signal of the electronic bridge. Hence, we calibrated the gages in the following manner. The signal resulting from pure air at ambient pressure being sucked through the probe was defined as zero level signal. The signal resulting from pure helium was defined as the 100 % level signal. Precise helium/air mixtures needed for values in between are relatively difficult to produce. Therefore, we used commercially available mixtures with guaranteed mixture ratios from the German company Messer-Griesheim. Pressure ratios of 80 % He and 60 % He were used.

From a total of about 20 probes, we selected 8 with nearly the same calibration curve and sensitivity to simplify the evaluation of the measured data. A typical calibration curve is shown in Figure 27.

SECTION 3 HIGH EXPLOSIVES CHARGE

3.1 MANUFACTURING OF THE CHARGE.

The most critical part for Micro-Mach experiments is, of course, the high explosives charge. To simulate a 1 kt detonation in the laboratory, a linear scale reduction of about 1 : 1000 must be realized. Crazz-Hopkinson scaling requires then a charge weight of 1 : 1000³. This rough estimate indicates that the model charge should have a weight of about 1 g. A more careful calculation, taking due consideration that the model charge must be a more sensitive explosive than TNT, indicates a charge mass of about 0.6 g. This very small charge should be safe enough to be handled in the laboratory without any severe restrictions but, on the other hand, should be sensitive enough to detonate completely if electrically ignited. Primary explosives such as lead acid or silver acid were eliminated for safety reasons. Commercially available HE was not sensitive enough to detonate completely in such small quantities. We therefore developed our own explosive. It consists of extremely fine powdered nitropenta dissolved in a mixture of gun-cotton and acetone. This paste dries relatively quickly, so it can easily be formed into a droplet. To get an ideal spherical shape with an ignitor in the center, we developed the following method (see Fig. 28).

Two electrodes are fixed in a centered holder so that a very fine wire can be wrapped around them (Fig. 28a). The holder is dipped several times into the explosive mixture until a nearly spherical shape is achieved (Fig. 28b - e). Following a drying process, an ideal sphere is turned on a lathe before the holder is removed (Fig. 28f). By this method, the ignitor can be placed with high accuracy in the center of the HE sphere. Because the density of the HE mixture is sufficiently constant, the mass of the charge is given by the diameter of the sphere. This measure can be controlled and kept fixed very easily.

As the results discussed in Section 4 confirm, the reproducibility of tests with this model charge is excellent.

3.2 DETERMINATION OF THE CHARGE EQUIVALENT.

To be able to compare the results with data from tests with other explosives, an equivalency factor is required. But it is well known that this factor is not the same if peak pressure or overpressure impulse data, respectively, of different explosives are compared. Also, the equivalency factor varies with the pressure and impulse level where the comparison is made. So it is important to define in which way the charge equivalent is determined.

3.2.1 Charge Equivalent Related to the Peak Overpressure.

To determine the charge equivalent, the peak overpressure must be known as a function of the scaled distance $R/W^{1/3}$ (R = distance, W = charge weight) of the explosives to be compared. By definition, the same peak overpressure P_{so} must exist at the same distance R for both explosives. Then both charges are equivalent.

If Z is the scaled distance for the peak overpressure P_{so} , then

$$Z_1 (P_{so}) = \frac{R_1}{W_1^{1/3}} \quad \text{for explosive 1, and} \quad (3.1)$$
$$Z_2 (P_{so}) = \frac{R_2}{W_2^{1/3}} \quad \text{for explosive 2}$$

Both charges are equivalent if $R_1 = R_2 = R$

$$Z_1 \cdot W_1^{1/3} = Z_2 \cdot W_2^{1/3} \quad \text{or}$$

$$W_1 = \left(\frac{Z_2}{Z_1} \right)^3 \cdot W_2$$

The term $(Z_2/Z_1)^3 = f_o$ is the charge-equivalent factor related to the given peak overpressure.

3.2.2 Charge Equivalent Related to the Overpressure Impulse.

By definition, the same specific overpressure impulse I_s must exist at the same distance R for both explosives. In this case, the charges are equivalent. In contrast to the overpressure $p(t)$, the impulse

$$I_s = \int_0^{t_+} \Delta p(t) dt \quad (3.2)$$

is a scaling-dependent variable. We therefore plot I_s/R as a function of $R/Q^{1/3}$. For a desired overpressure impulse I_{s0} , we get as scaled distance

$$Z_{i1} (I_{s0}/R_1) = R_1/W_1^{1/3} \quad (3.3)$$

$$Z_{i2} (I_{s0}/R_2) = R_2/W_2^{1/3}$$

Because R_1 and R_2 in both cases should be the same, we receive

$$Z_{i1} W_1^{1/3} = Z_{i2} W_2^{1/3} \quad \text{or}$$

$$W_1 = \left(\frac{Z_{i2}}{Z_{i1}} \right)^3 \cdot W_2$$

The term $(Z_{i2}/Z_{i1})^3 = f_i$ is the charge-equivalent factor related to the given overpressure impulse I_{s0} .

As a rule, the factors f_0 and f_i are not identical and, in addition, depend on the chosen peak overpressure and overpressure impulse, respectively, where the comparison is made.

SECTION 4 RESULTS

4.1 HOB EXPERIMENTS WITHOUT HE LAYER.

Numerous experiments were carried out to determine the influence of the rough Filtrokelit surface on the wave propagation, the time of arrival, the peak overpressure, and the overpressure impulse, respectively. The purposes of the tests were to investigate the reproducibility and accuracy of the results and to evaluate the airblast scale factors for this charge.

The following heights of burst were chosen: $H = 3.3$ cm; 6.7 cm; 7.7 cm; 8.5 cm; 12.5 cm; 20.2 cm; 26.9 cm; 33.7 cm; and 40.4 cm, respectively. The most preferred heights were $H = 6.7$ cm and $H = 12.5$ cm.

4.1.1 Smooth Surface

To simulate ideal free field values, a polished aluminum plate was used instead of the porous ceramic plate.

4.1.1.1 Optical Measurements. Cinematographic picture series were taken with a Cordin continuous writing and framing camera (type 330). Some frames of a picture series are shown in Figure 29.

The shock fronts are not as sharp as we are accustomed to from shock tube tests. But one must take account of the fact that in these experiments the blast wave expands spherically. The wave fronts are curved and the light path is deflected through inhomogeneous regions. By diffraction effects, the shock fronts seem to broaden and many details in the flow field are lost. In addition, the pictures are slightly blurred because the exposure time of each individual frame is too long (~ 3 μ s). The exposure time in a high speed camera with rotating prism depends on the frame period. In our camera, the ratio of exposure time to frames period is about 0.5.

Figure 30 depicts some single pictures of different tests under the same conditions but with variation of the delay time between charge ignition and triggering the light source. In this case, the exposure time is 0.3 μ s. The snapshot time of the photographs in Figures 29 and 30 is nearly the same.

It is evident that the shock fronts and the wave interactions in single picture technique are much clearer, but many more tests are required to produce a sequence of photos with this technique.

It can be seen that the wave fronts from different tests are reproducible. The flow field behind the shock fronts changes a little bit by random effects. Jets from instabilities on the charge surface are present, and it was not possible to avoid them completely. During the fabrication of the small charges we made several attempts to get the most homogeneous detonation pattern, but we were only partially successful. However, it is well known that jets are also present in large HE field tests (e.g., DNA's 500-ton experiments). In this respect, the Micro-Mach tests seem to be realistic experiments. The wave system is explained in Figure 31.

4.1.1.2 Pressure Measurements. For each test, the pressure-time history was measured at 12 different locations, as described in Section 2.3.2 (see Fig. 18). When the Le Croy 12-channel transient recorder was not available (until test No. M 191), measurements were only possible at 8 stations. The pressure records do permit us to evaluate the time of arrival (TOA), the overpressure impulse (I+), and the positive phase (t+), respectively (see Fig. 15). The results for different heights of burst (HOB) are presented in Table 1, which also shows the mean values and the standard deviation values. The data demonstrate the excellent reproducibility of the tests. Records are shown in Figure 42.

4.1.2 Rough Surface.

As shown in a previous report, the roughness centers on the surface of a slightly polished Filtrokelt plate have a height of about 30 μ m.* In addition to the roughness effect on the parameters of the blast wave, we also have to consider that a small inflow exists in the pores of the ceramic plate. So we have to expect that the time of arrival, the overpressure, and the impulse are a little bit smaller compared to the smooth surface data.

* See Figure 11 of volume 2: Parametric Studies, EMI Rep. E 6/87

4.1.2.1 Optical Measurements. As in the case of the smooth surface, cinematographic pictures with the Cordin camera and pictures in single frame technique were taken. Significant differences between the smooth and rough surfaces cannot be detected. In Figure 32, two single frame pictures at different times are shown as examples.

4.1.2.2 Pressure Measurements. The pressure records of the rough surface experiments look like those obtained in smooth surface tests. The data are specified in Table 2 in the same format as Table 1, so an easy comparison is possible. The data are self-consistent and confirm the good reproducibility of the tests.

4.1.3 Comparison between Smooth and Rough Surface Data.

The diagrams of the peak overpressure and impulse (versus distance from ground zero) (Figs. 33 and 34) show that there is, as expected, a tendency for smaller values in the case of rough surface data. But the error bands ($\pm \sigma$ of single values) overlap each other. From a statistical standpoint, a significant difference cannot be stated. If more tests can be carried out with a more extended rough surface (as possible with the new design shown in Fig. 3), more precise results are to be expected. The same happens if the roughness of the surface is enlarged.

4.1.4 Determination of the Charge Scale Factor.

4.1.4.1 Comparison with TNT Free Field Data. Two methods were applied to compare Cordin camera data with TNT free field values.

At first, from the Cordin camera pictures, the time-distance values of the shock front were measured along a line parallel to the surface at the distance of the height of burst. These values should correspond with the free field values as long as the Mach stem does not reach the measuring line.

Using the first method, the data were then compared with the time of arrival values of TNT free field results. The upper diagram in Figure 35 shows the comparison of the measured values with the TNT standard curve before matching. In the lower diagram a TNT equivalent factor (see Section 3.2.1) of

$$f_0 = 1.4$$

was applied. Now the data match very well in the range between $0.5 < R/W^{1/3} < 2$. This means that in the given range 1 g of our charge corresponds to 1.4 g of TNT. According to the second method, the measured time-distance values of the shock front were fitted by a polynom of 6th order.

$$x = \sum_{n=0}^6 b_n t^n \quad (4.1)$$

This function was differentiated in respect to t and derived from the sound speed of air, a_0 . The result is an analytical expression of the Mach number of the shock front.

$$M_s = \frac{1}{a_0} \sum_{n=0}^6 n b_n t^{n-1} \quad (4.2)$$

If one assumes ideal gas behavior the peak overpressure as function of the shock Mach number is given by

$$p = P_{21} - 1 = \frac{7}{6} (M_s^2 - 1) \quad (4.3)$$

Converting Eq. 1 the peak overpressure can be determined as function of distance. With the same TNT equivalent factor of

$$f_0 = 1.4$$

the data match very well with overpressure-distance curves for TNT* in the range $0.7 \text{ bar} < \Delta P_s < 3 \text{ bar}$, as shown in Figure 36.

* Charles N. Kingery and Gerald Bulmash, Airblast Parameters from TNT Spherical Air Burst and Hemispherical Surface Burst, ARBRL-TR-02555, April 1984.

4.1.4.2 Comparison with RDX-HOB Curves. Numerous HOB data are available from earlier tests with spherical RDX charges. Results are given in EMI Report E 26/85.* The Nitropenta small charge overpressure measurements were compared with the RDX-HOB curves. As shown in Figure 37, the data are in excellent agreement with these curves if

$$f_0 = 0.7 \text{ (RDX)}$$

is applied as RDX equivalent factor. Because RDX is a high explosive with a higher energy content than TNT it is evident that the RDX equivalent factor of the Nitropenta charge is smaller than for TNT. Thus 1 g of our charge corresponds to 0.7 g of RDX.

The solid lines in Figure 37 are RDX-HOB curves. The data points represent the measured values after correction with $f_0 = 0.7$.

4.2 EXPERIMENTS WITH HELIUM LAYER.

4.2.1 Helium Concentration Distribution in the Layer.

The vertical and horizontal concentration distribution was determined with 8 helium concentration measuring probes (Section 2.5.1). Test results are given in Figure 38. We defined the direction of the optical axis through the test chamber as $\varnothing = 0^\circ$. $\varnothing 90^\circ$ corresponds then with the observed flow propagation direction. Near the surface, a helium concentration of more than 90 % is measured. The helium layer concentrations were quite reproducible; test to test variations were within a few percent. A more uniform distribution is expected with the new design of the test chamber roof plate (see Fig. 3). There is a uniform Filtrokelit surface and an area with porous bronze (Poral) at the center and at the outer ring (see Fig. 21).

* W. Heilig, H.P. Mehlin, G. Gürke, G. Scheklinski-Glück, Ermittlung von HOB- und Tripelpunktstrajektoren, EMI Report E 26/85.

4.2.2 HOB Experiments.

4.2.2.1 Optical Measurements. Cinematographic picture series were taken with a Cordin camera. Two frames are shown in Figure 39 as examples. The formation of the precursor, the two triple points, the turning shock, the slip lines, the secondary shock, and other phenomena of the shock structure can be seen. The complete picture series visualizes the dynamic feature of the airblast precursor. A movie of cinematographic picture series with the Cordin camera was produced where each frame was copied with the individually corrected magnification factor. In the movie, each frame was repeated two times. The movie duration is therefore doubled without noticeable effect on the dynamic course of the precursor propagation.

The space and time resolution of the pictures is much higher in the single frame technique. Some examples are given in Figure 40 at different times after charge ignition. To demonstrate the difference of precursed and ideal HOB-shock structure, single frame pictures for both cases are shown. Notice that each picture corresponds to a new test.

In Figure 40a, the pictures are taken 180 μ s after charge ignition. The marks at the upper edge are 10 cm apart from each other. The Mach stem has developed at the nonprecursed blast (upper frame). The triple point is a little bit disturbed by a jet. The reflected wave and slipline are clearly visible. At the precursed flow (lower frame), the precursor inside the helium layer can be seen. The flow behind the tip of the precursor is laminar and then becomes turbulent. The turning shock and the two triple points have developed.

In Figure 40b, the delay time between ignition and exposure time is 220 μ s. The Mach stem in the nonprecursed blast is raised. The reflected shockwave at the triple point seems to be fan-shaped but it should be remembered that the flow field is three-dimensional. The secondary shock and its reflection at the bottom are visible. At the precursed blast (lower frame), the sliplines from the two triple points change from laminar to turbulent flow. The same mechanism starts to create the wall-jet as it is made visible in shock tube experiments. The roll-up of the helium layer and the formation of shocklets can be noticed.

Experiments at a delay time between ignition and exposure time of 250 μ s are shown in Figure 40c. The pictures are very similar to those of Figure 40b. Differences can be detected in the helium layer. The sensitivity of the shadow system at the lower frame was raised to optimize the resolution.

In Figure 40d, the delay time was 350 μ s. Because the reaction products of the charge lay behind the incident blast wave, more details can be seen in the flow field. Structures at the border of the layer are visible especially in the helium layer. The flow field behind the tip of the precursor is laminar at first. In the walljet the flow starts to get turbulent and develops small shock fronts.

The picture series in Figure 40 makes flow phenomena visible, phenomena which often can hardly be seen in free field tests. It should be mentioned, however, that the interpretation of photographs of three-dimensional events must be done very carefully.

The objective lense of a camera focuses the points of the object plane to the image plane. Normally, the density field (refraction index) is assumed to be homogenous. But in our HOB test, the light beams are traversing regions of inhomogenous density. So the optical copying process can be disturbed, especially if high density gradients are present. Figure 41 serves as an example. The upper frame shows a small cube. The edges are rectangular to each other. The cube has just been parted by the Mach stem of a nonprecursed blast. The edge is slightly deformed at the roof. A high deformation can be seen at the middle and lower frames. In this case, the cube is nearly completely embedded in the helium layer.

Figure 41 demonstrates that great care and experience are needed to interpret photographs of 3-D-events.

4.2.2.2 Pressure Measurements. As described in Section 2.3.2, pressure measurements were made for each test at 12 different locations. The helium layer has as a rule an extension of about 30 cm. This means that only gage No. 1 to gage No. 6 measured the surface pressure in the helium layer whereas gage No. 7 to gage No. 12 were located in the air layer (see Fig. 18). One can therefore expect to see in the pressure records the cleanup phase of the precursor. To compare the differences between ideal and precursed blast propagation in Figure 42, the pressure-time curves are superimposed. The dark curve belongs to the ideal

blast, measured at an HOB of 12.5 cm (test M 245) whereas the grey curve represents the pressure-time history of a precursed blast wave (test M 248).

At ground zero (Fig. 42; MK 1), we observe quite a different overpressure, 15 bars (ideal black) and 6.5 bars (precursed blast) respectively. As expected, the arrival time is shorter in the case of precursed blast.

At gage position No. 4 (Fig. 42; MK 4, 17.1 cm from GZ), the sharp peak disappears at the pressure curve of the precursed blast. The rise time of the precursor gets longer (Fig. 42; MK 6). We are now just at the border of the helium layer. The precursor shock decays more to a compression wave (Fig. 42; MK 7). The cleanup phase starts. At gage position No. 8 (Fig. 42; MK 8; 39.9 cm from GZ), the turning shock T (see Fig. 40) is reflected from the ground and creates a second peak. This shock becomes more dominant in the history of the surface pressure (compare Fig. 42; MK 9). The front of the precursor steepens more and more. At position No. 12 (Fig. 42; MK 12), the profiles of precursed and nonprecursed blast are nearly the same; only the time of arrival differs. The cleanup phase is now finished.

The impulse curves of ideal and precursed blast are quite similar. At precursed blast the impulse is always about 10 % - 20 % smaller than in the ideal case. Some examples are given in Figure 43. As in Figure 42, the records of tests M 245 and M 248 are compared.

The pressure measurements demonstrate the good reproducibility of the experiments with small charges of 0.6 g only. They also confirm the qualification of the tests for studying the cleanup phase of the precursor.

As a preliminary result, the peak overpressure versus ground range in the case of HOB = 12.5 cm is shown in Figure 44. Results are also included for smooth Al surface, rough (Filtrokelit) surface, and helium layer precursor. The helium stops at a ground range of about 30 cm. The reflected turning shock can be identified at a distance of about 40 cm. At the end of the runway it reaches about the same peak overpressure as the ideal blast.

Figure 44 demonstrates the wide variety of model tests that are applied to solve problems of precursed blast and to provide data for computer codes validation.

SECTION 5 SUMMARY AND CONCLUSIONS

SMALL-CHARGE DEVELOPMENT.

A new 0.6 g spherical charge of Nitro-Penta (NP) was developed. Also, a technique for precisely locating the detonator in the center of the charge was designed. A electrical energy source (~ 50 joules stored energy) was used to ignite the charge. This produced an overdriven detonation wave that successfully detonated the complete charge. The electrical energy coupled into the charge was less than 25 joules (compared to chemical energy of 1756 joules).

5.2 BLAST WAVE DRIVEN BY NP CHARGE.

High speed photography revealed that the charges produced a smooth spherical blast wave. The secondary shock characteristic of HE-driven blast waves is also evident in photographs.

The photography revealed some jetting effects that are present in all HE charges (due to Rayleigh-Taylor instabilities); however, these jets were no worse than those found in larger HE tests. In the lower pressure regimes of interest here, such effects were small and could be overcome by performing additional tests when required.

5.3 BLAST WAVE SCALE.

The blast wave scale was established by two methods based on the "Time-Distance" curve for the free-air burst (as measured from the high-speed cinematography).

Method 1: compare NP time-distance curve with a standard TNT curve

Method 2: differentiate X-t curve to give shock Mach number and peak pressure; compare the pressure-range curve with a standard TNT curve.

In addition, a third method was used; the HOB curve of the NP charge was compared with results from an RDX charge at the same scaled HOB. Thus the following HE scale factors were established:

$$\begin{aligned} \text{SF} &= 1.4 \quad (\text{TNT}) \\ &= 0.7 \quad (\text{RDX}) \end{aligned}$$

5.4 INSTRUMENTATION FOR THE HEIGHT-OF-BURST TESTS.

Two schlieren/shadowgraph photography systems were developed. One was a single-frame system for high space and time resolution, and the other was an 80-frame cinematographic system using a Cordin rotating mirror camera and a specially designed long-duration spark light source.

The high-speed photography made visible the unique features of HE-driven spherical blast waves reflecting from plane surfaces. These included the shock structure, slip lines, and turbulent flow features. In particular, the secondary shock S and its reflection from the surface and interaction with shock R was made visible for the first time (this shock is not visible on large field tests because the detonation products are optically dense and the scale is too large).

A high-speed recording system was developed that is capable of accurately measuring such short duration (30 to 300 μs) pressure waves. The pressure records are self-consistent and demonstrate that the tests are reproducible within a few percent. This system can be used to give an accurate characterization of near-surface blast wave environments, for example:

- (i) static pressure histories
- (ii) time of arrival curves
- (iii) peak pressure vs range curves
- (iv) impulse curves
- (v) positive phase duration curves

In addition, the photography can be synchronized with the charge detonation and pressure-recording system to elucidate particular flow regions of interest.

5.5 IDEAL HEIGHT-OF-BURST RESULTS.

This small-charge technique can be used to quantitatively study blast reflections over smooth (ideal) surfaces. The HOB can be easily varied over the range of 3 cm to 40 cm; this corresponds to 100 ft to 1200 ft HOB on a kiloton basis.

A parametric series of such tests was performed with the 0.6 g NP charges. The results were scaled (based on the above-mentioned scale factor). The resulting HOB curves were in excellent agreement with the large-charge data (e.g., 1 kg RDX charges).

Such comparisons demonstrate and confirm the validity of using this small-charge technology for accurately studying HE blast reflections in the low pressure regime (100 psi to 2 psi).

The obvious advantages of this approach are: (1) the well-controlled laboratory conditions (no wind or terrain effects, etc.); (2) parametric tests can be performed in a cost-effective manner; and (3) such parametric results can be used to statistically analyze blast environments to evaluate not only the mean values, but also the standard deviations of the results.

5.6 HEIGHT-OF-BURST TESTS OVER ROUGH SURFACES.

Height of burst tests were also conducted over a porous ceramic (Filtrokelit) plate. Surface roughness was approximately 30 μ m (3 cm on a kiloton basis). When compared with the smooth-surface results, systematic trends were found for the "rough surface" results:

- delayed shock arrival
- reduced peak overpressure
- reduced overpressure impulse (-10 % to -20 %)

These effects were reduced by increasing the height of burst.

These small-charge experiments then offer an effective technique for parametrically studying surface roughness (i.e., boundary layer) effects on reflected blast wave environments.

5.7 HELIUM LAYER PRECURSOR TESTS.

A new method was developed to create reproducible "pancake-shaped" helium layers applicable to height-of-burst tests. This involves the transient development of a helium layer forced through a porous ceramic (Filtrokelit) surface.

Specialized anemometry probes were also developed to experimentally map the helium concentration throughout the layer. High concentrations of helium (92 to 96 %) were successfully measured near the surface (0 to 2 mm).

The high-speed photography revealed many of the dynamic features of airblast precursors for the height of burst geometry. These features include the formation of the precursor shock structure and associated slip lines, the development of the turbulent wall jet, and the precursor cleanup.

Overpressure histories were also measured on these tests. Comparison with ideal surface results indicate the following:

- (1.) Strong precursor effects were evident; precursor arrival times were as much as $160 \mu\text{s}$ (or $160 \text{ ms}/KT^{1/3}$) ahead of the ideal surface results.
- (2.) Peak pressures were reduced, but no classic second peak was found in the strong precursor region.
- (3.) The precursor cleanup phase was well simulated. The precursor shock decayed to a compression wave at $GR \approx 23 \text{ cm}$ ($680 \text{ ft}/KT^{1/3}$); by $GR \approx 40 \text{ cm}$ ($1200 \text{ ft}/KT^{1/3}$) the T-shock reflected from the ground, creating a second peak. At far ground ranges the overpressure of this shock approached the ideal surface results.
- (4.) Positive phase impulses were reduced by 10 to 20 % because of the precursor effect.

These results were self-consistent and quite reproducible.

These experiments indicate that this small-charge technique can be used to parametrically study precursor effects, particularly in the cleanup region, as a function of height of burst. Noteworthy advantages of this approach are:

- (1) A circular "pancake-shaped" layer is used so that the flow field is symmetrical (i.e., there are no edge effects as in the large field tests).
- (2) No membrane is needed to form the helium layer; thus flow develops naturally and is not disturbed by membrane fragments.
- (3) Parametric precursor tests are practical, and may be used to statistically analyze precursor environments, not only the mean values but also the standard deviations of the results.

SECTION 6 RECOMMENDATIONS

Based on the above demonstrated successes of this small-charge technique, the following experiments are recommended:

1. Perform a parametric series of HOB tests over a smooth surface, to establish the ideal HE height-of-burst curves for low pressures (100 psi to 2 psi). Use statistical analysis to establish mean curves and standard deviations.
2. Perform a similar series of HOB tests over one (or more) rough surfaces to evaluate boundary layer/roughness effects.
3. Perform a similar series of HOB tests over a helium layer to investigate precursor cleanup effects. Complementary shock tube precursor tests can be used to investigate the fluid mechanics of precursor wall jets under more simplified conditions.

In addition, the small-charge technique can be used to investigate other blast reflection phenomena. Atmospheric inversions can be easily created by this experimental method (e.g., by using thick, dense gas layers) to investigate inversion effects on HOB curves. Also, multiple burst explosions can be simulated by replacing symmetry lines between charges with reflecting plane surfaces, and examining airblast cumulation effects near the center of symmetry.

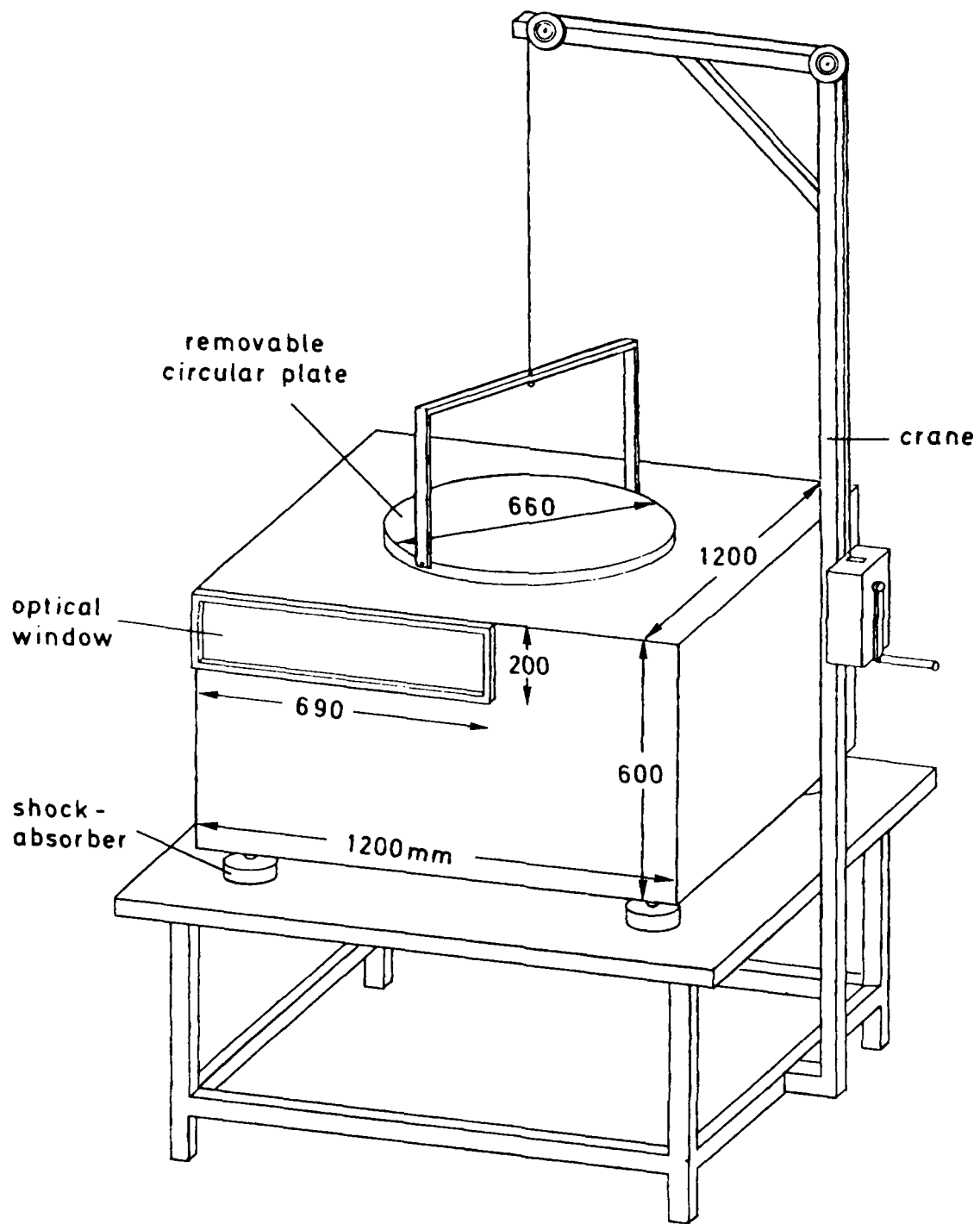


Figure 1. Test chamber for Micro-Mach experiments.



Figure 2. Overview picture of the test chamber.

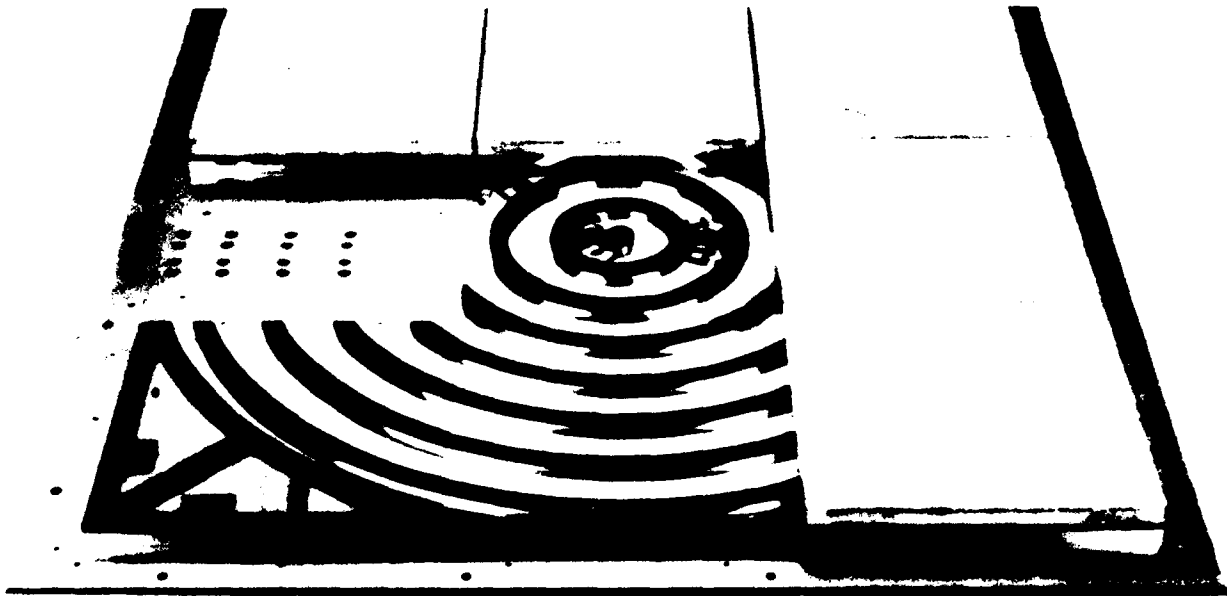


Figure 3. New design of the roof plate.

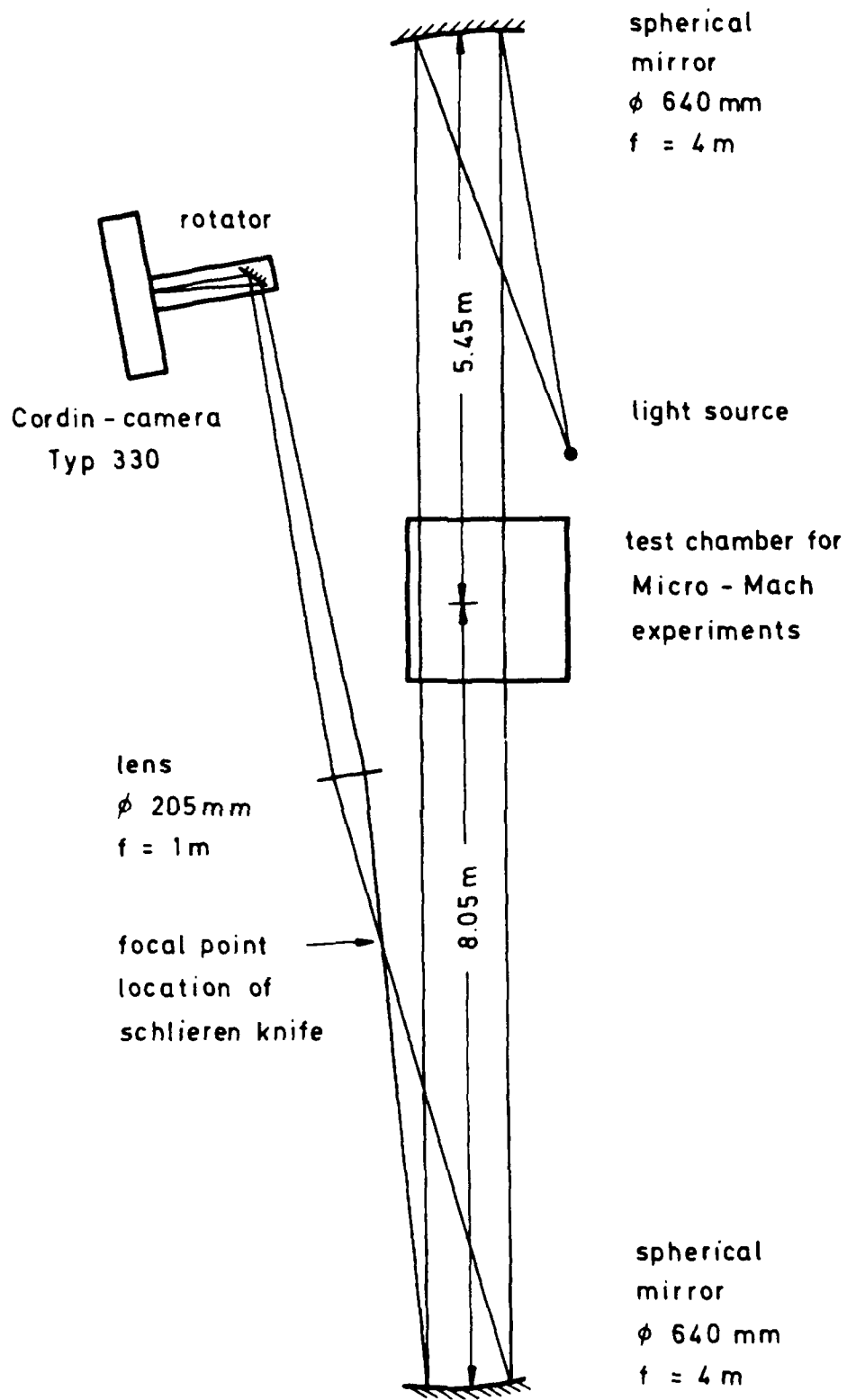


Figure 4. Optical setup for high speed camera pictures.

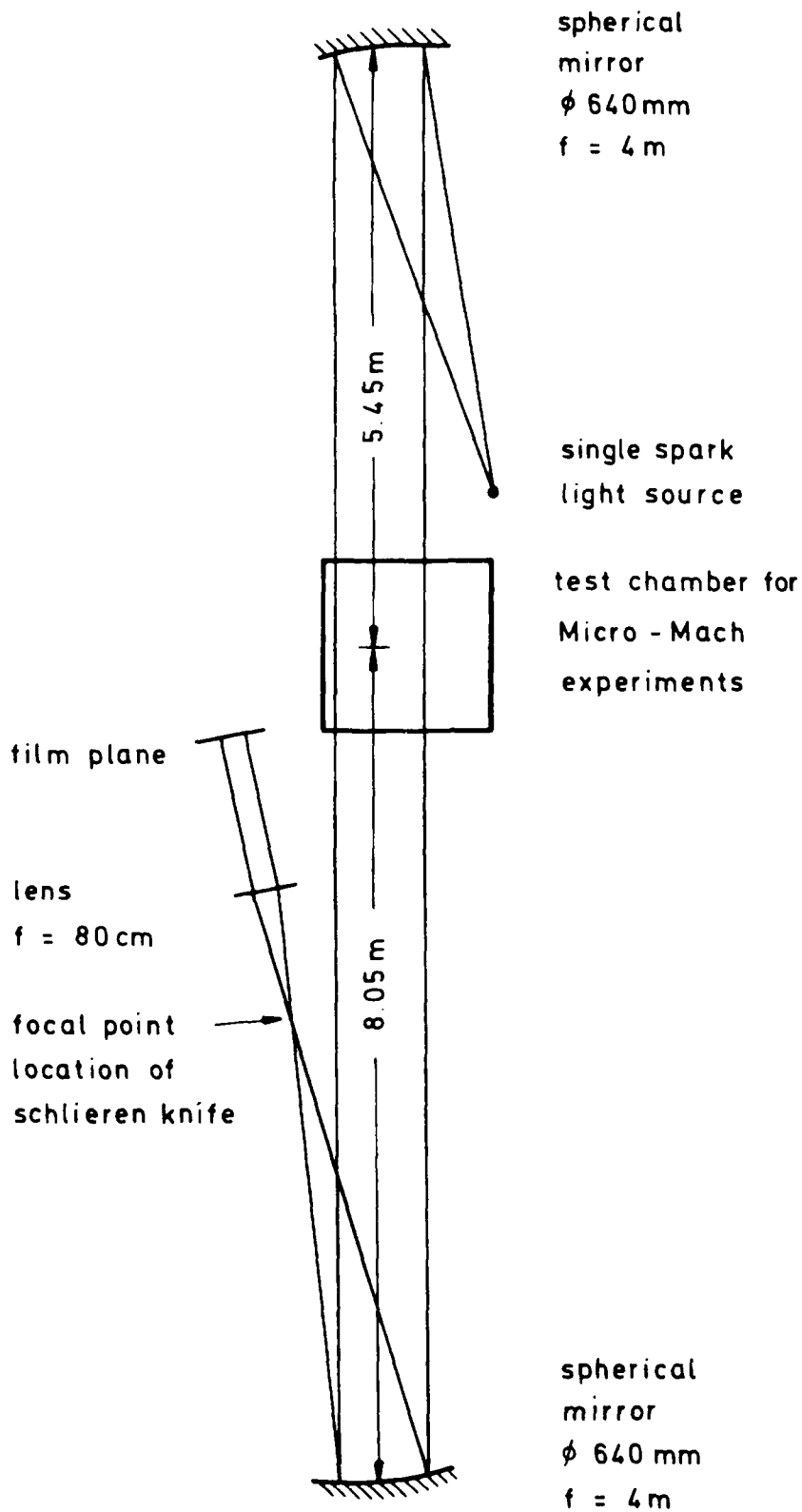


Figure 5. Optical setup for single frame pictures.

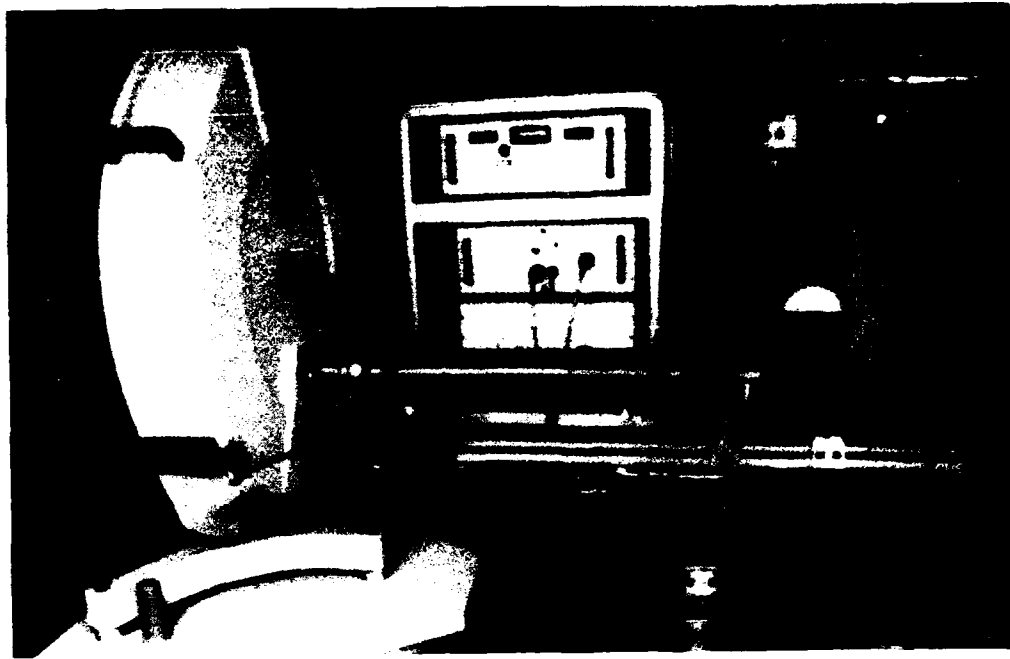


Figure 6. Cordin camera with rotator and control unit.

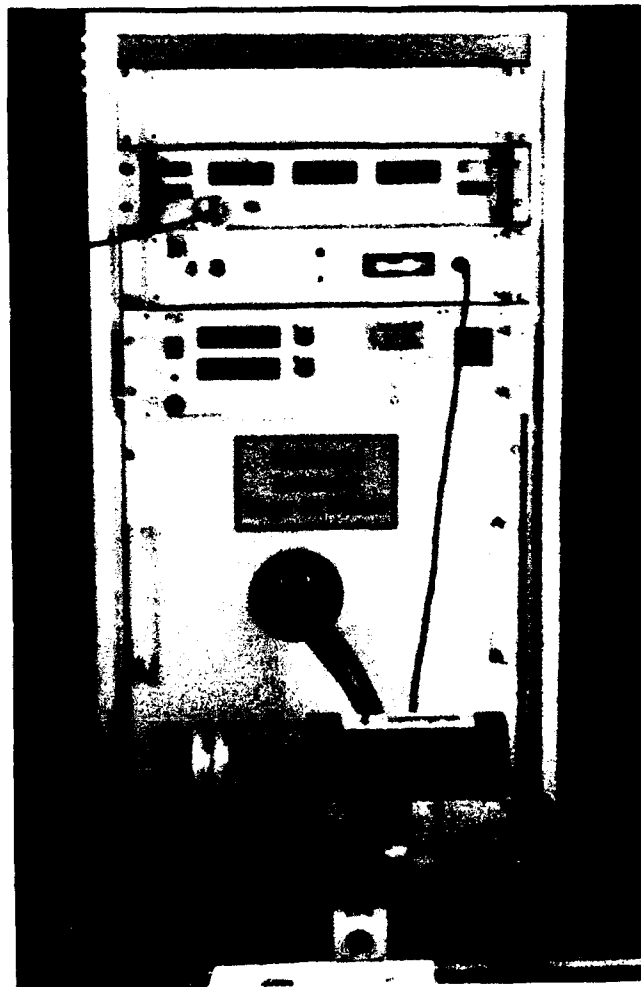


Figure 7. Light source with light output between 40 μ s and 700 μ s in the form of a square wave pulse. Energy source, pulse former, trigger, and delay circuits are installed in their own cabinet.

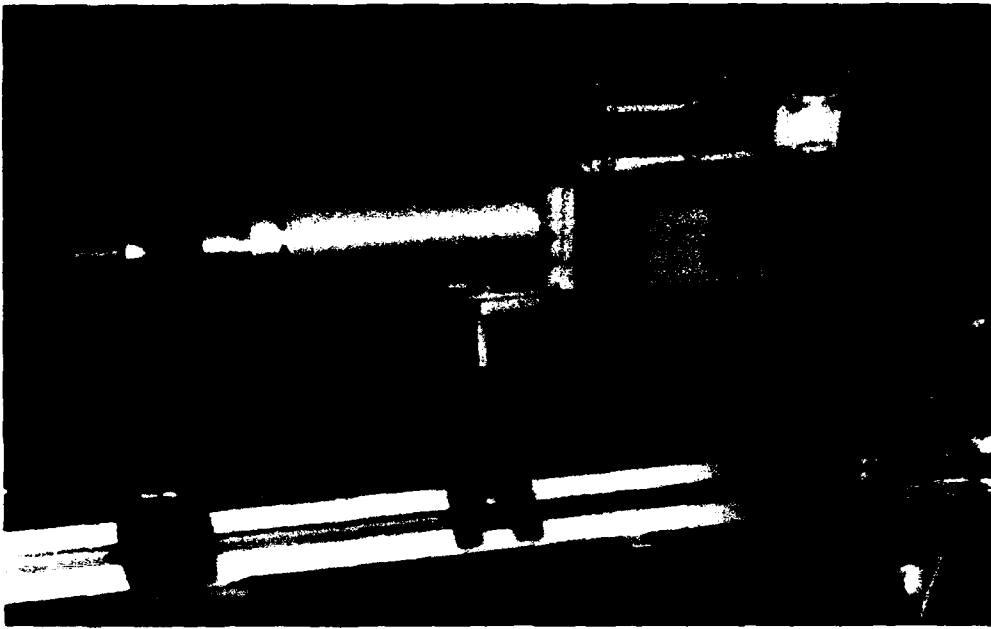


Figure 8. EMI single spark point light source. Power supply and trigger are integrated in a single box. Exposure time: 0.3 μ s.

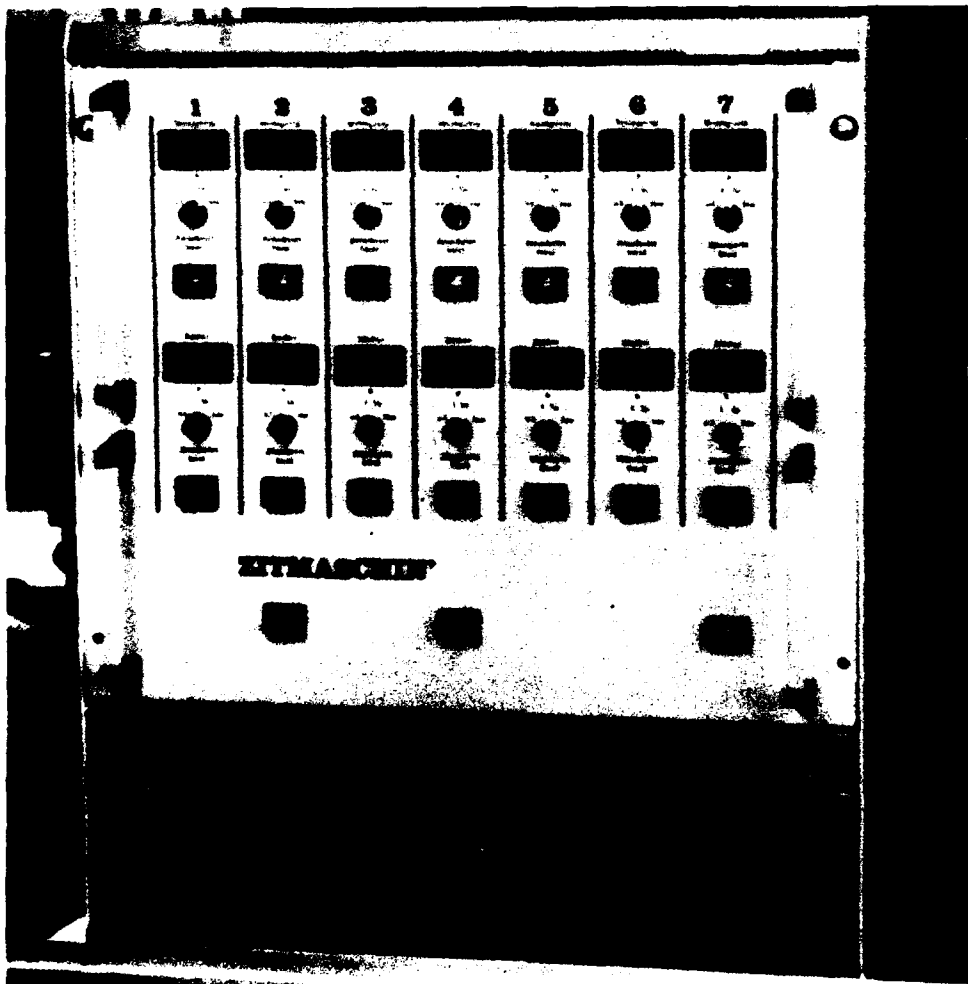


Figure 9. 7-channel timing unit.

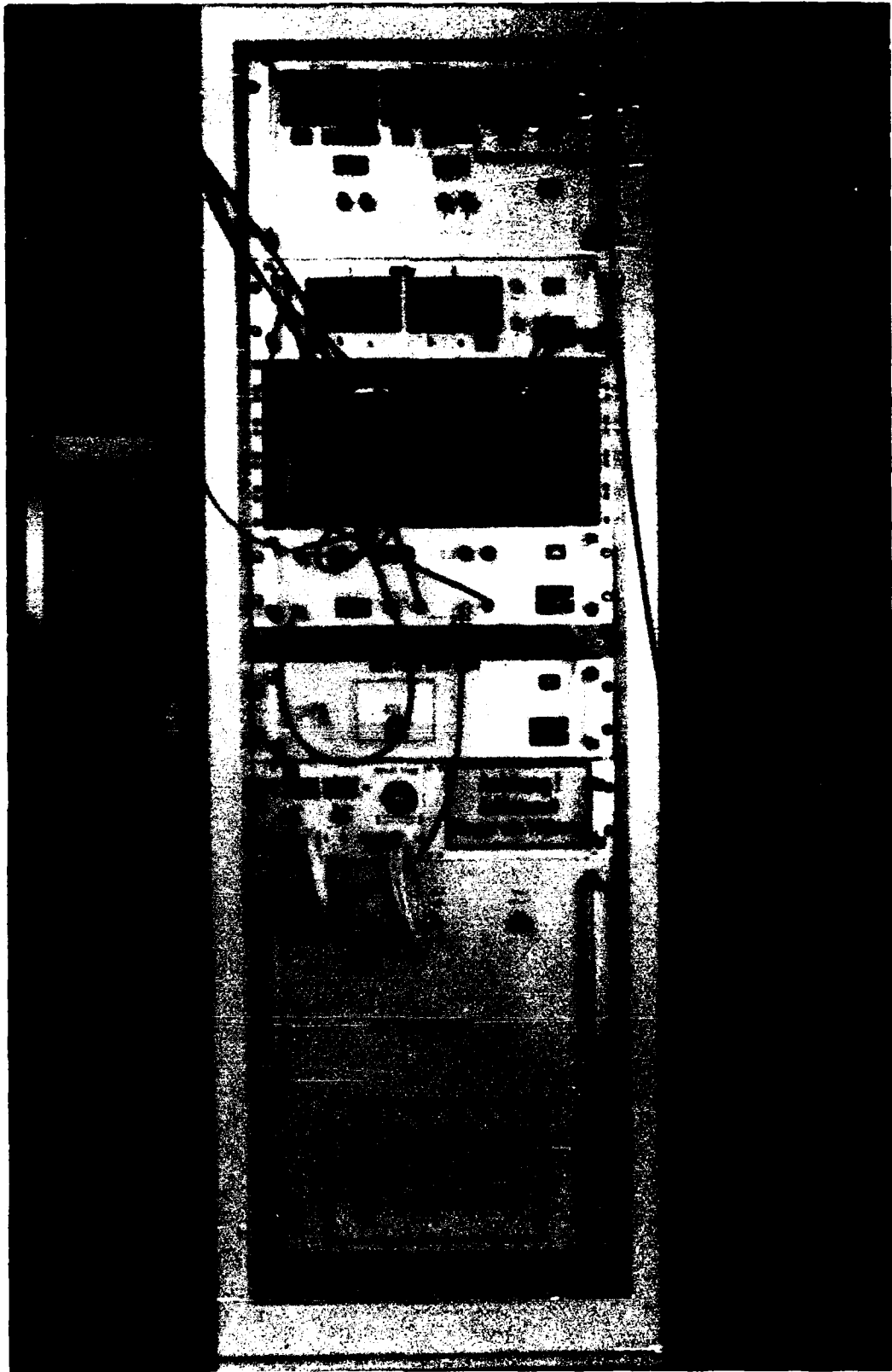


Figure 10. Charge ignition unit with trigger and delay device.

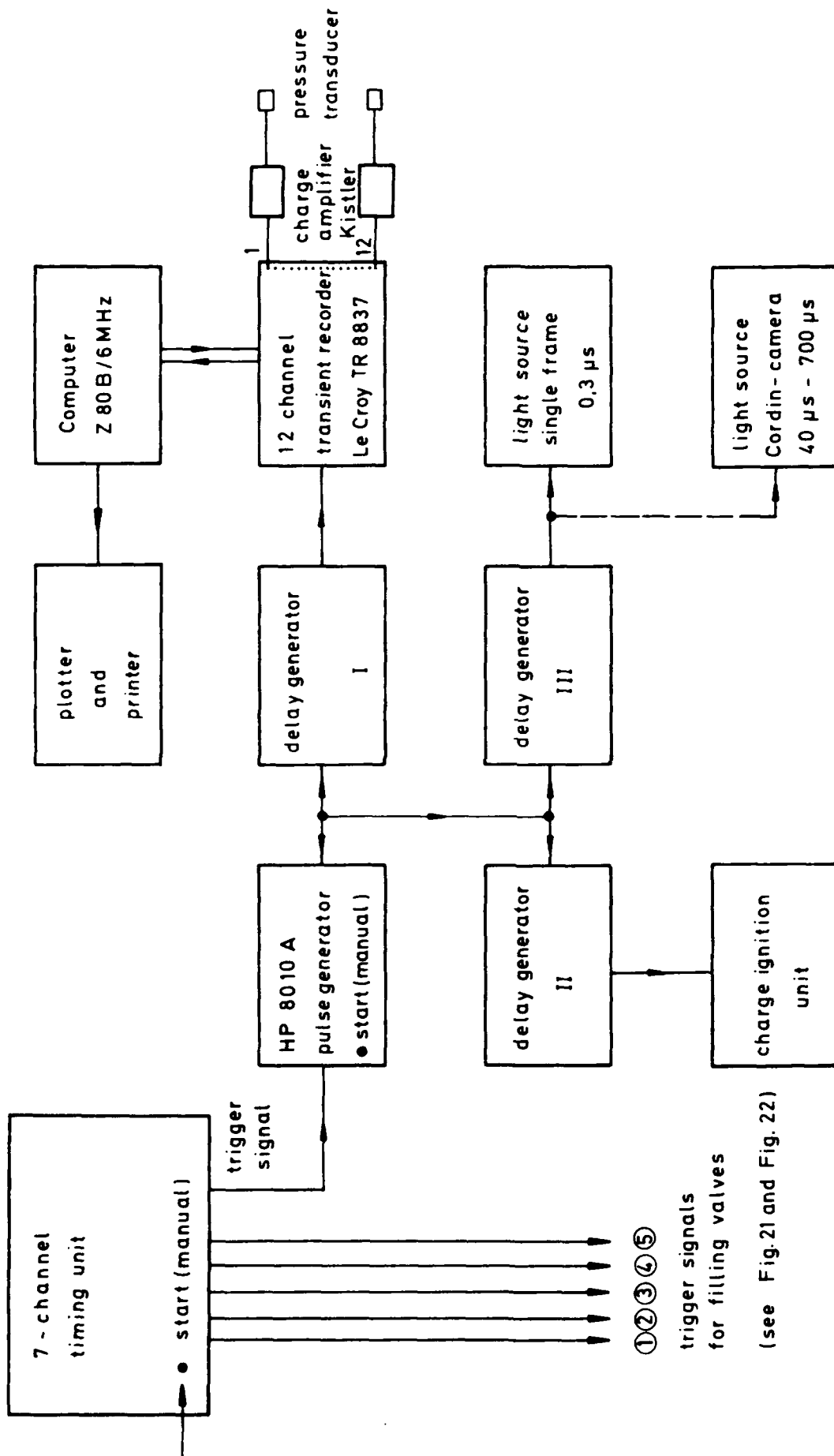


Figure 11. Circuit diagram of the electronic equipment.

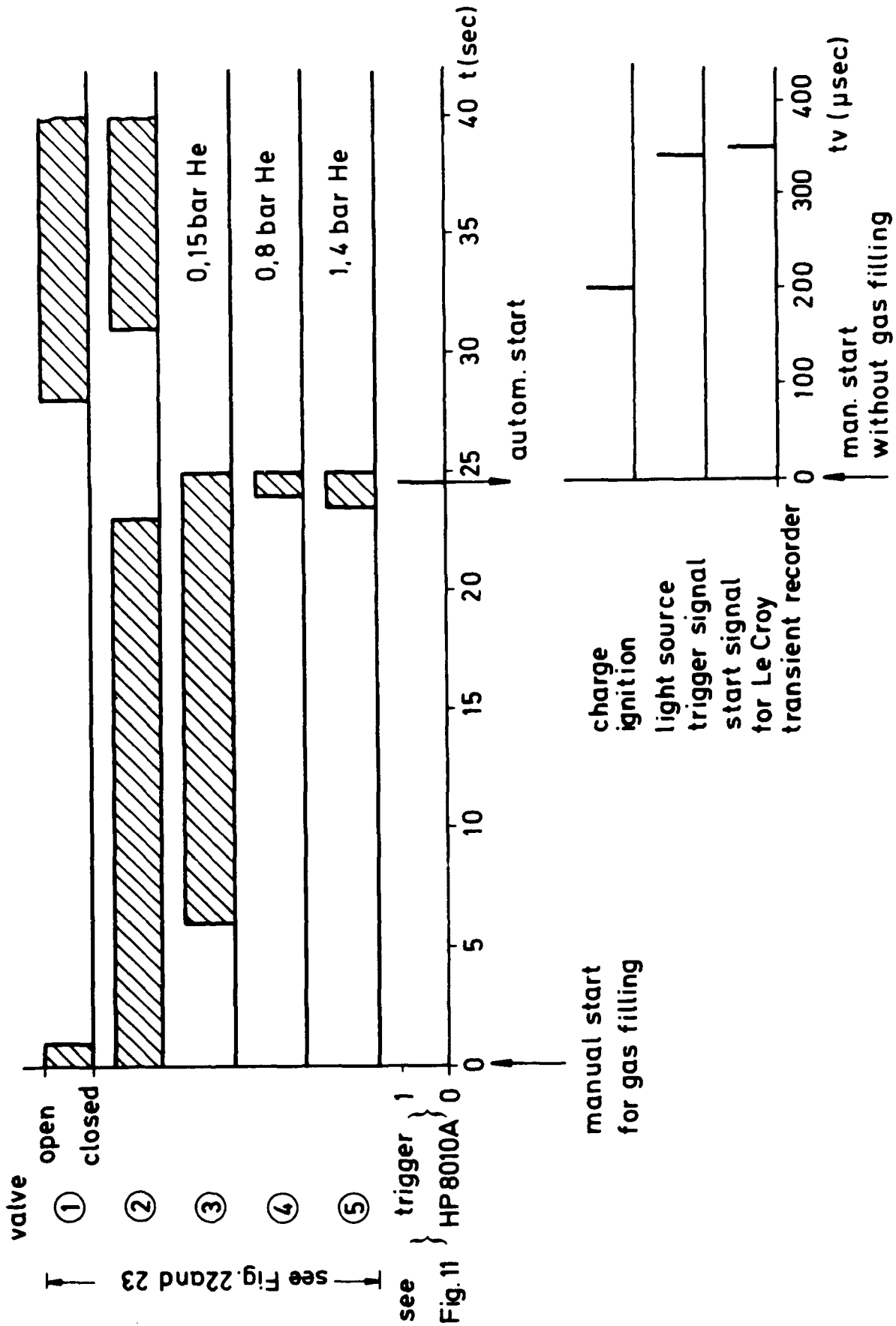


Figure 12. Timing diagram for single spark photography. The given helium pressures are measured in the helium lines (Fig. 23). The diagram portrays test M 0228.

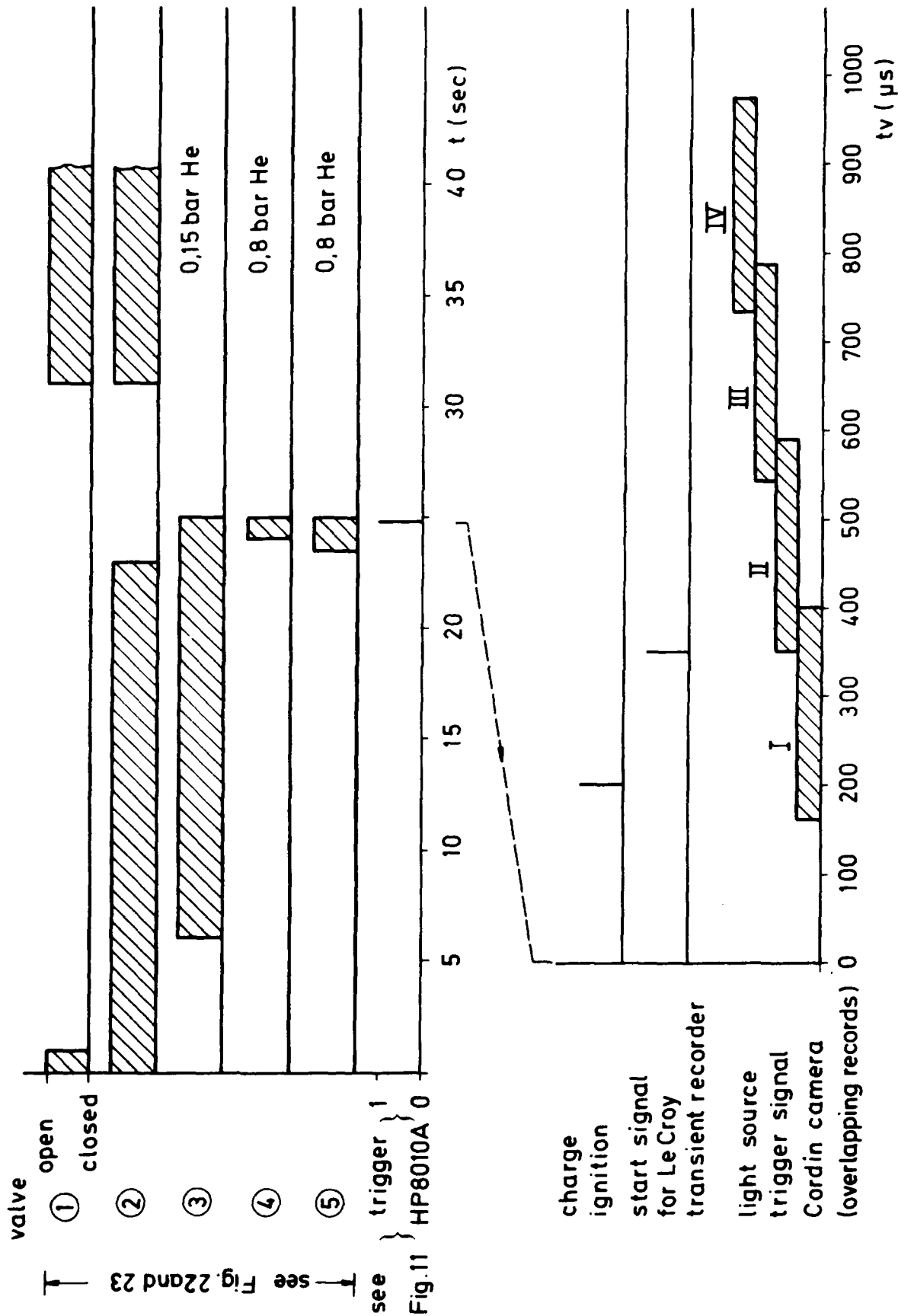
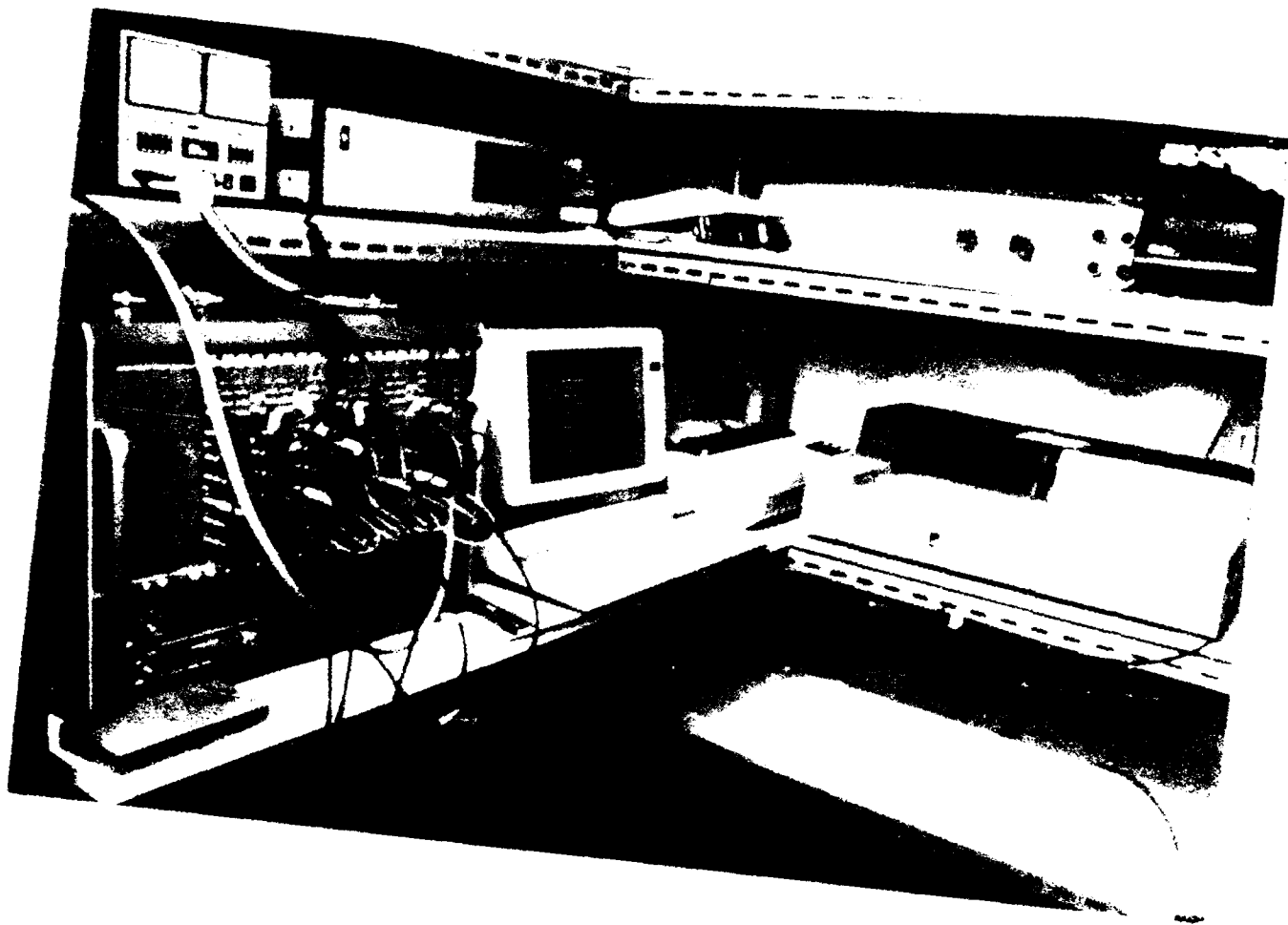
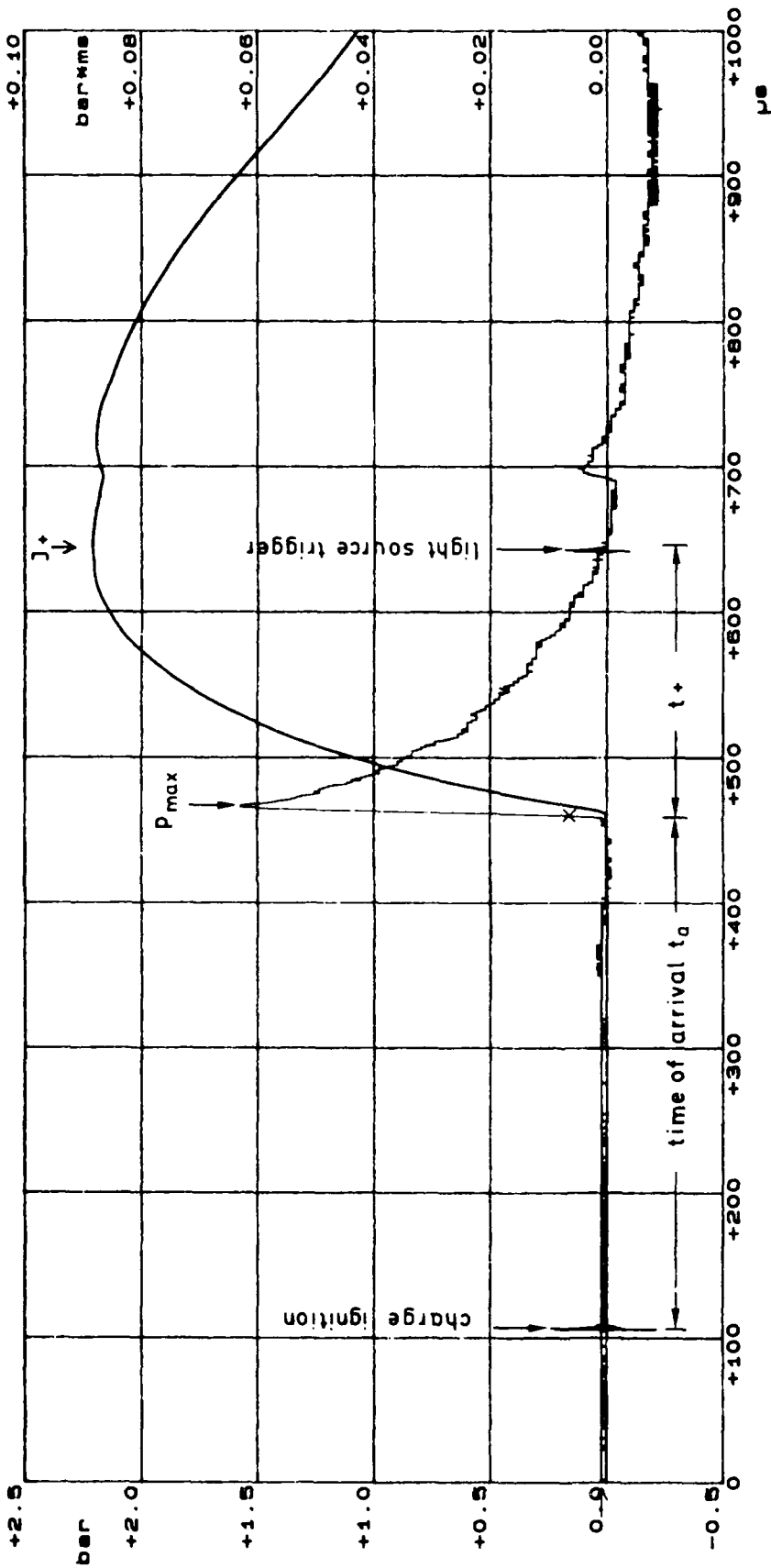


Figure 13. Timing diagram for Cordin camera records. The given helium pressures are measured in the helium lines (Fig. 23). The diagram portrays tests M0246 - M0249 (overlapping records).



Pressure recording system. On the left: 12-channel LeCroy transient recorder with calibration device and computer. On the right: printer and plotter. The recording system is installed in a Faraday cage.



024505.KMM Mk5 1bar pro V am 5001
 24.03.88

I+ = +0.088 bar*ms
 t+ = +183.750 μs
 t_a = +354.250 μs (+150.0 Verz. -Pretrigg.)
 pmax = +1.55 bar

Figure 15. Example of a pressure record. Charge ignition signal and light source trigger signal are visible. The second curve gives the overpressure impulse, $I = \int \Delta p dt$. The data for peak overpressure, maximum impulse, time of arrival, and positive duration are printed automatically in the diagram.

Versuchs - Nr.: 0240		Gruppe MM		Datum/Uhrzeit		24.10.1987/07:40:37	
Panel - Nr.	03	04	03	04	03	04	04
Fenster (ps)	500	500	500	500	500	500	500
Memory (Bytes)	8	8	8	8	8	8	8
Frequenz/Teiler	274	274	274	274	274	274	274
Freitrigger	278	278	278	278	278	278	278
Verst. Bereich	10 V	10 V	5 V	5 V	10 V	10 V	10 V
Offset	0.00	0.00	0.00	0.00	0.00	0.00	0.00
Eingang	1 M Ω DC	1 M Ω DC	1 M Ω DC	1 M Ω DC	1 M Ω DC	1 M Ω DC	1 M Ω DC
Filter	20 MHz	20 MHz	20 MHz	20 MHz	20 MHz	20 MHz	20 MHz
Trigg. Quelle	ext. $\pm 2V$	ext. $\pm 2V$	ext. $\pm 2V$	ext. $\pm 2V$	ext. $\pm 2V$	ext. $\pm 2V$	ext. $\pm 2V$
Schwelle	1.0	1.0	1.0	1.0	1.0	1.0	1.0
Flanke	pos.	pos.	pos.	pos.	pos.	pos.	pos.
Fopplung	0	0	0	0	0	0	0
Messbereich	20	5	5	5	20	20	20
Einheit	bar	bar	bar	bar	bar	bar	bar
Fal.-Zeit Null	14:50:10	14:50:11	14:50:14	14:50:17	14:50:19	14:50:22	14:50:27
Fal.-Zeit Voll	14:50:48	14:50:40	14:50:14	14:50:14	14:50:14	14:50:14	14:50:14
Fal.-Wert Null	41	34	31	35	35	35	35
Fal.-Wert Voll	140	223	180	180	180	180	180

Versuchs - Nr.: 0240		Gruppe MM		Datum/Uhrzeit		24.10.1987/07:40:37	
Panel - Nr.	05	05	07	08	05	08	08
Fenster (ps)	1000	1000	1000	1000	1000	1000	1000
Memory (Bytes)	8	8	8	8	8	8	8
Frequenz/Teiler	274	274	274	274	274	274	274
Freitrigger	278	278	278	278	278	278	278
Verst. Bereich	5 V	2.5 V	1.0 V	1.0 V	1.0 V	1.0 V	1.0 V
Offset	0.00	0.00	0.00	0.00	0.00	0.00	0.00
Eingang	1 M Ω DC	1 M Ω DC	1 M Ω DC	1 M Ω DC	1 M Ω DC	1 M Ω DC	1 M Ω DC
Filter	20 MHz	20 MHz	20 MHz	20 MHz	20 MHz	20 MHz	20 MHz
Trigg. Quelle	ext. $\pm 2V$	ext. $\pm 2V$	ext. $\pm 2V$	ext. $\pm 2V$	ext. $\pm 2V$	ext. $\pm 2V$	ext. $\pm 2V$
Schwelle	1.0	1.0	1.0	1.0	1.0	1.0	1.0
Flanke	pos.	pos.	pos.	pos.	pos.	pos.	pos.
Fopplung	DC	DC	DC	DC	DC	DC	DC
Messbereich	1	2	300	600	600	600	600
Einheit	bar	bar	mbar	mbar	mbar	mbar	mbar
Fal.-Zeit Null	14:50:40	14:50:44	14:50:47	14:50:50	14:50:50	14:50:50	14:50:50
Fal.-Zeit Voll	14:50:45	14:50:05	14:50:40	14:50:58	14:50:58	14:50:58	14:50:58
Fal.-Wert Null	41	41	37	38	38	38	38
Fal.-Wert Voll	190	240	235	186	186	186	186

Versuchs - Nr.: 0245		Gruppe MM		Datum/Uhrzeit		24.10.1987/07:40:37	
Panel - Nr.	07	10	11	12	07	12	12
Fenster (ps)	2048	2048	2048	2048	2048	2048	2048
Memory (Bytes)	8	8	8	8	8	8	8
Frequenz/Teiler	274	274	274	274	274	274	274
Freitrigger	278	278	278	278	278	278	278
Verst. Bereich	1.0 V	500 mV	500 mV	500 mV	500 mV	500 mV	500 mV
Offset	0.00	0.00	0.00	0.00	0.00	0.00	0.00
Eingang	1 M Ω DC	1 M Ω DC	1 M Ω DC	1 M Ω DC	1 M Ω DC	1 M Ω DC	1 M Ω DC
Filter	20 MHz	20 MHz	20 MHz	20 MHz	20 MHz	20 MHz	20 MHz
Trigg. Quelle	ext. $\pm 2V$	ext. $\pm 2V$	ext. $\pm 2V$	ext. $\pm 2V$	ext. $\pm 2V$	ext. $\pm 2V$	ext. $\pm 2V$
Schwelle	1.0	1.0	1.0	1.0	1.0	1.0	1.0
Flanke	pos.	pos.	pos.	pos.	pos.	pos.	pos.
Fopplung	DC	DC	DC	DC	DC	DC	DC
Messbereich	600	400	300	300	300	300	300
Einheit	mbar	mbar	mbar	mbar	mbar	mbar	mbar
Fal.-Zeit Null	14:50:53	14:50:55	14:51:00	14:51:00	14:51:00	14:51:00	14:51:00
Fal.-Zeit Voll	14:04:05	14:50:40	14:50:58	14:50:58	14:50:58	14:50:58	14:50:58
Fal.-Wert Null	35	32	38	38	38	38	38
Fal.-Wert Voll	187	235	187	184	184	184	184

Figure 16. Example of a data summary sheet. After each test the sheet is printed with the calibration data of the 12 measuring channels.

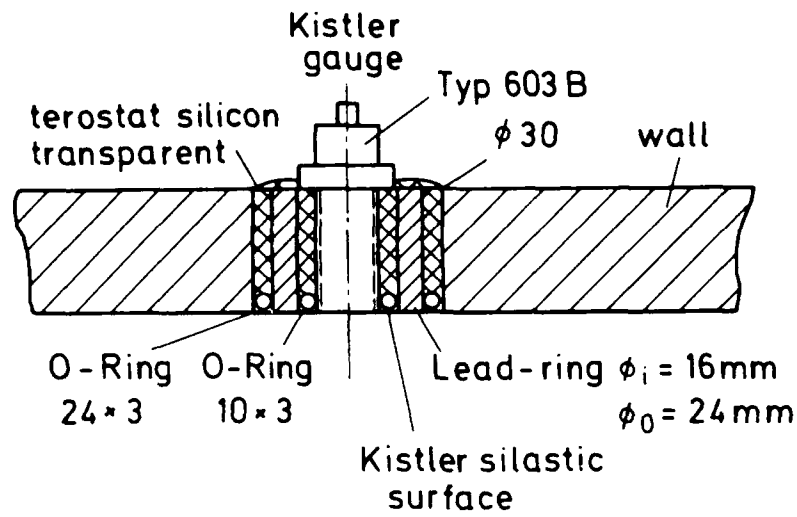


Figure 17. Transducer mounting for vibration damping.

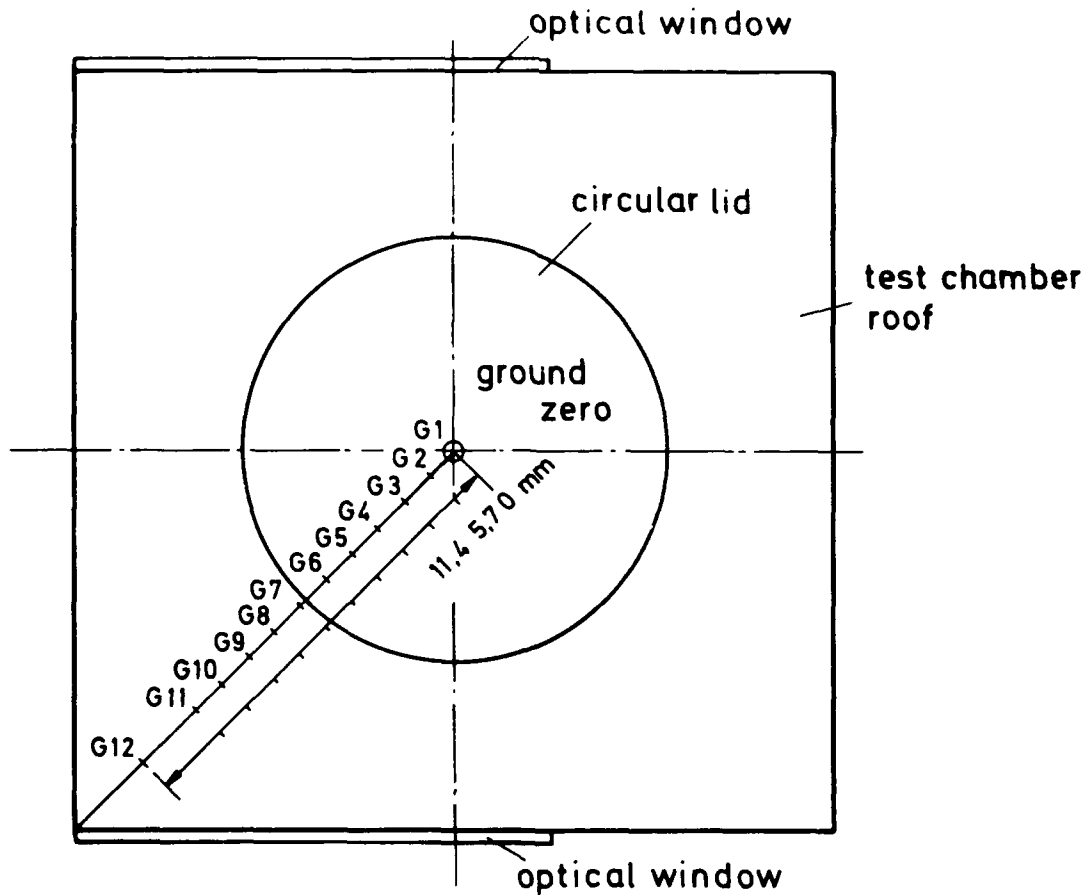


Figure 18. Location of the transducers. Top view of the test chamber $G_1 \dots G_{12}$ = gauge location. Distance between two gauges 5.7 cm (11.4 cm between G_{11} and G_{12}). See also Figure 20.

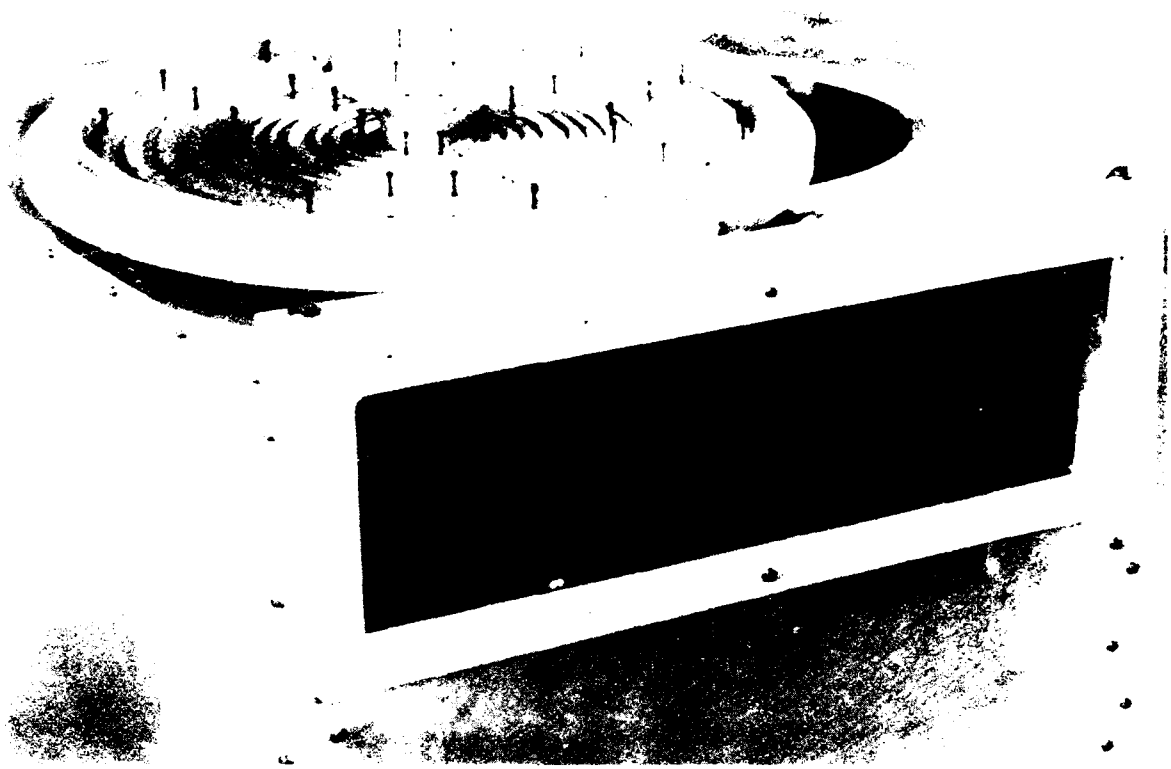


Figure 1. The top of the test chamber is partly shown. The different grooves are for the air and the water, which serve to fix the ultraviolet plate.



Figure 2. The top of the helium filling system. Some tubes are removed for a better overview. The position of the pressure transducer is at the lower left of the picture.

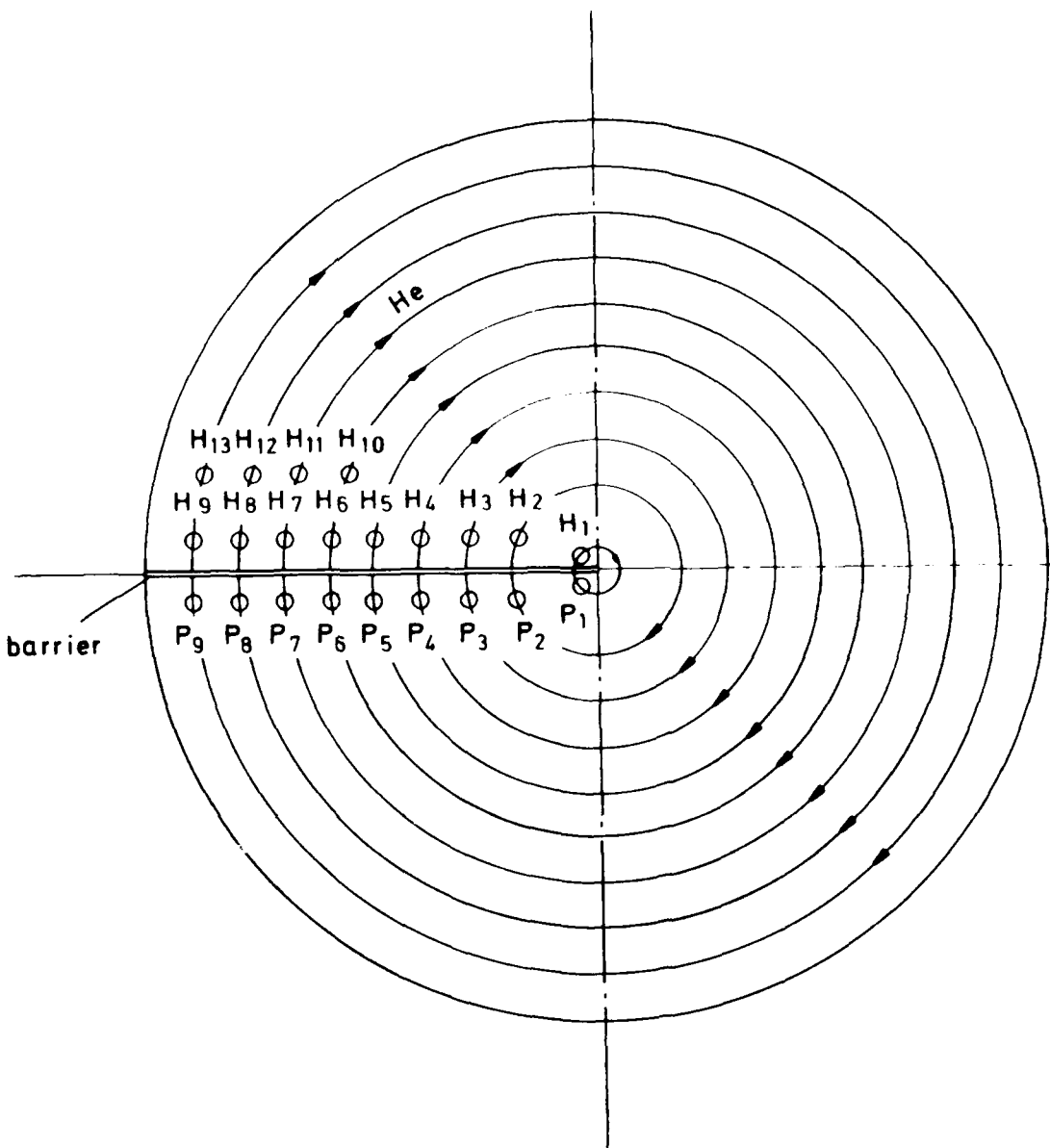
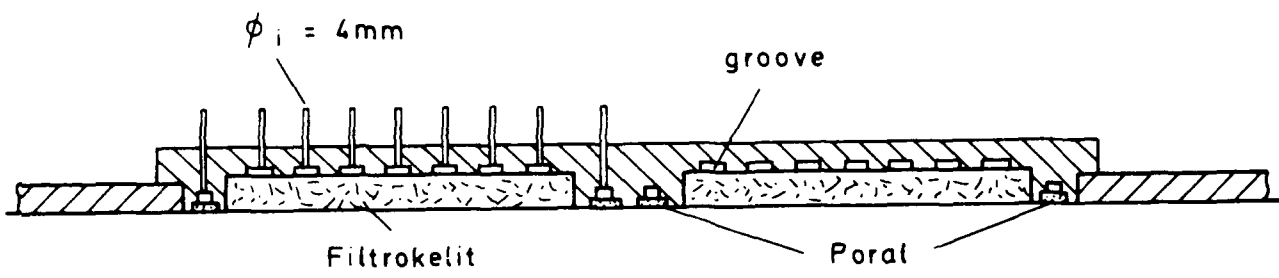


Figure 21. Side and top view of the bore holes in the lid of the test chamber.

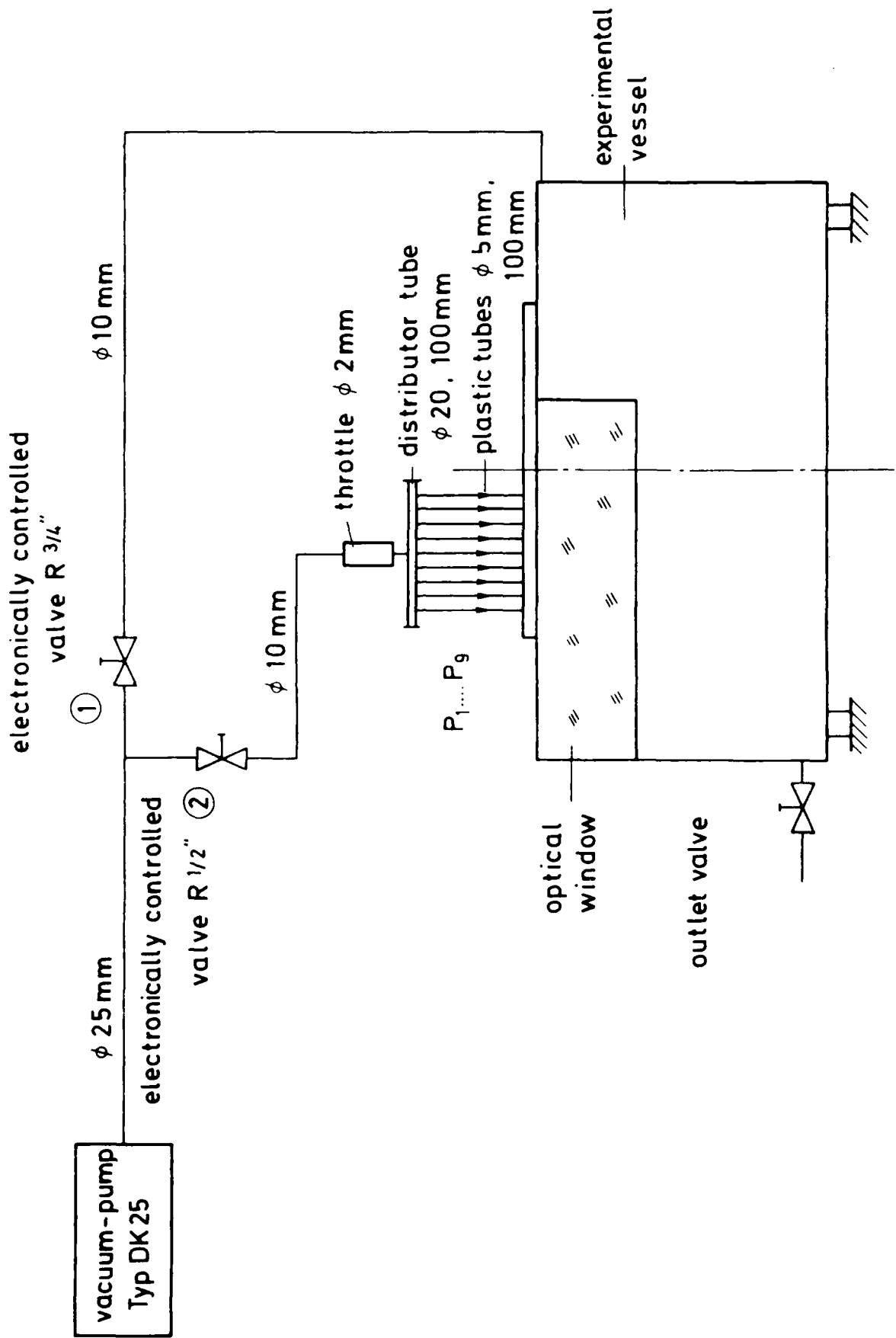


Figure 22. Pumping system (see also Fig. 11, Fig. 12, Fig. 13, Fig. 21).

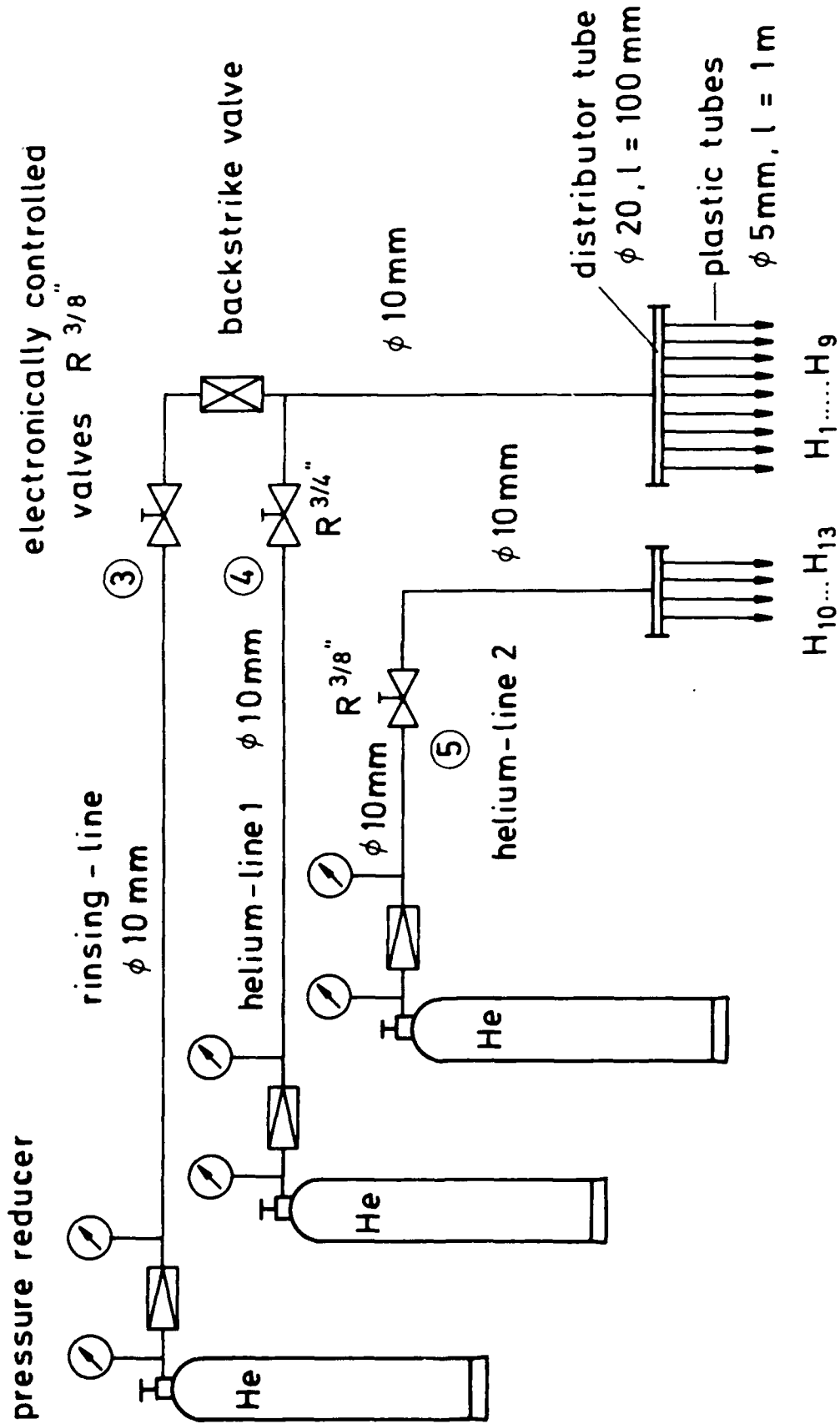


Figure 23. Helium rinsing and filling system (see also Fig. 11, Fig. 12, Fig. 13, Fig. 21).

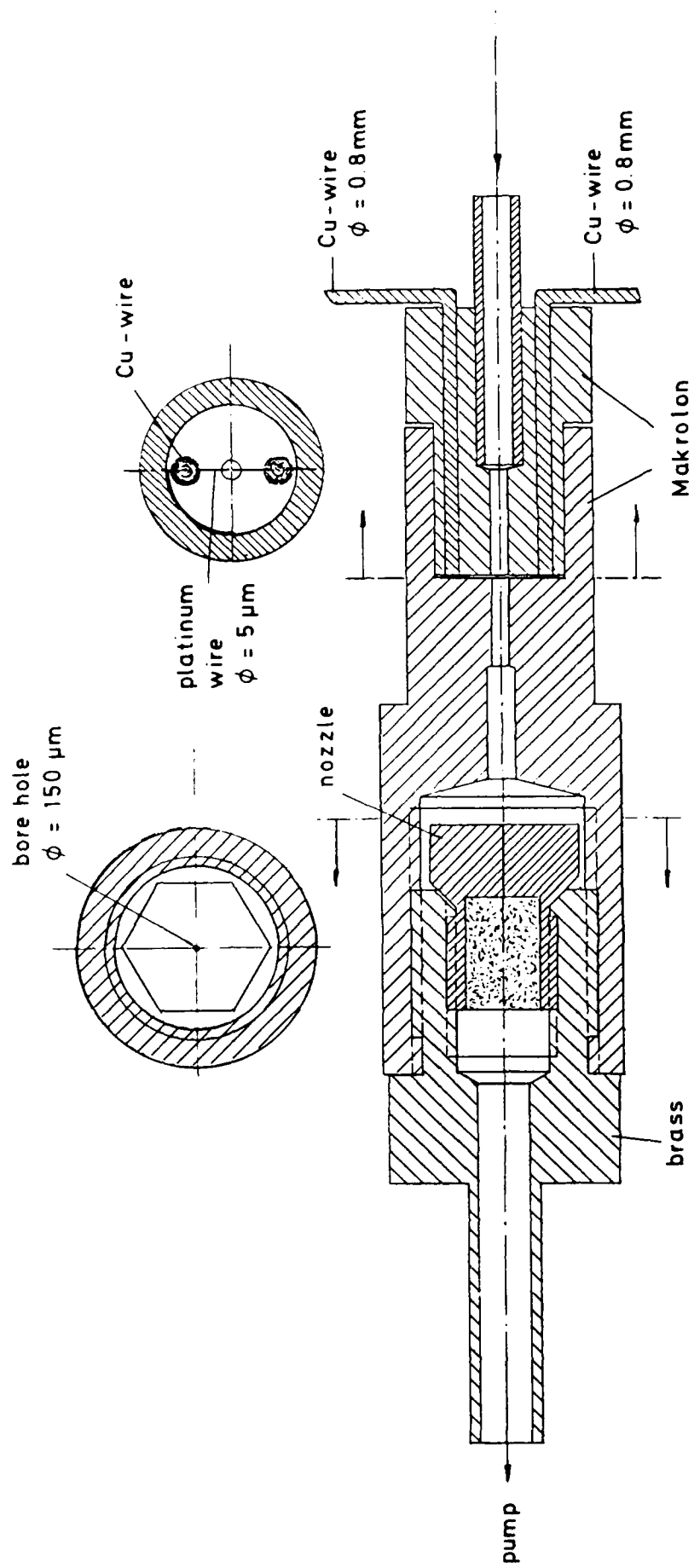
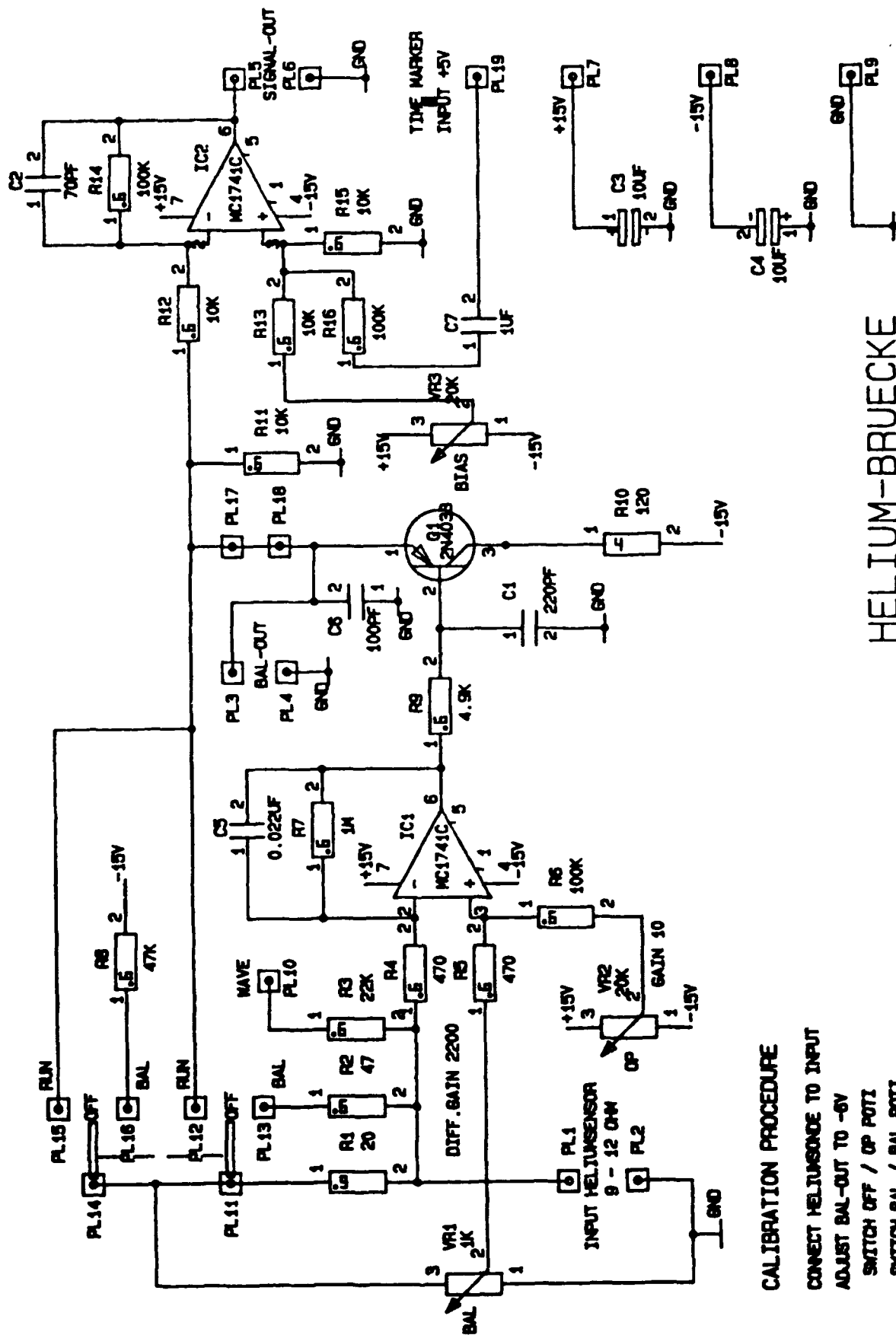


Figure 24. Construction of the helium probe.



HELIUM-BRUECKE

CALIBRATION PROCEDURE
 CONNECT HELIUMSND TO INPUT
 ADJUST BAL-OUT TO -6V
 SWITCH OFF / OP POTTI
 SWITCH BAL / BAL POTTI


09.05.88 J.B.HAGELWEIDE  FL21
 FL20

Figure 25. Circuit diagram of the electronic bridge of the helium probe.

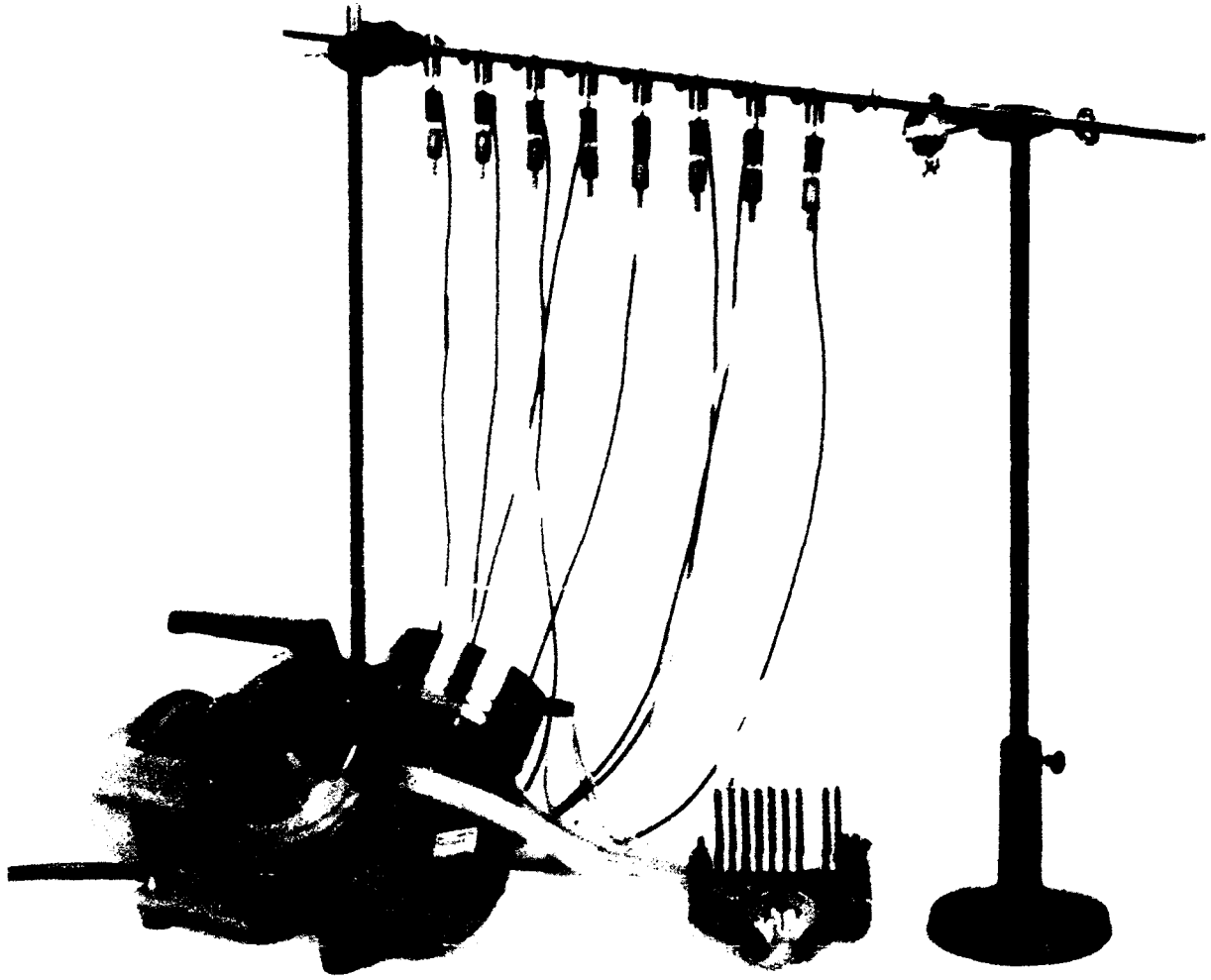


Figure 26. 8-channel He-concentration measuring arrangement.

Calibration Curve for He - Probes

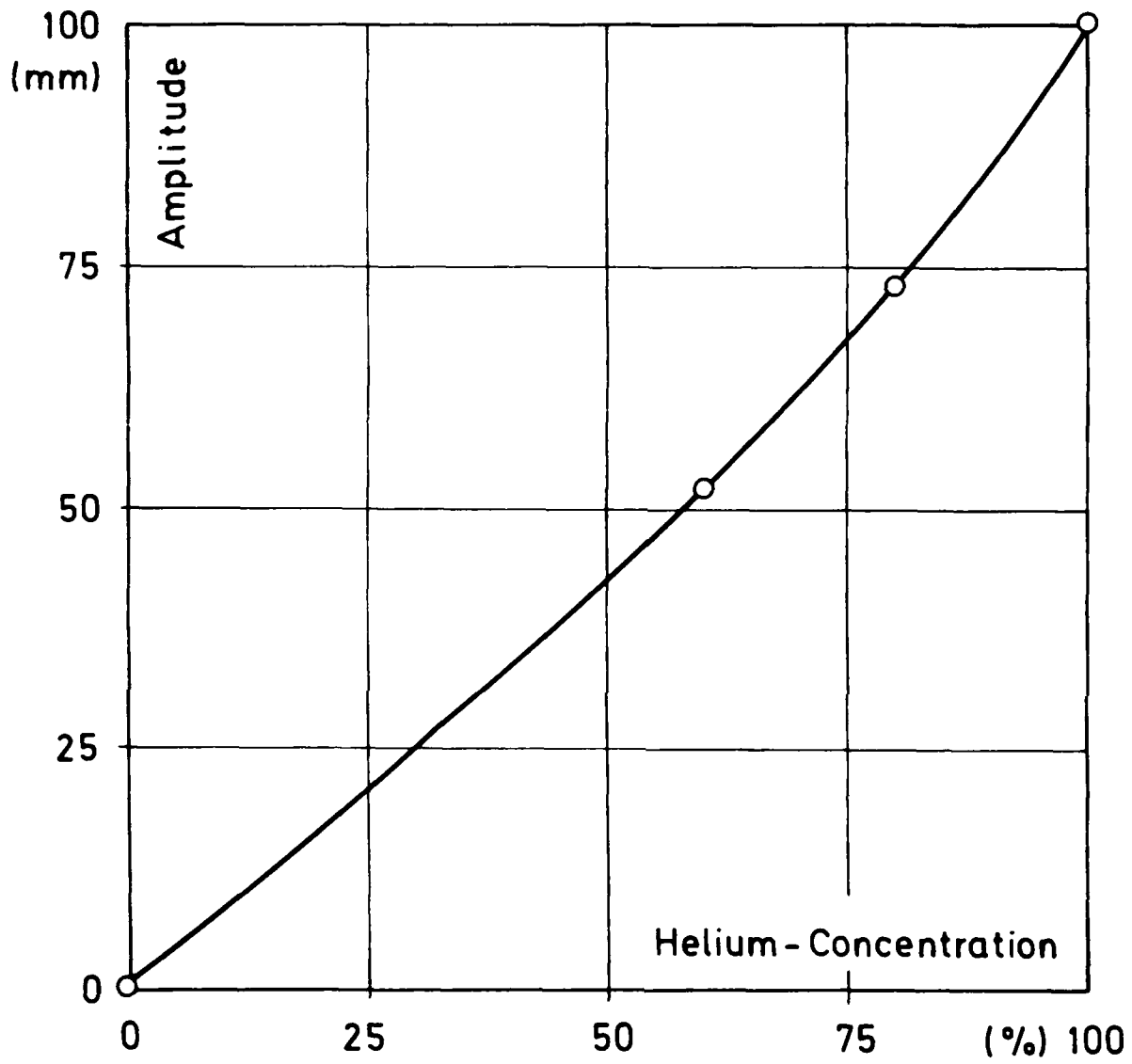


Figure 27. Calibration curve for helium-concentration measurements.

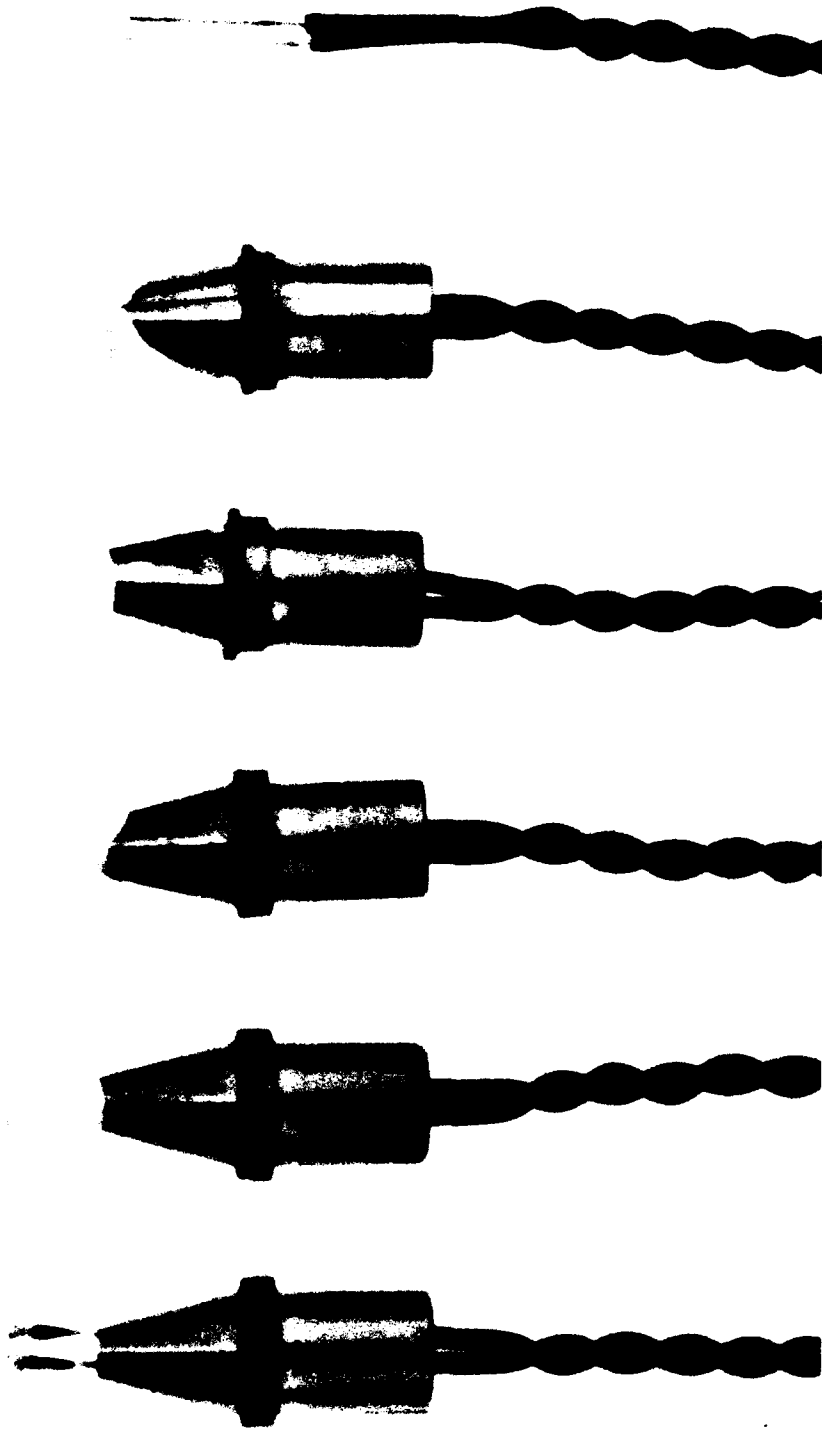


Figure 28. Intermediate stages of the manufacturing process of the HE charge.



Figure 29. Some frames of a Cordin-camera film. Test No. M 027;
HOB = 12.5 cm, smooth surface (aluminum). Charge weight = 0.6 g.
Exposure time of a frame $3 \mu\text{s}$.

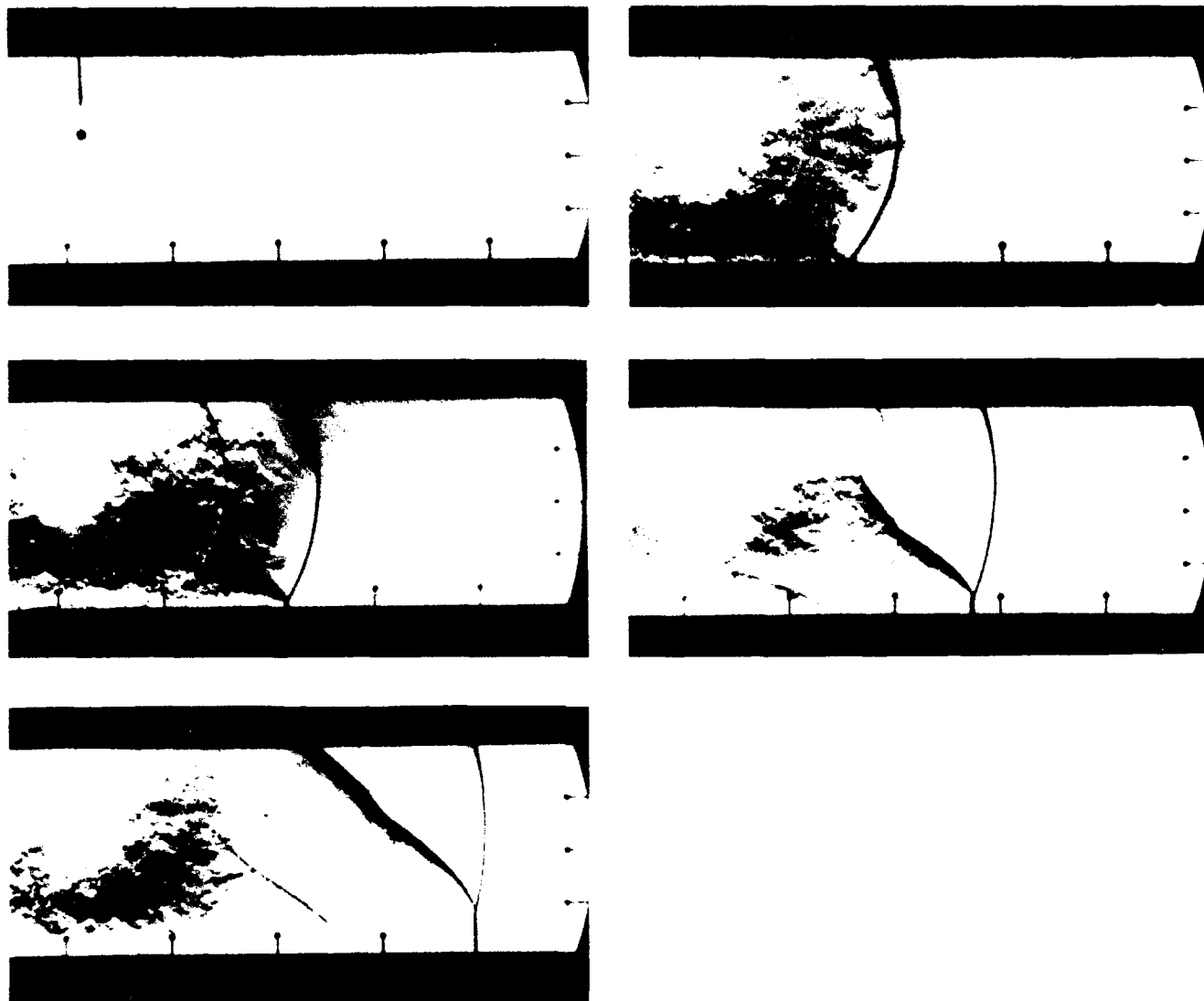


Figure 30. Single frame photographs. Tests No. M 44, M 46, M42, M 43.
RCS = 12.5 cm; smooth surface (aluminum). Charge weight = 0.6 g.
Exposure time = 0.3 μ s. First frame shows charge before detonation.

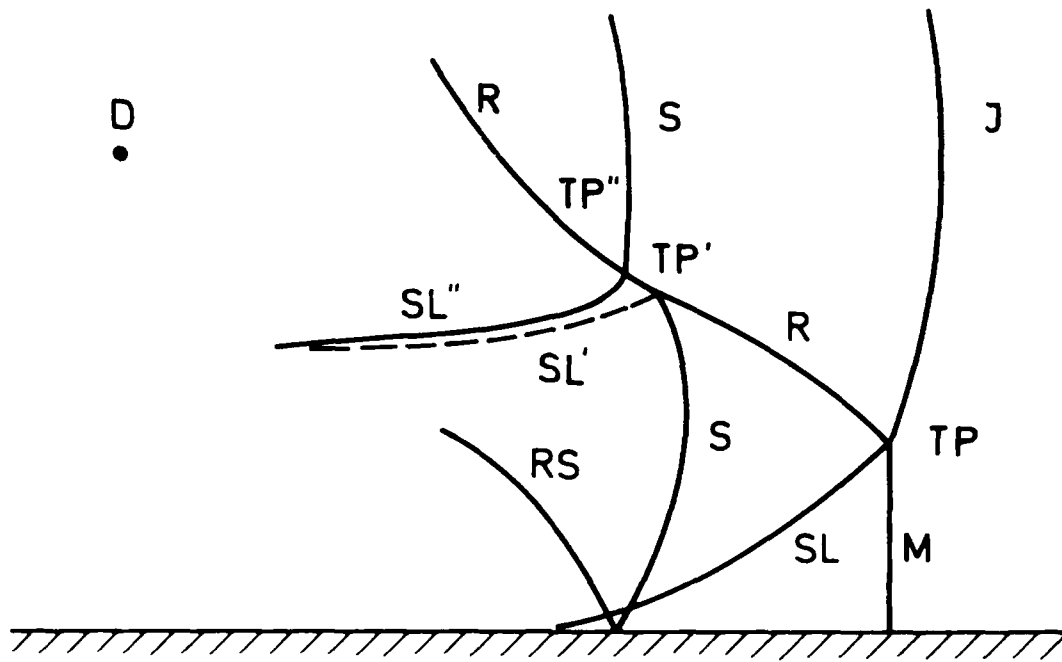


Figure 31. Explanation of the wave system in the case of non-precursed blast propagation.

- D = Detonation point
- I = Incident shock
- M = Mach-stem
- R = Reflected shock
- SL = Slip line
- S = Second shock
- RS = Reflected second shock
- TP = Triple point

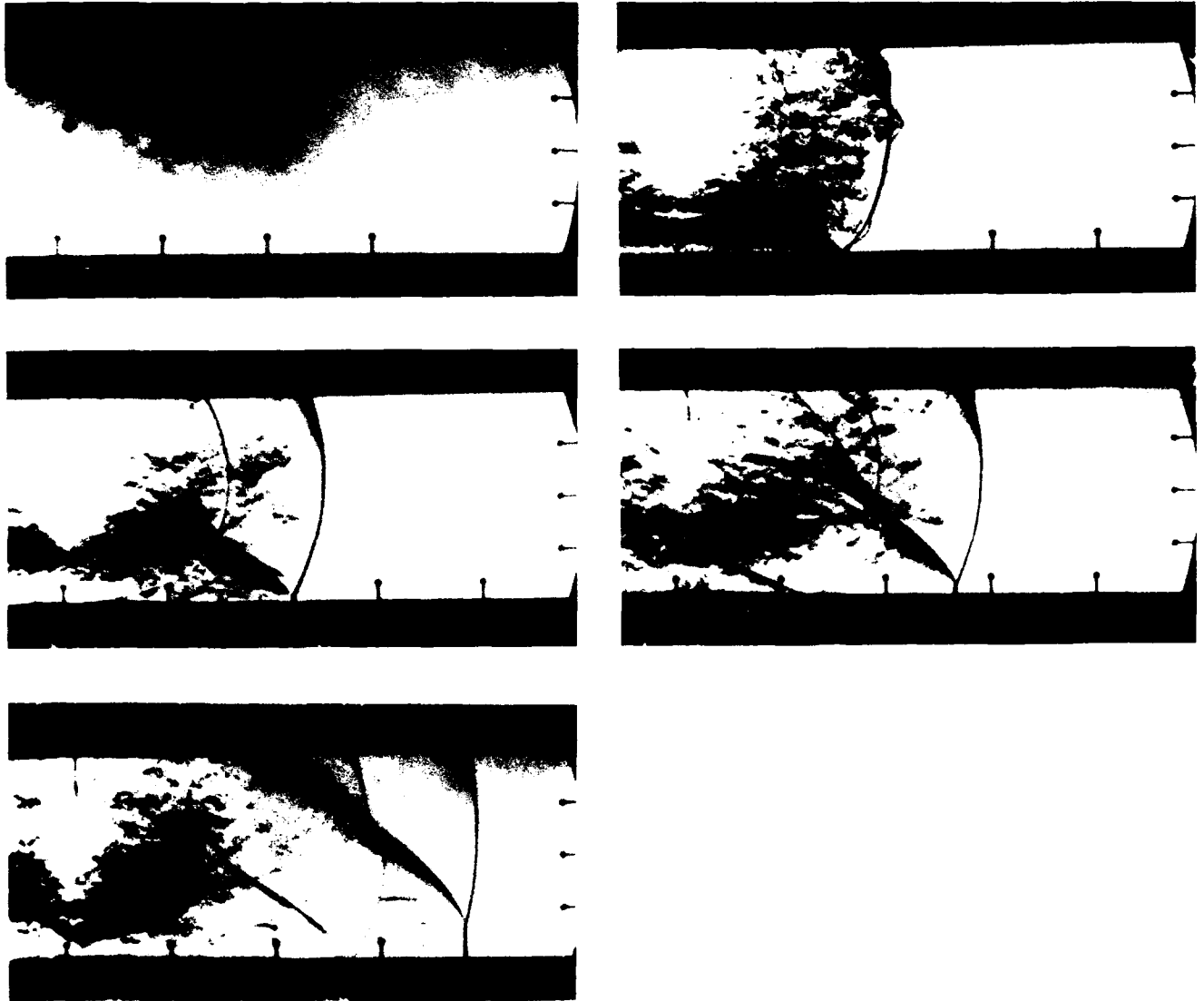


Figure 32. Single frame photographs.
Tests No. M 51; M 50; M 49; M 48; HOB = 12.5 cm;
rough surface; charge weight = 0.6 g; exposure time = 0.3 μ s.
First frame shows charge before detonation.

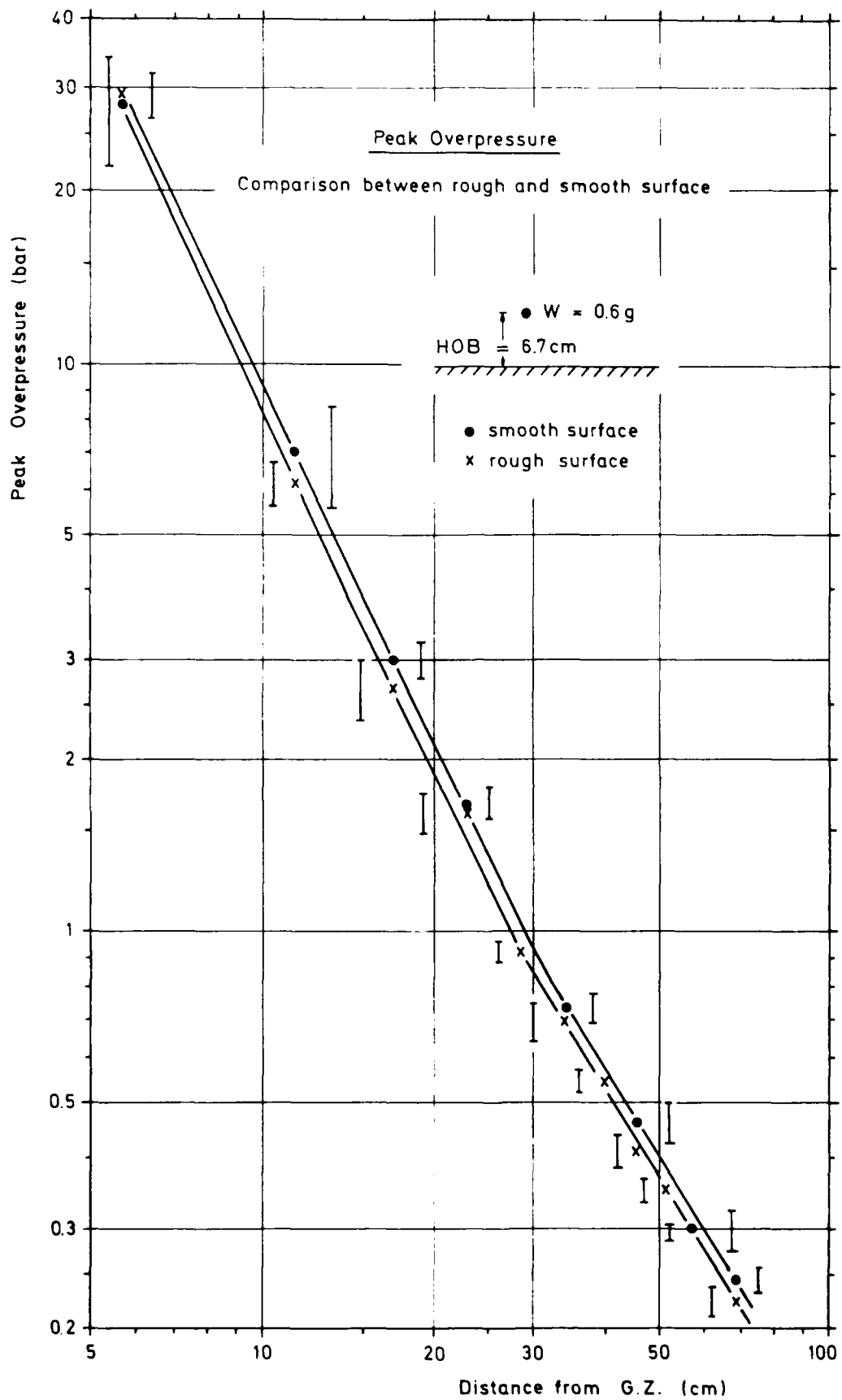


Figure 33. Peak overpressure P_{50} at smooth and rough surfaces. HOB = 6.7 cm, charge weight = 0.6 g. The error bars are marked left and right of the data points for a clearer representation.

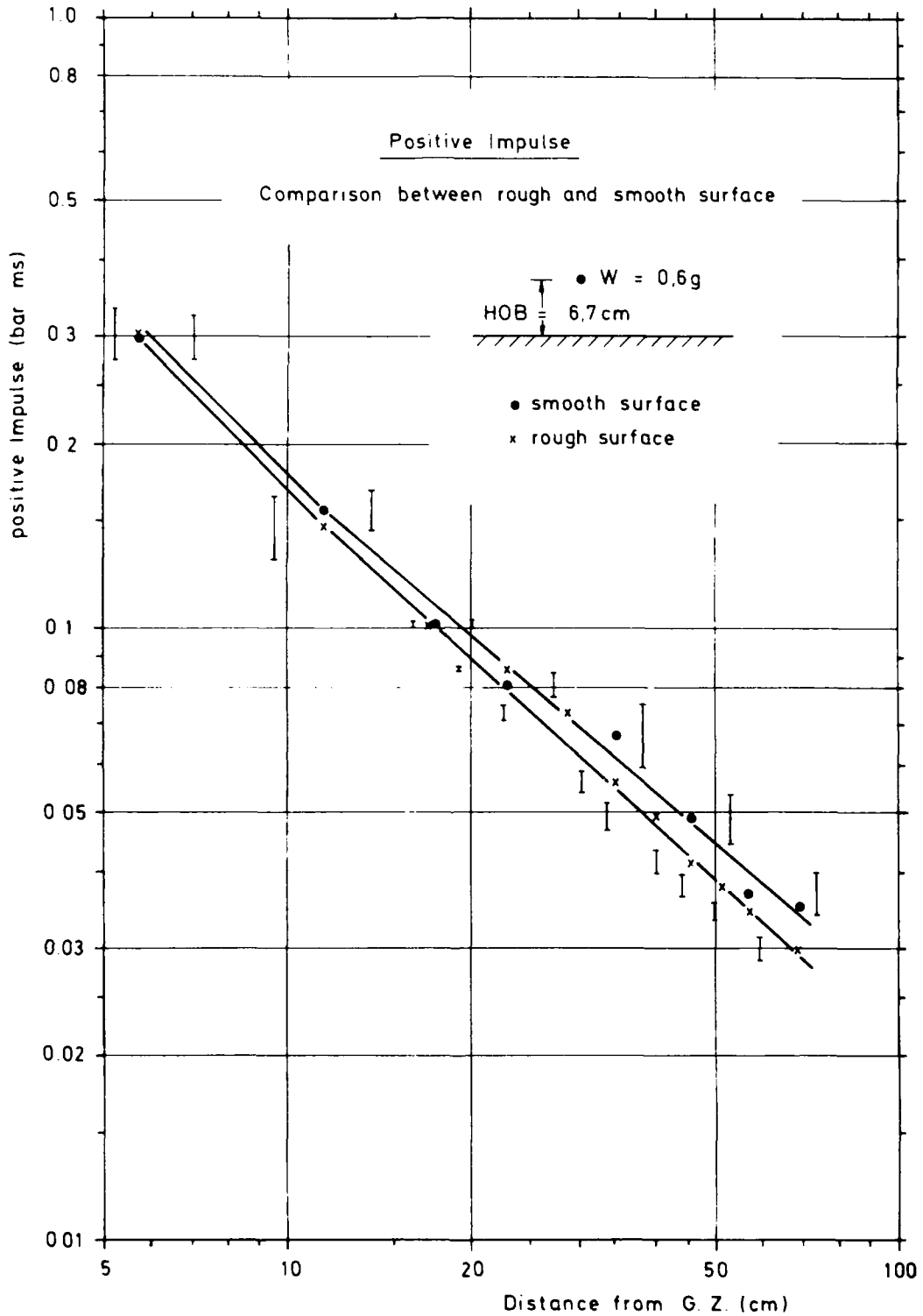
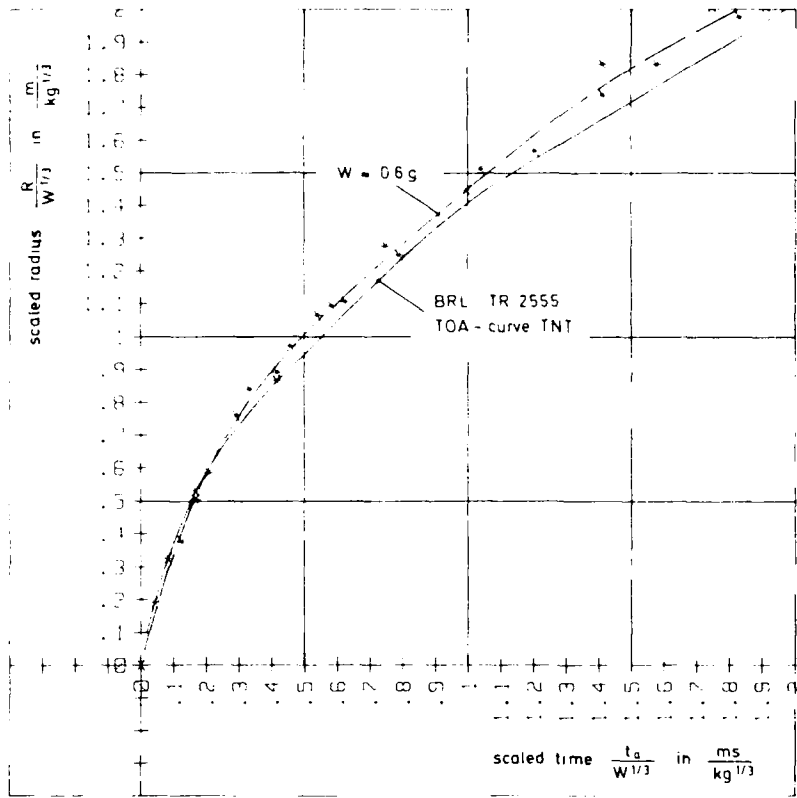
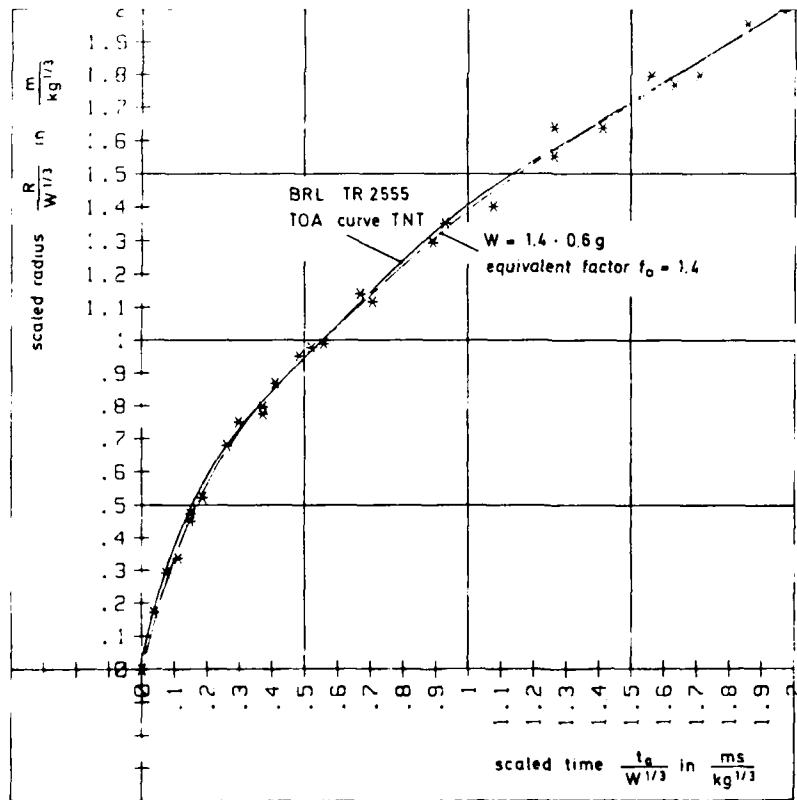


Figure 34. Overpressure impulse I_+ at smooth and rough surfaces. HOB = 6.7 cm, charge weight = 0.6 g. The error bars are marked left and right of the data points for a clearer representation.



(Fig. 35a)



(Fig. 35b)

Figure 35. Comparison between measured radius-time values of the shock front from Cordin camera pictures with time-of-arrival TNT free field data. Upper diagram is before matching, lower diagram is after matching. TNT equivalent factor: $f_0 = 1.4$.

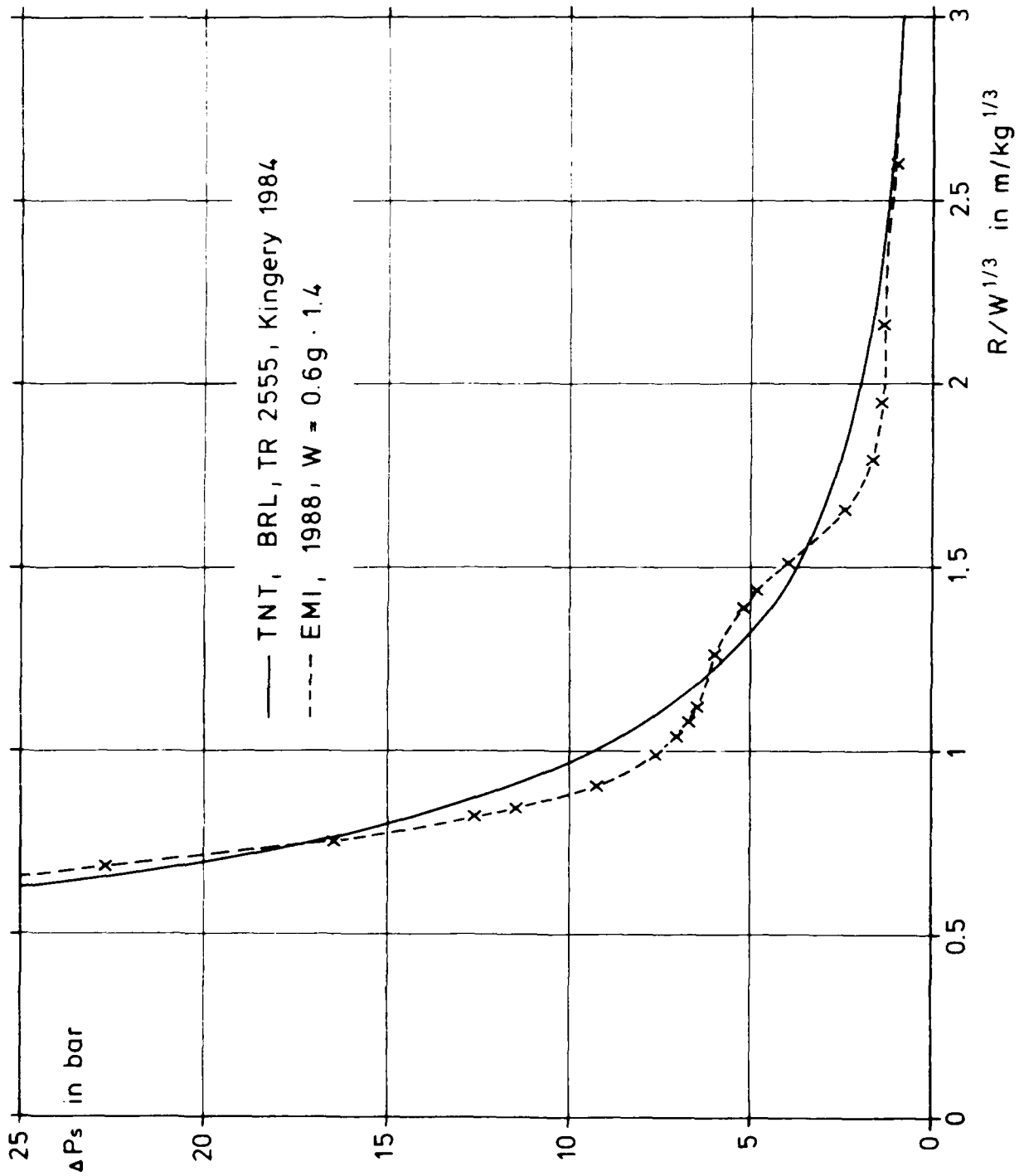
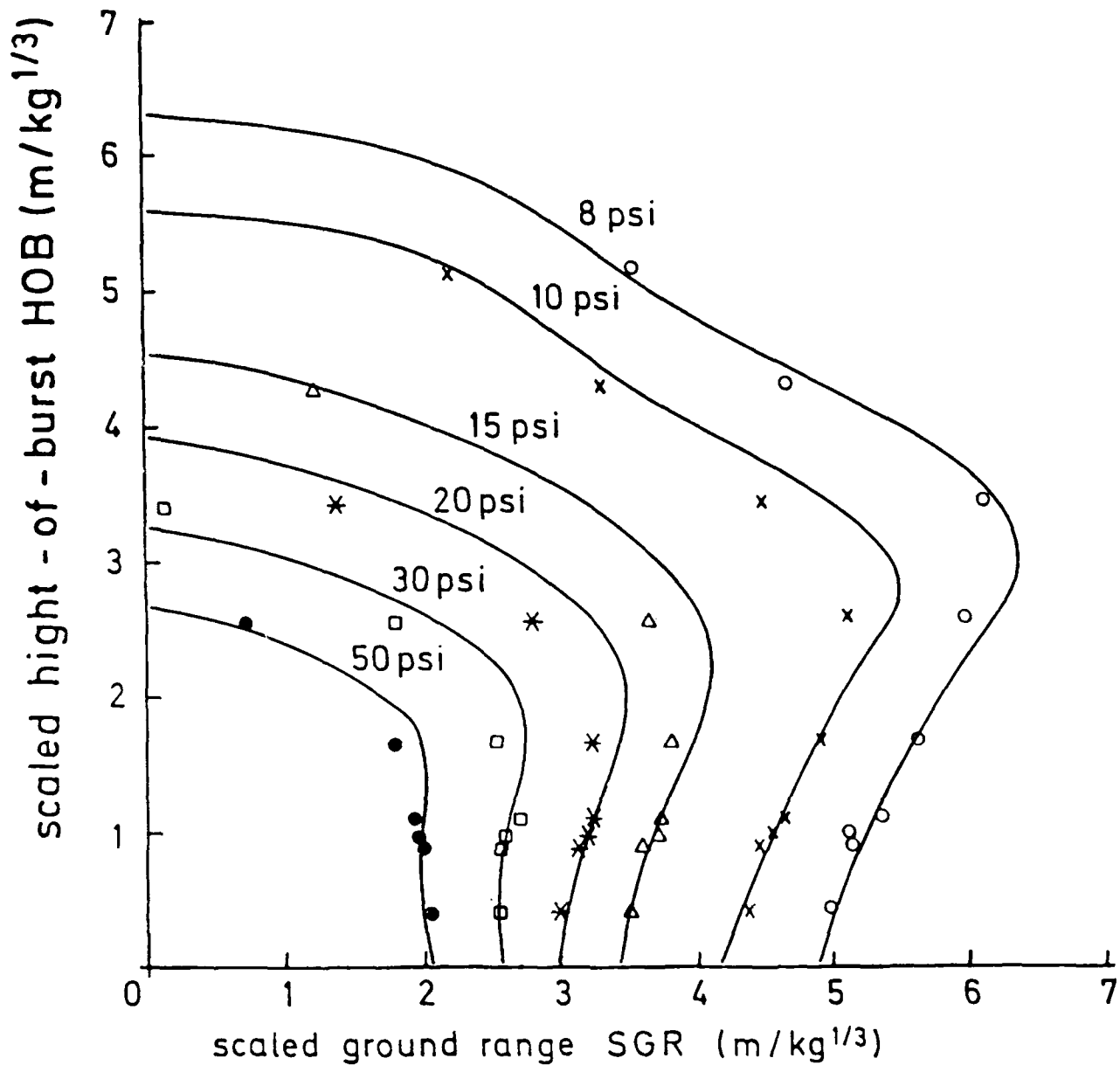


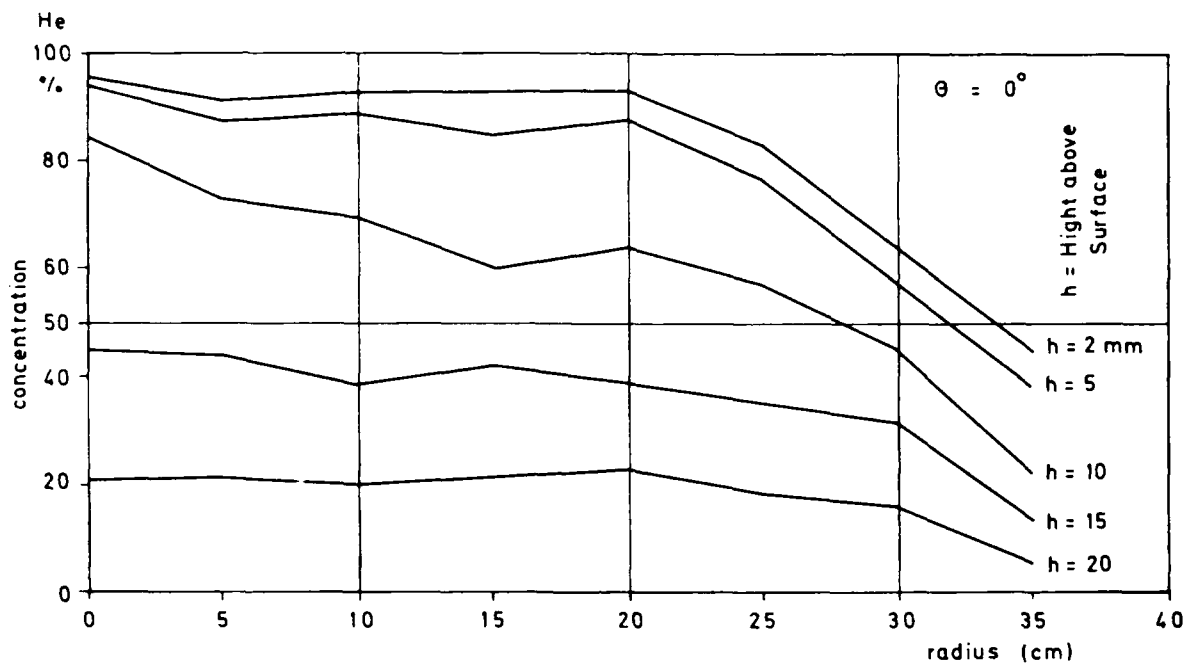
Figure 36. Comparison between evaluated peak overpressure-distance value from Cordin camera pictures with peak overpressure free field data for TNT. TNT equivalent factor $f_0 = 1.4$.



HE HOB - Curves, $W = 1$ kg RDX, EMI 1984
 Data points fitted by 8. degree power functions

Figure 37. Comparison with RDX-HOB curves. In this case, the best fit is achieved with an RDX equivalent factor of $f_0 = 0.7$.

Helium Concentration in Horizontal Direction



Helium Concentration in Vertical Direction

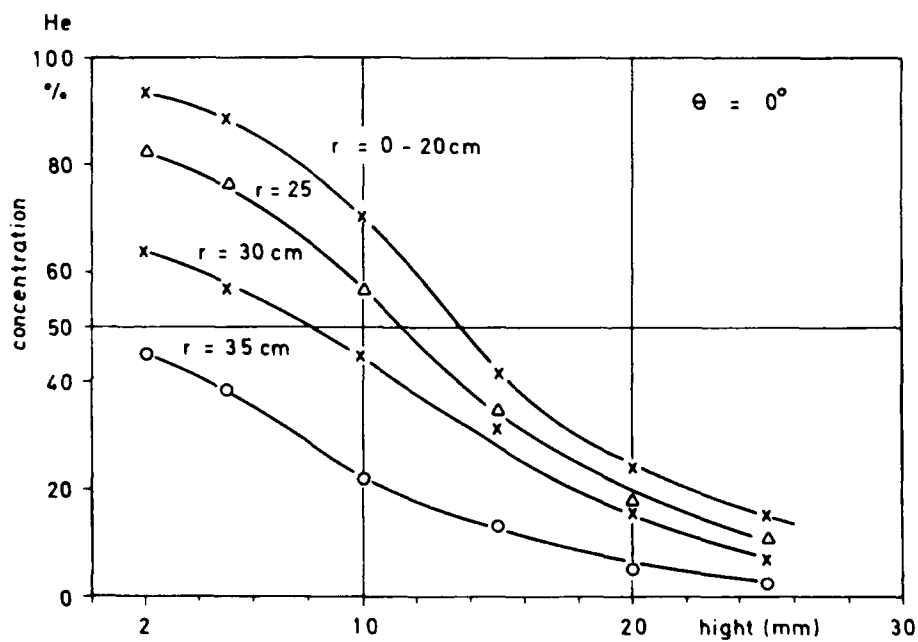


Figure 38. Measured helium concentration as function of radius and height. High helium concentrations of more than 90% were achieved.

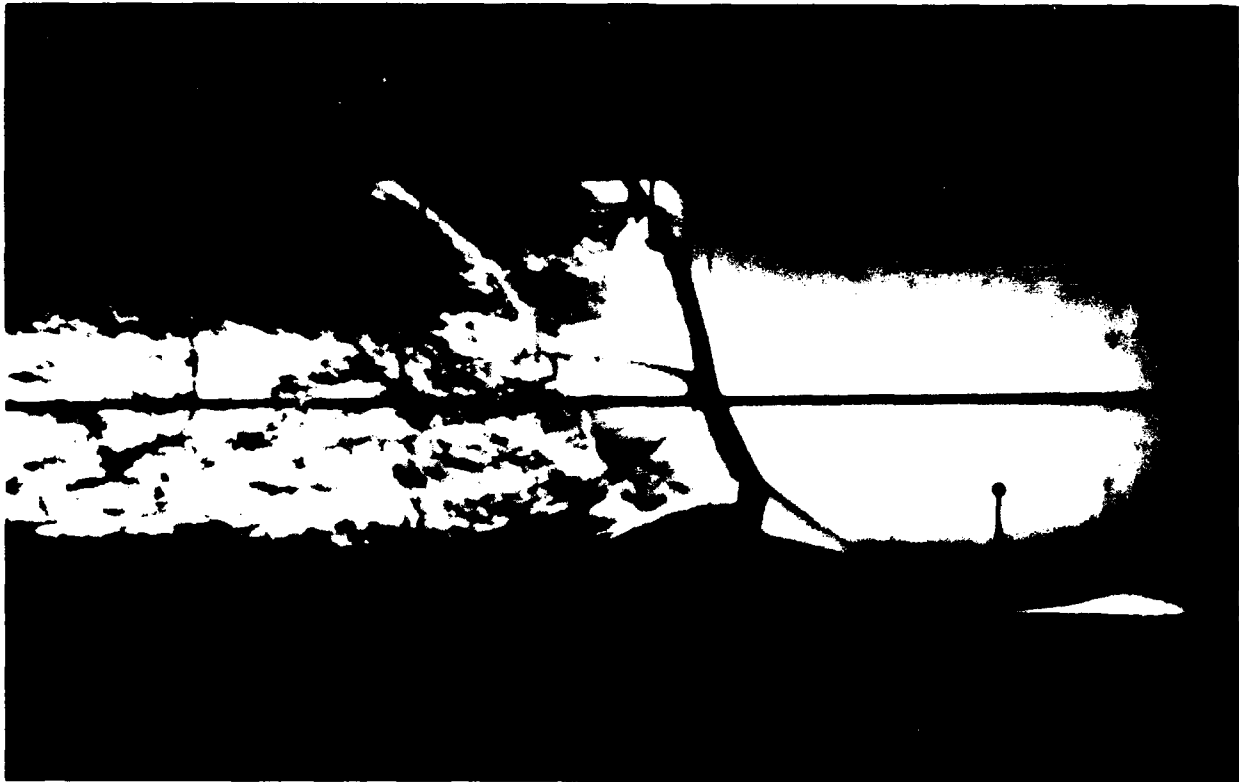
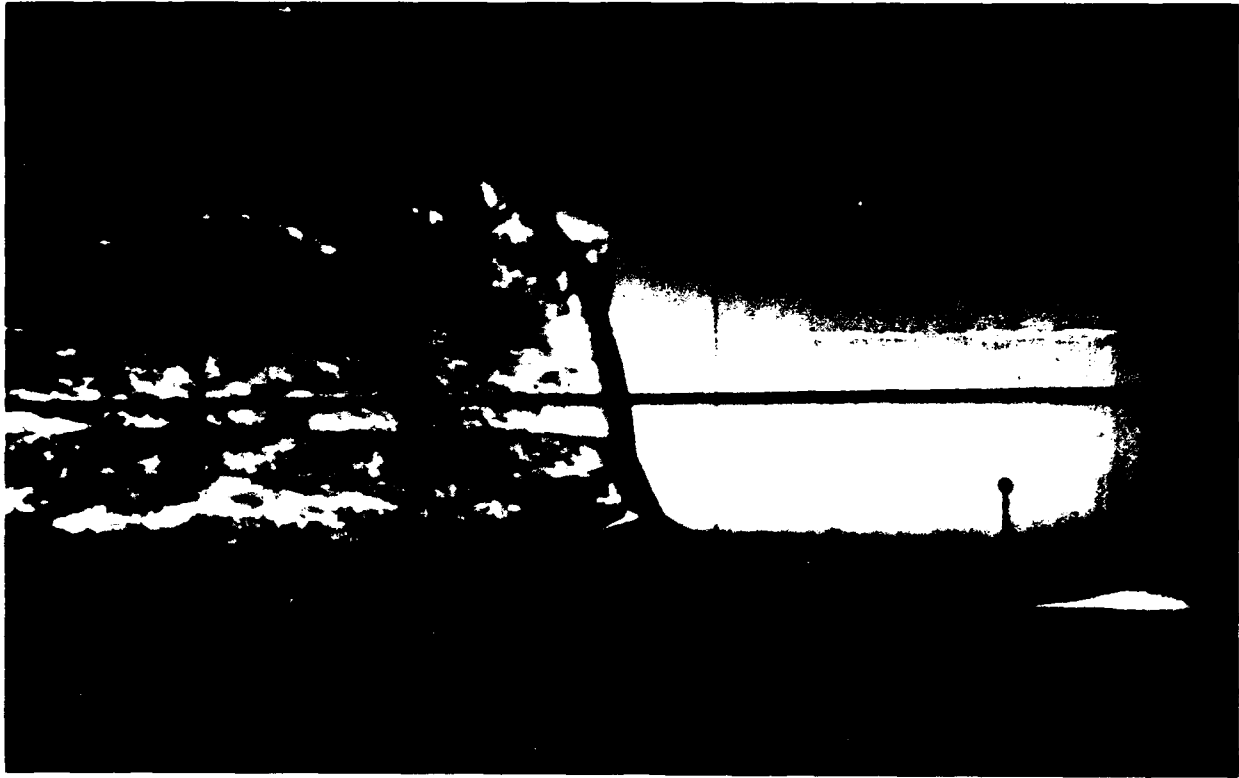


Figure 39. Two frames of a Cordin cinematographic picture series. Test No. M 228. Frames 59 and 84. HOB = 6.7 cm.

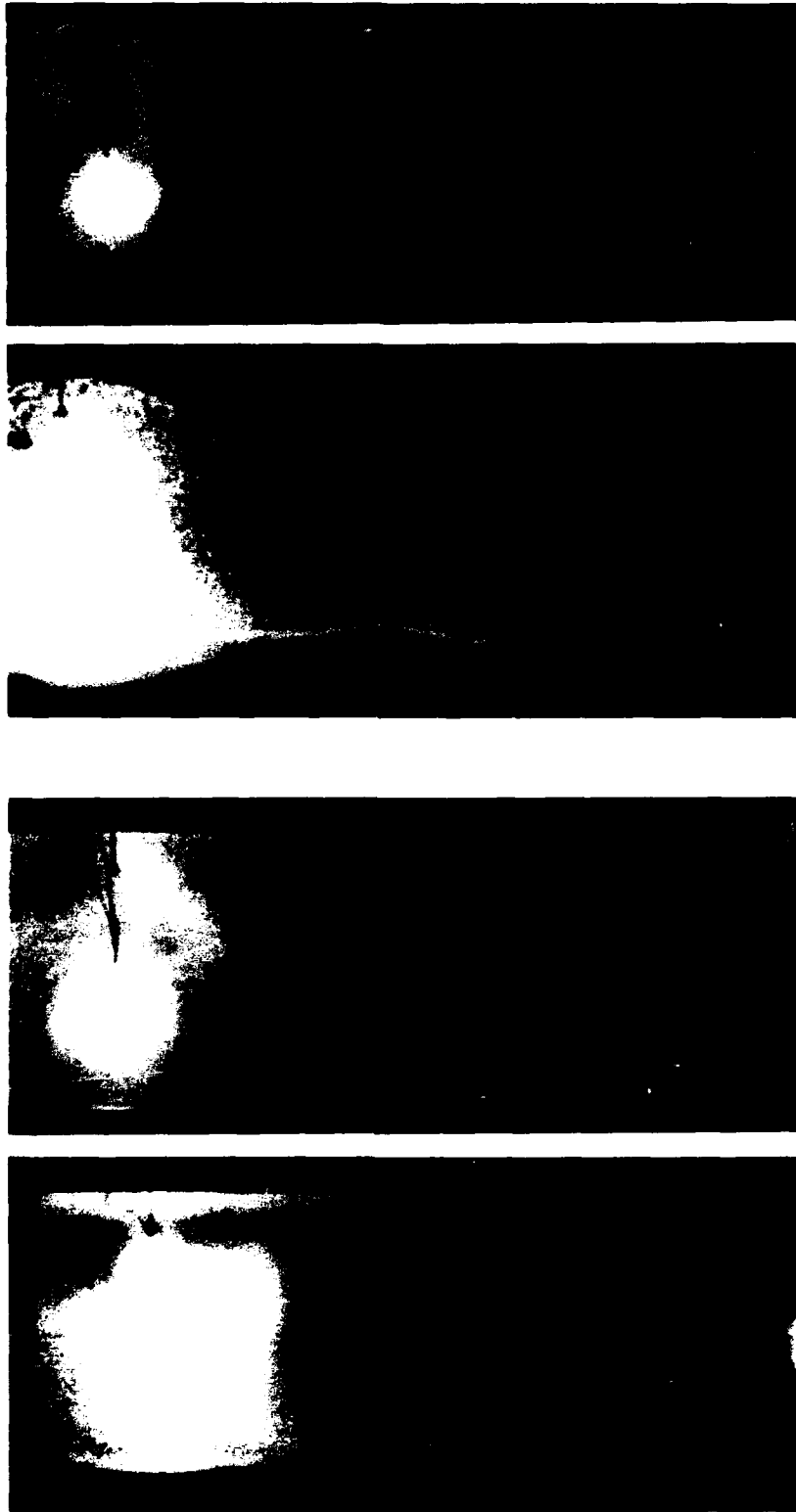


Figure 40. Precursed and ideal HOB-shock structure. HOB = 6.7 cm.
a) 180 μ s after charge ignition (tests M 263 and M 198)
b) 220 μ s after charge ignition (tests M 264 and M 190)

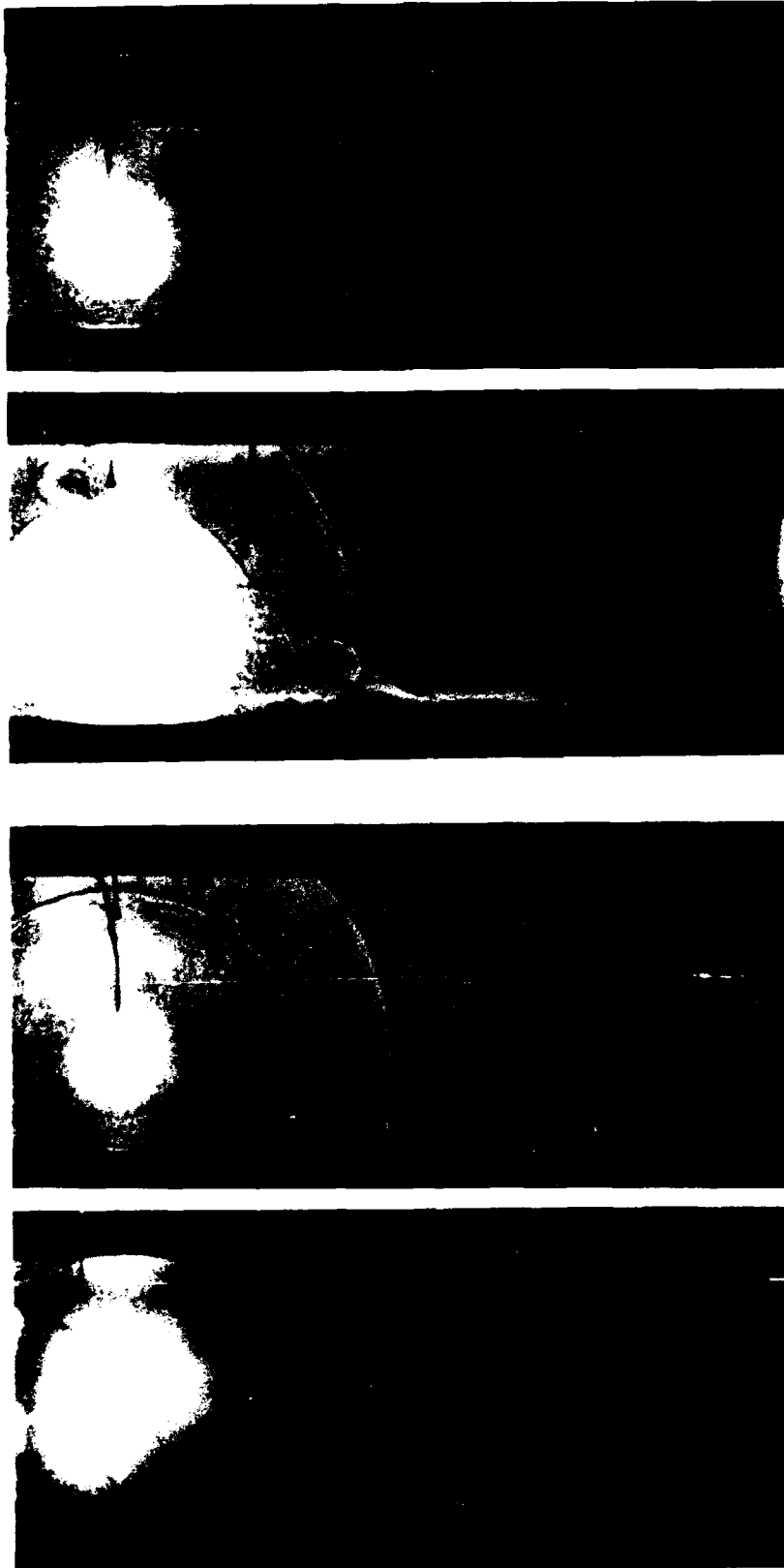


Figure 40. c) 250 μ s after charge ignition (tests M 260 and M 183)

d) 350 μ s after charge ignition (tests M 262 and M 201)

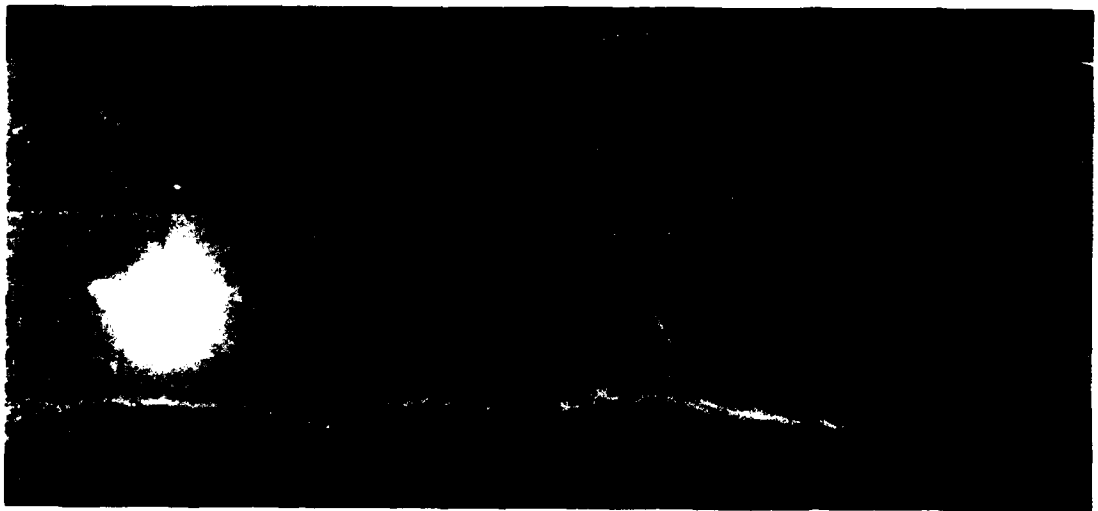
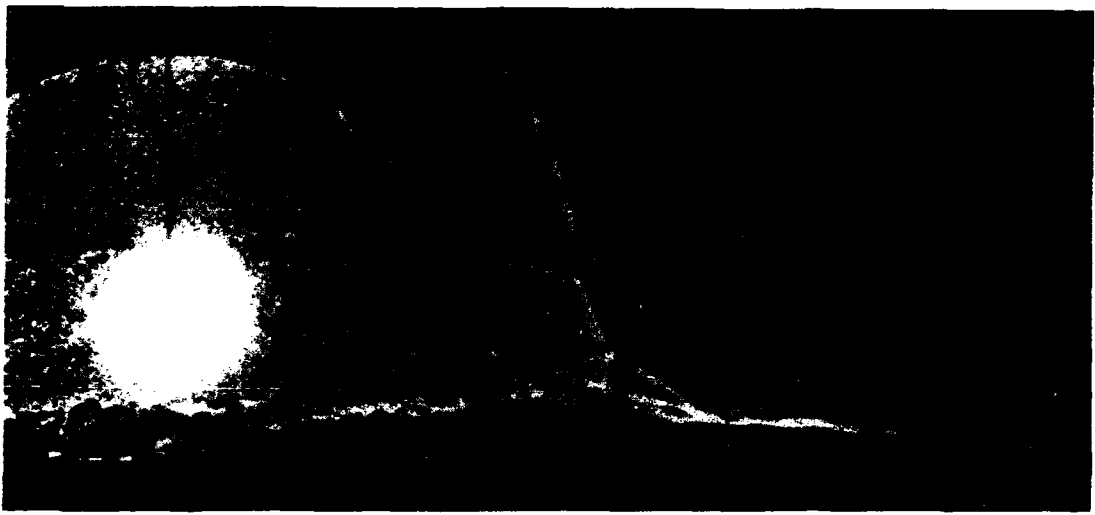
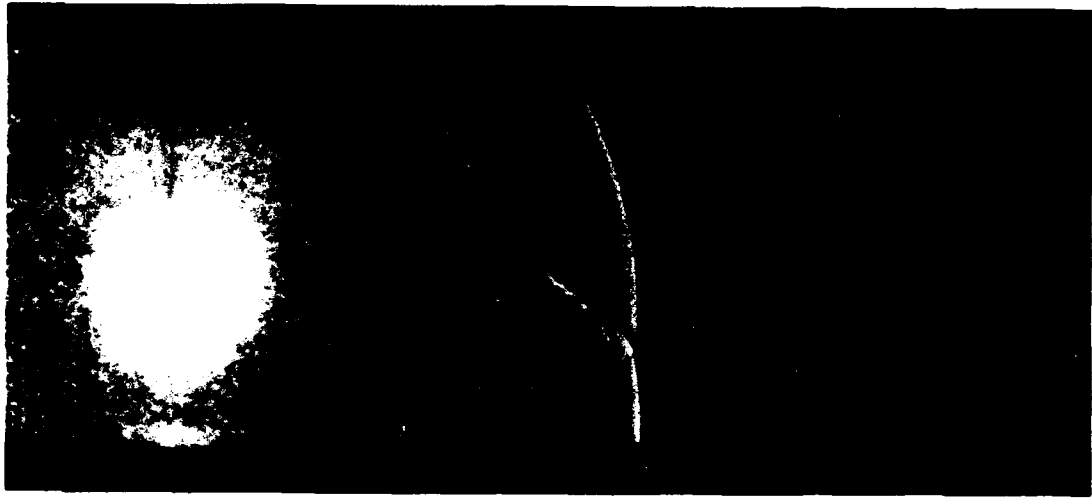
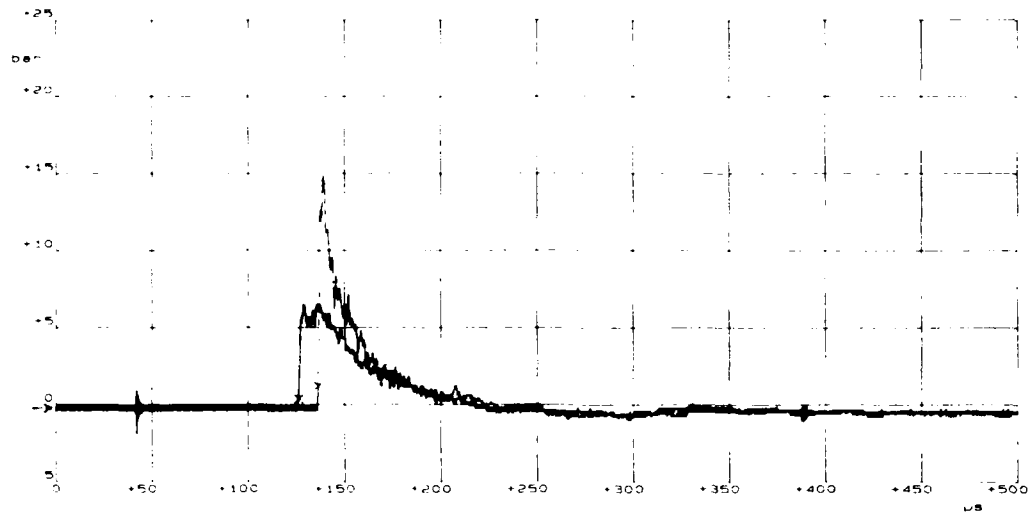
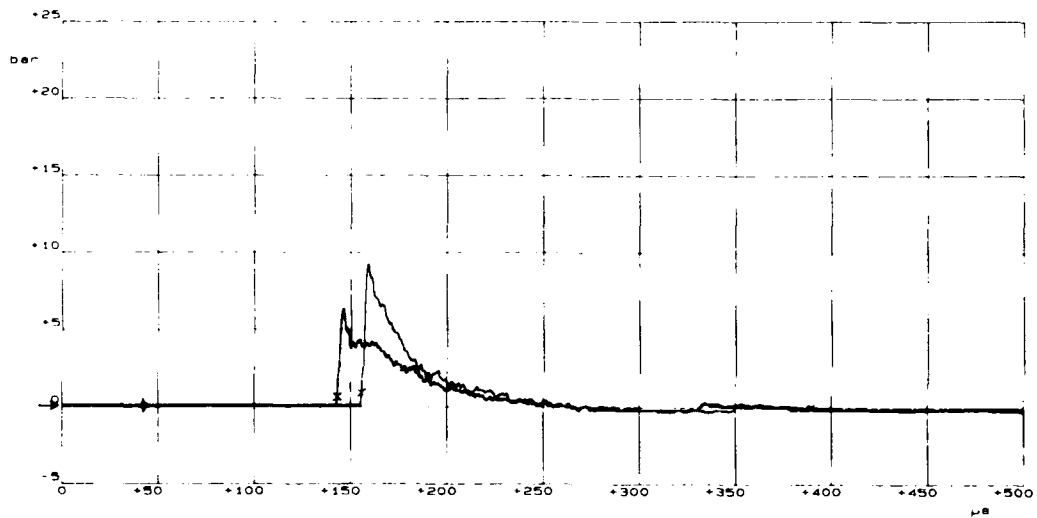


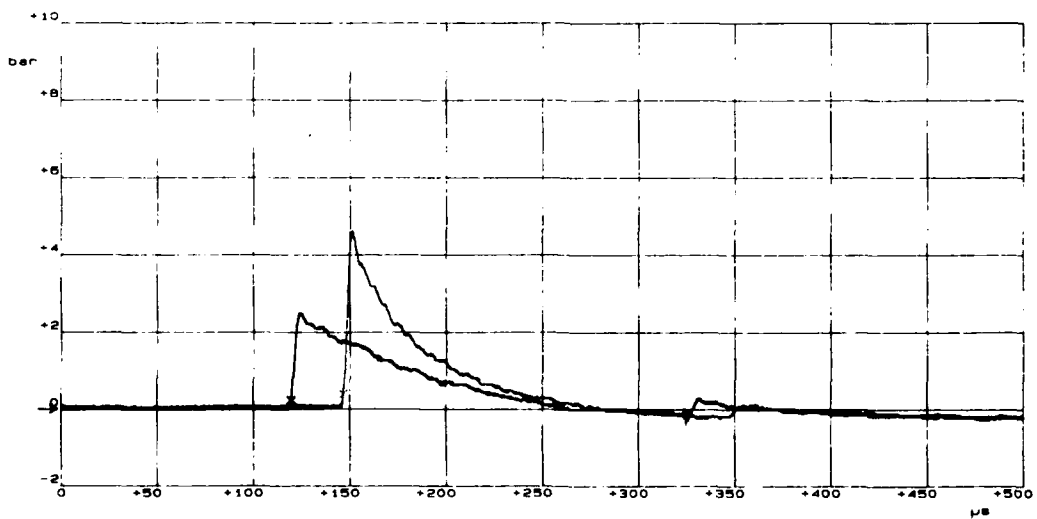
Figure 41. Deformation of the edges of a cube by light deflection in an inhomogeneous density field (tests M 240, M 236, M 237).



Mk1 5bar pro V am 5001

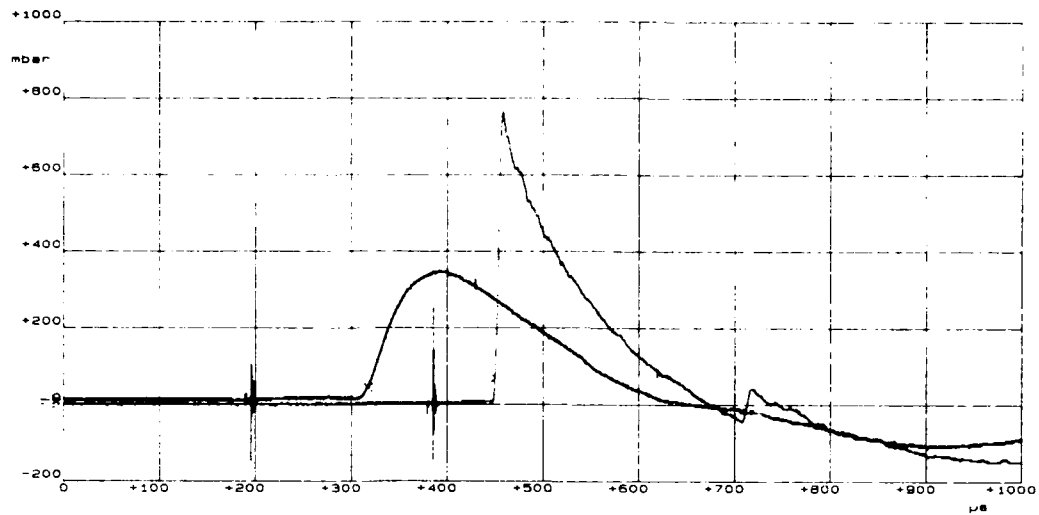


Mk2 2bar pro V am5001

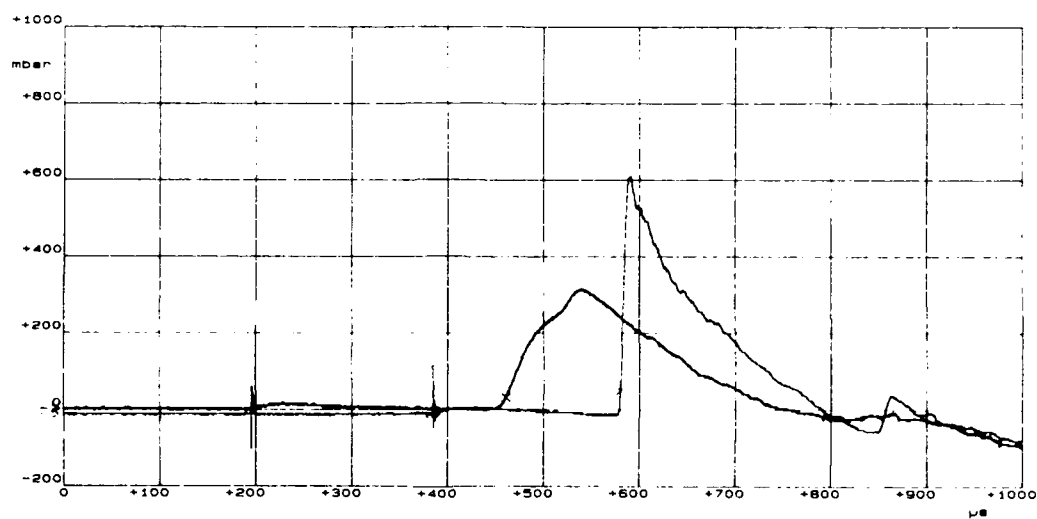


Mk3 2bar pro V am 5001

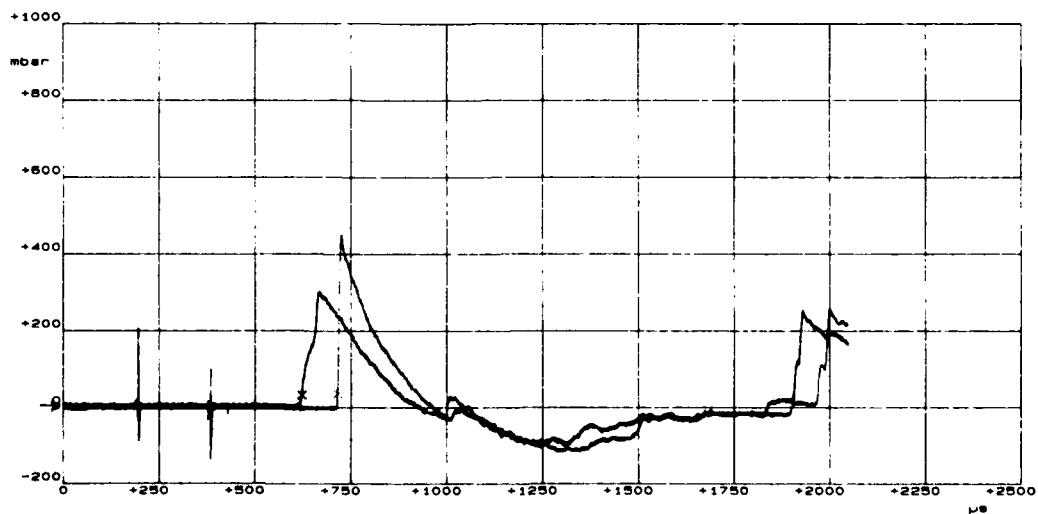
Figure 42. Pressure records at different ground range positions for nonprecursed (black) and precursed (grey) blast (for positions see Fig. 18; tests M 245 and M 248, resp.).



Mk 7 1bar pro V am 5001

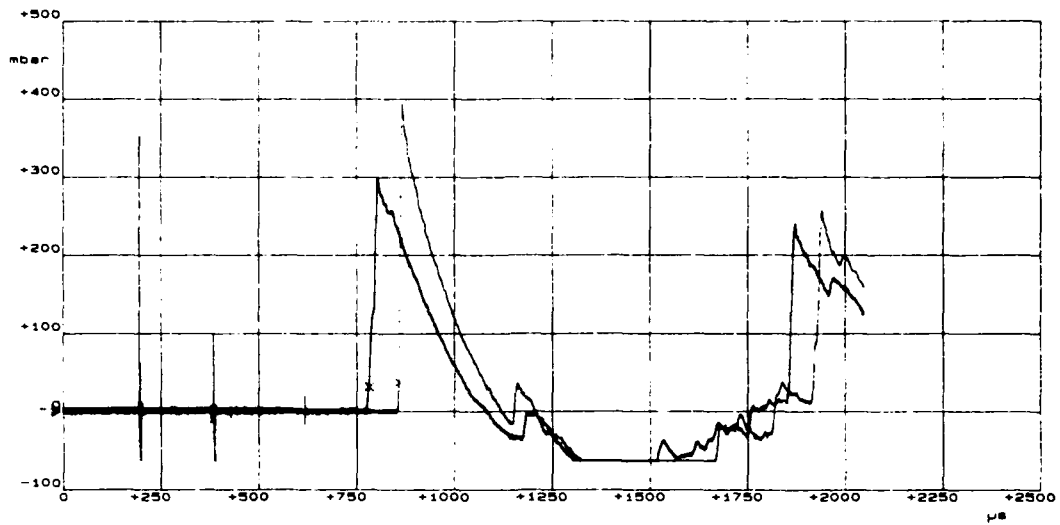


Mk 8 1bar pro V am 5001

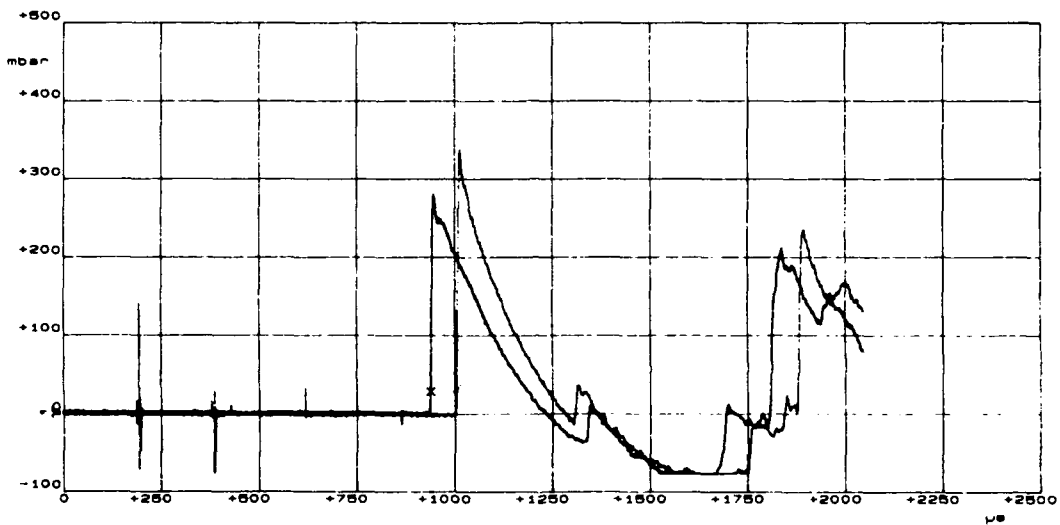


Mk 9 1bar p V am 5007

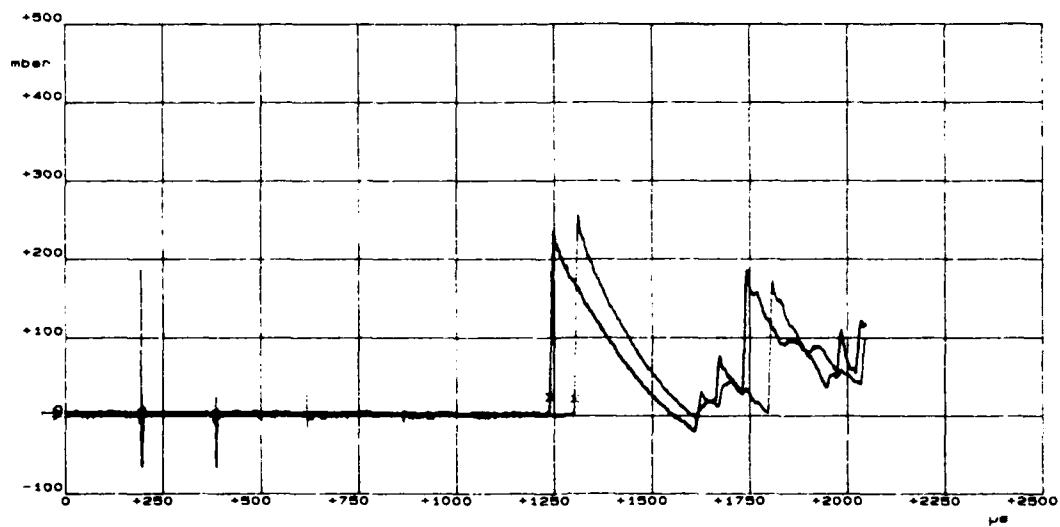
Figure 42. Pressure records at different ground range positions for nonprecursed (black) and precursed (grey) blast (for positions see Fig. 18; tests M 245 and M 248, resp.) (continued).



Mk10 1bar p V am 5007

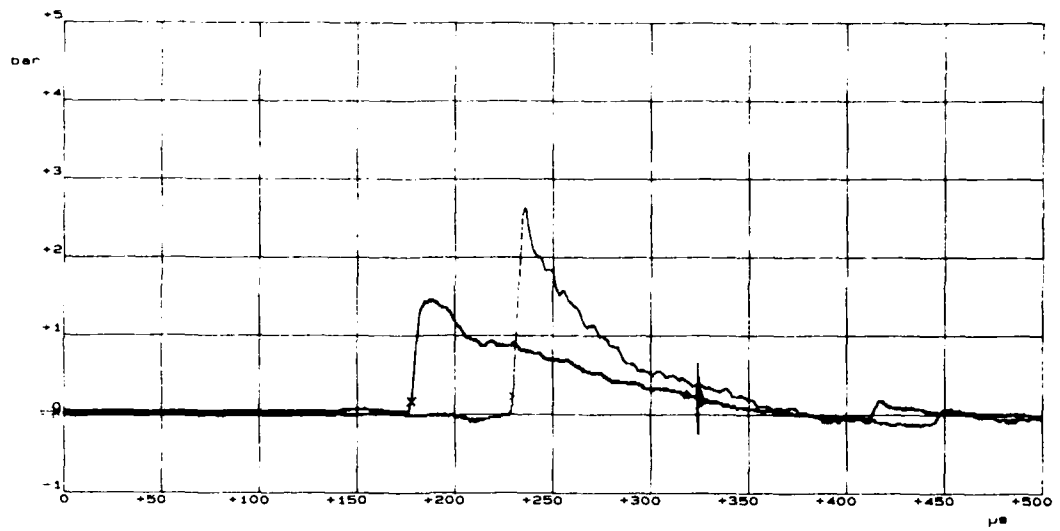


Mk11 1bar p V am 5007

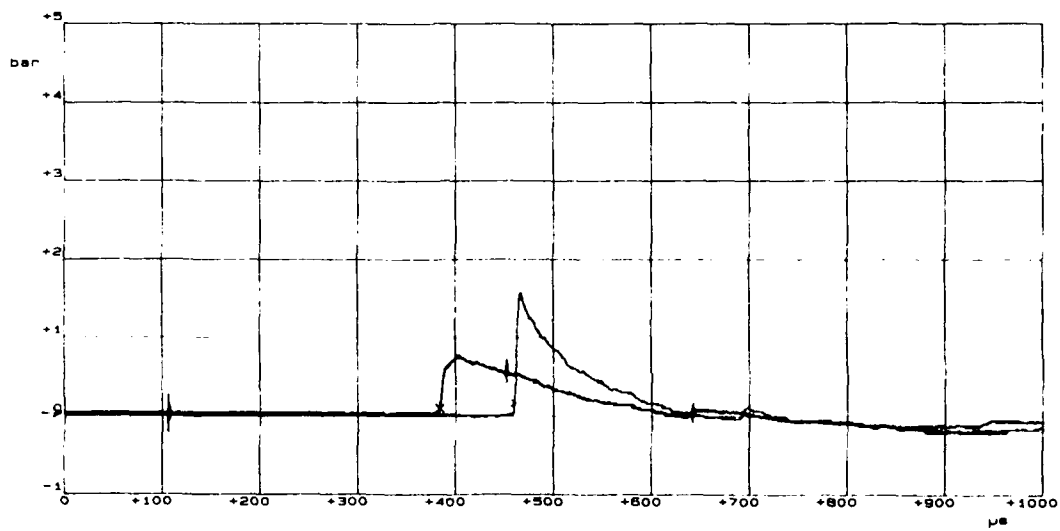


Mk12 1bar pIV am 5007

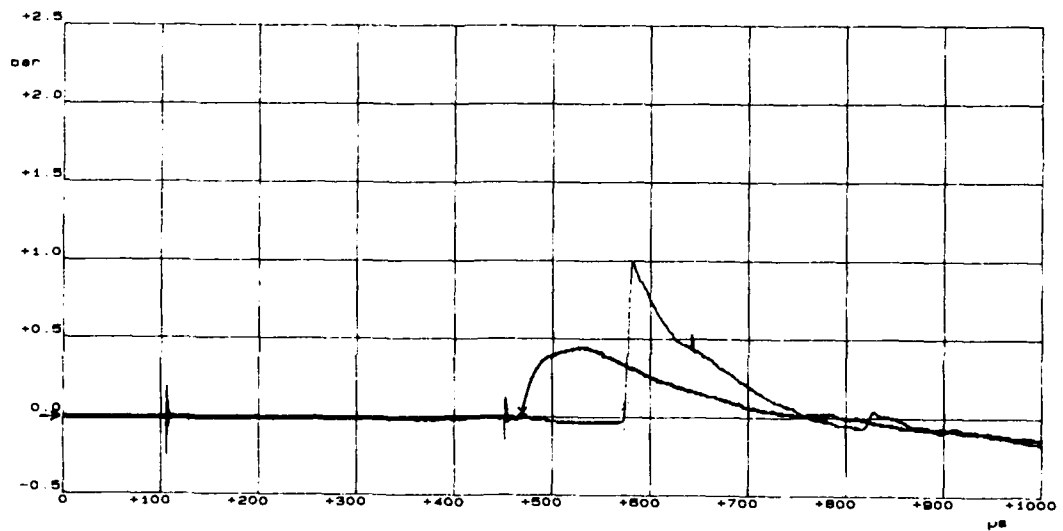
Figure 42. Pressure records at different ground range positions for nonprecursed (black) and precursed (grey) blast (for positions see Fig. 18; tests M 245 and M 248, resp.) (continued).



Mk4 2bar pro V am 5001

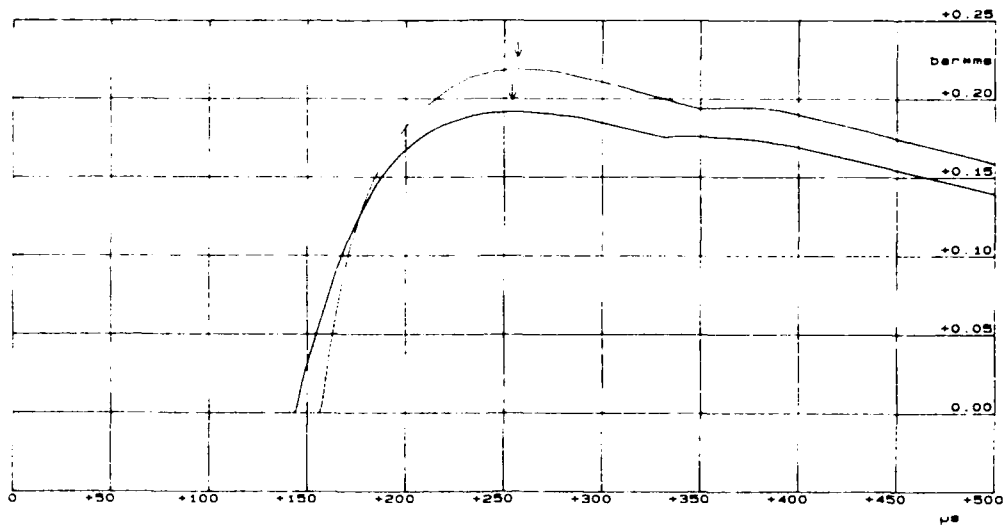


Mk5 1bar pro V am 5001

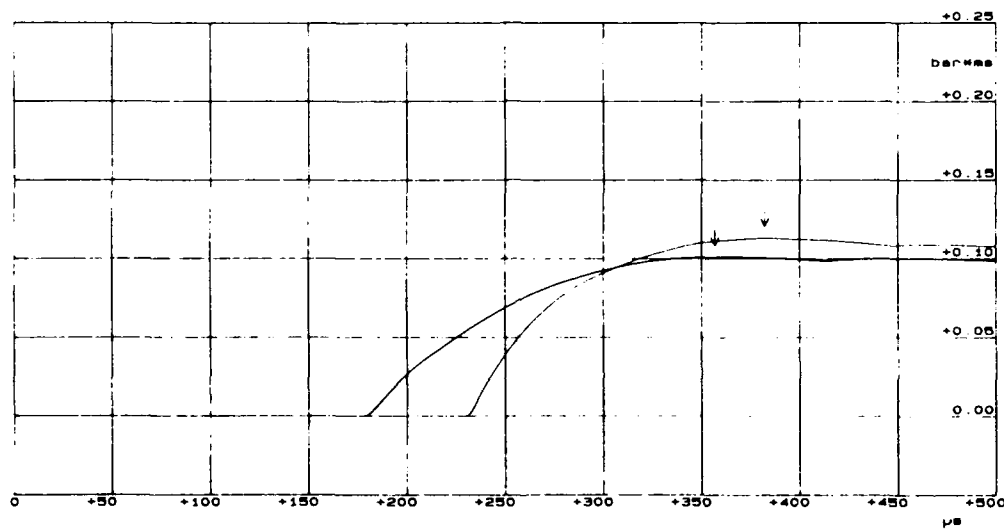


Mk6 1bar pro V am 5001

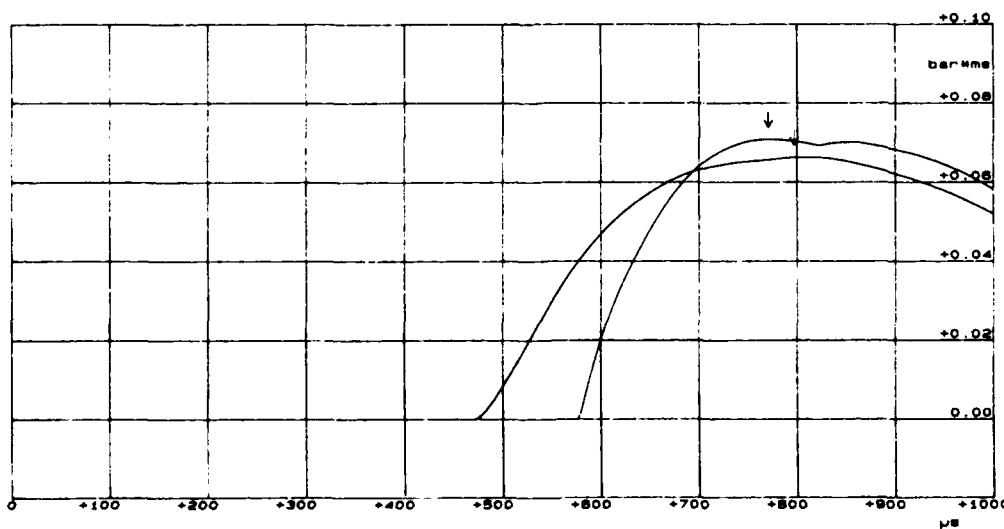
Figure 42. Pressure records at different ground range positions for nonprecursed (black) and precursed (grey) blast (for positions see Fig. 18; tests M 245 and M 248, resp.) (continued).



Mk2 2bar pro V am5001

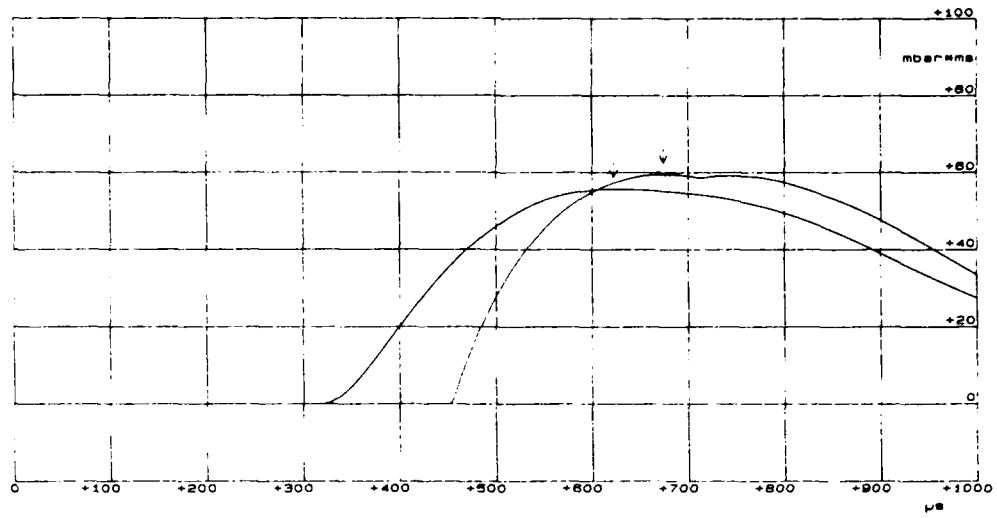


Mk4 2bar pro V am 5001

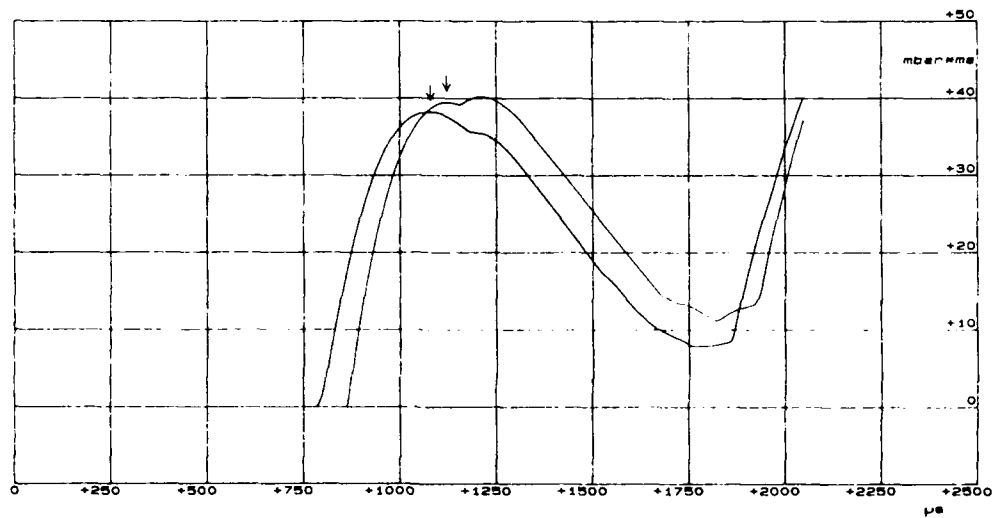


Mk6 1bar pro V am 5001

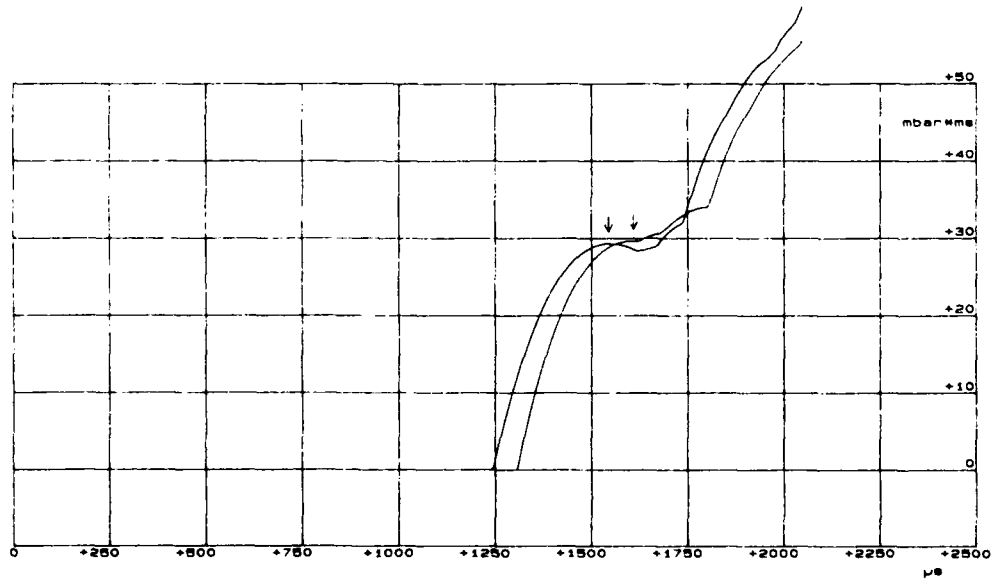
Figure 43. Impulse curves at different ground range positions for nonprecursed (black) and precursed (grey) blast (tests M 245 and M 248, resp.).



Mk7 1bar pro V am 5001



Mk10 1bar p V am 5007



Mk12 1bar p1V am 5007

Figure 43. Impulse curves at different ground range positions for nonprecursed (black) and precursed (grey) blast (tests M 245 and M 248, resp.) (continued).

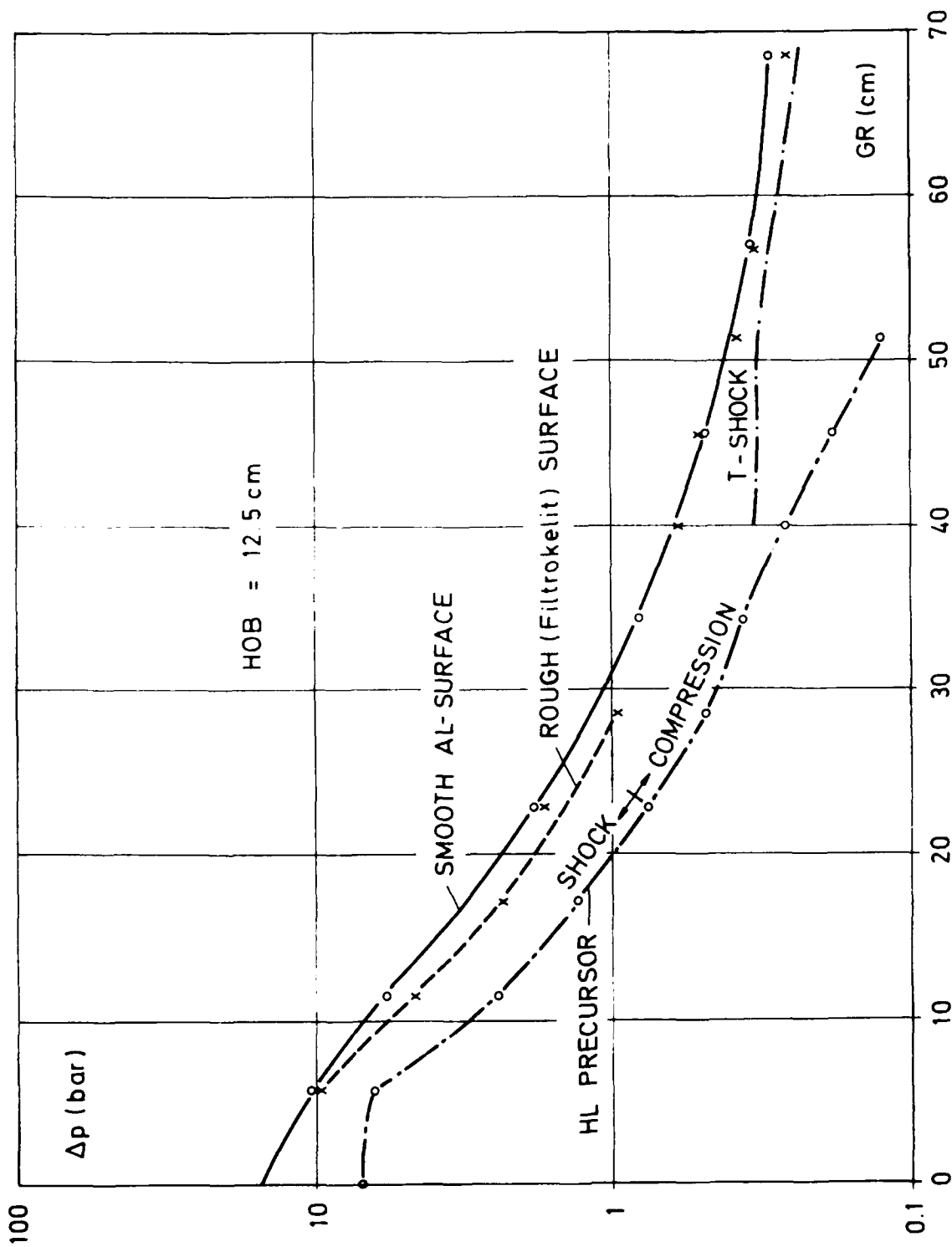


Figure 44. Peak overpressure versus ground range for nonprecursed blast at smooth and rough surfaces, respectively, and for precursed blast. HOB = 12.5 cm (375 ft/kt^{1/3}).

DISTRIBUTION LIST

DNA-TR-85-352-V3

DEPARTMENT OF DEFENSE

ASSISTANT TO THE SECRETARY OF DEFENSE
ATOMIC ENERGY

ATTN: EXECUTIVE ASSISTANT

DEFENSE INTELLIGENCE AGENCY

ATTN: DB-6E

ATTN: RTS-2B

ATTN: VP-TPO

DEFENSE NUCLEAR AGENCY

2 CYS ATTN: SPSD

ATTN: SPSP

ATTN: SPWE K PETERSEN

ATTN: SPWE/RINEHART

4 CYS ATTN: TITL

DEFENSE NUCLEAR AGENCY

ATTN: TDNV

DEFENSE NUCLEAR AGENCY

ATTN: TDNM-CF

ATTN: TDTT W SUMMA

DEFENSE TECHNICAL INFORMATION CENTER

2 CYS ATTN: DTIC/FDAB

DEPARTMENT OF DEFENSE EXPLO SAFETY BOARD

ATTN: CHAIRMAN

JOINT STRAT TGT PLANNING STAFF

ATTN: JK

ATTN: JKAD

ATTN: JKCS

ATTN: JPEP

ATTN: JPTM

UNDER SECRETARY OF DEFENSE

ATTN: G SEVIN

DEPARTMENT OF THE ARMY

DEP CH OF STAFF FOR OPS & PLANS

ATTN: DAMO-NCN

HARRY DIAMOND LABORATORIES

ATTN: SLCIS-IM-TL

U S ARMY ARM, MUNITIONS, AND CHEM COMMAND

ATTN: MA LIBRARY

U S ARMY BALLISTIC RESEARCH LAB

2 CYS ATTN: SLCBR-SS-T

U S ARMY CORPS OF ENGINEERS

ATTN: DAEN-RDL

U S ARMY ENGINEER DIV HUNTSVILLE

ATTN: HNDED-SY

U S ARMY ENGINEER DIV OHIO RIVER

ATTN: ORDAS-L

U S ARMY ENGR WATERWAYS EXPER STATION

ATTN: J JACKSON

ATTN: J ZELASKO

ATTN: TECHNICAL LIBRARY

ATTN: J K INGRAM

U S ARMY FOREIGN SCIENCE & TECH CTR

ATTN: DRXST-SD

U S ARMY MATERIAL TECHNOLOGY LABORATORY

ATTN: J MESCALL

ATTN: TECHNICAL LIBRARY

U S ARMY MISSILE COMMAND/AMSMI-RD-CS-R

ATTN: AMSMI-RD-CS-R

U S ARMY NUCLEAR & CHEMICAL AGENCY

ATTN: MONA-NU

U S ARMY STRATEGIC DEFENSE CMD

ATTN: R BRADSHAW

ATTN: R K DUDNEY

U S ARMY STRATEGIC DEFENSE COMMAND

ATTN: CSSD-H-L

ATTN: CSSD-H-SAV

U S ARMY WAR COLLEGE

ATTN: LIBRARY

U S ARMY WHITE SANDS MISSILE RANGE

ATTN: K CUMMINGS

USA SURVIVABILITY MANAGEMENT OFFICE

ATTN: J BRAND

DEPARTMENT OF THE NAVY

NAVAL FACILITIES ENGINEERING COMMAND

ATTN: CODE 04B

NAVAL OCEAN SYSTEMS CENTER

ATTN: TECH LIB

NAVAL POSTGRADUATE SCHOOL

ATTN: LIBRARY

NAVAL RESEARCH LABORATORY

ATTN: TECH LIB

ATTN: D BOOK

ATTN: J BORIS

NAVAL SEA SYSTEMS COMMAND

ATTN: SEA-0351

ATTN: SEA-09G53

NAVAL SURFACE WARFARE CENTER

ATTN: TECHNICAL LIBRARY

ATTN: W GLOWASKI

NAVAL WEAPONS CENTER

ATTN: C AUSTIN

ATTN: TECH SVCS

NAVAL WEAPONS EVALUATION FACILITY

ATTN: CLASSIFIED LIBRARY

DNA-TR-85-352-V3 (DL CONTINUED)

OFC OF THE DEPUTY CHIEF OF NAVAL OPS
ATTN: OP 03EG
ATTN: OP 981

OFFICE OF NAVAL RESEARCH
ATTN: CODE 1132SM

SPACE & NAVAL WARFARE SYSTEMS CMD
ATTN: PME 117-21

DEPARTMENT OF THE AIR FORCE

AIR FORCE GEOPHYSICS LABORATORY
ATTN: H OSSING

AIR FORCE INSTITUTE OF TECHNOLOGY/EN
ATTN: C BRIDGMAN

AIR FORCE WEAPONS LABORATORY
ATTN: NTE
ATTN: NTED R HENNY
ATTN: SUL

AIR UNIVERSITY LIBRARY
ATTN: AUL-LSE

BALLISTIC MISSILE OFFICE
ATTN: ENS
ATTN: MGER
ATTN: MYEB D GAGE

HEADQUARTERS USAF/IN
ATTN: IN RM 4A932

SECRETARY OF AF/AQQS
ATTN: AF/RDQI

STRATEGIC AIR COMMAND/XRFS
ATTN: XRFS

USAF/LEEEU
ATTN: LEEE

DEPARTMENT OF ENERGY

DEPARTMENT OF ENERGY
ATTN: R JONES

DEPARTMENT OF ENERGY
ATTN: OMA/DP-225

LAWRENCE LIVERMORE NATIONAL LAB
ATTN: R SCHOCK
ATTN: P COLELLA
ATTN: P COYLE

LOS ALAMOS NATIONAL LABORATORY
ATTN: G SPILLMAN
ATTN: REPORT LIBRARY
ATTN: R WHITAKER

MARTIN MARIETTA ENERGY SYSTEMS INC
ATTN: CENTRAL RSCH LIBRARY
ATTN: CIVIL DEF RES PROJ

SANDIA NATIONAL LABORATORIES
ATTN: J S PHILLIPS
ATTN: J R BANNISTER
ATTN: L R HILL
ATTN: TECH LIB 3141

OTHER GOVERNMENT

CENTRAL INTELLIGENCE AGENCY
ATTN: OSWR/NED

DEPARTMENT OF THE INTERIOR
ATTN: TECH LIB

FEDERAL EMERGENCY MANAGEMENT AGENCY
ATTN: W CHIPMAN

DEPARTMENT OF DEFENSE CONTRACTORS

AEROSPACE CORP
ATTN: H MIRELS
ATTN: LIBRARY ACQUISITION

ANALYTIC SERVICES, INC (ANSER)
ATTN: G HESSELBACHER

APPLIED & THEORETICAL MECHANICS, INC
ATTN: J M CHAMPNEY

APPLIED RESEARCH ASSOCIATES, INC
ATTN: N HIGGINS

APPLIED RESEARCH ASSOCIATES, INC
ATTN: R FRANK

BDM CORP
ATTN: F LEECH
ATTN: R HENSLEY

BDM CORPORATION
ATTN: J MERRITT
ATTN: LIBRARY

BDM INTERNATIONAL INC
ATTN: A LAVAGNINO
ATTN: A VITELLO
ATTN: E DORCHAK
ATTN: J STOCKTON

BGEING CO
ATTN: H WICKLEIN

CALIFORNIA RESEARCH & TECHNOLOGY, INC
ATTN: K KREYENHAGEN
ATTN: LIBRARY
ATTN: M ROSENBLATT

CALIFORNIA RESEARCH & TECHNOLOGY, INC
ATTN: J THOMPSON

CALSPAN CORP
ATTN: LIBRARY

CARPENTER RESEARCH CORP
ATTN: H J CARPENTER

DENVER COLORADO SEMINARY UNIVERSITY OF ATTN: J WISOTSKI	R & D ASSOCIATES ATTN: E FURBEE
ERNST-MACH INSTITUT 2 CYS ATTN: M REICHENBACH	R & D ASSOCIATES ATTN: G GANONG
IIT RESEARCH INSTITUTE ATTN: DOCUMENTS LIBRARY ATTN: M JOHNSON	RAND CORP ATTN: B BENNETT
INFORMATION SCIENCE, INC ATTN: W DUDZIAK	S-CUBED ATTN: D GRINE
INSTITUTE FOR DEFENSE ANALYSES ATTN: CLASSIFIED LIBRARY	SCIENCE APPLICATIONS INTL CORP ATTN: TECHNICAL LIBRARY
KAMAN SCIENCES CORP ATTN: L MENTE ATTN: LIBRARY ATTN: R RUETENIK ATTN: W LEE	SCIENCE APPLICATIONS INTL CORP ATTN: J COCKAYNE ATTN: R SIEVERS ATTN: W LAYSON
KAMAN SCIENCES CORP ATTN: F SHELTON ATTN: B KINSLOW	SCIENCE APPLICATIONS INTL CORP ATTN: G BINNINGER
KAMAN SCIENCES CORP ATTN: E CONRAD	SOUTHWEST RESEARCH INSTITUTE ATTN: A WENZEL
KAMAN SCIENCES CORPORATION ATTN: DASIAK	SRI INTERNATIONAL ATTN: J COLTON
KAMAN SCIENCES CORPORATION ATTN: DASIAK	TECH REPS, INC ATTN: F MCMILLIN
LOCKHEED MISSILES & SPACE CO, INC ATTN: TECH INFO CTR	TECH REPS, INC ATTN: J KEEFER
MARTIN MARIETTA CORP ATTN: G FOTIEO	TELEDYNE BROWN ENGINEERING ATTN: J RAVENSCRAFT
MCDONNELL DOUGLAS CORP ATTN: M POTTER	TERRA TEK, INC ATTN: A JONES ATTN: S GREEN
MCDONNELL DOUGLAS CORPORATION ATTN: R HALPRIN	TRW INC ATTN: TECH INFO CTR
NICHOLS RESEARCH CORP, INC ATTN: R BYRN	TRW SPACE & DEFENSE SYSTEMS ATTN: W WAMPLER
PACIFIC-SIERRA RESEARCH CORP ATTN: H BRODE	WEIDLINGER ASSOC., CONSULTING ENGRG ATTN: T DEEVY
PACIFICA TECHNOLOGY ATTN: R ALLEN ATTN: R BJORK	WEIDLINGER ASSOC, INC ATTN: J ISENBERG
PATEL ENTERPRISES, INC ATTN: M PATEL	WEIDLINGER ASSOCIATES, INC ATTN: I SANDLER ATTN: M BARON
R & D ASSOCIATES ATTN: A KUHL ATTN: D SIMONS ATTN: J LEWIS ATTN: T MAZZOLA ATTN: TECHNICAL INFORMATION CENTER	